Scale Interactions: Time and Space, Ocean and Atmosphere

- ITCZ Is a global tropical feature that also links Walker and Hadley Cells.

- ITCZ is easy to see but not easy to define except in the zonal mean

- ENSO and Warming affect the Hadley cell and the ITCZ. What are the relations? Zonal asymmetries?

What has been driving the downward trend in the ISMR?

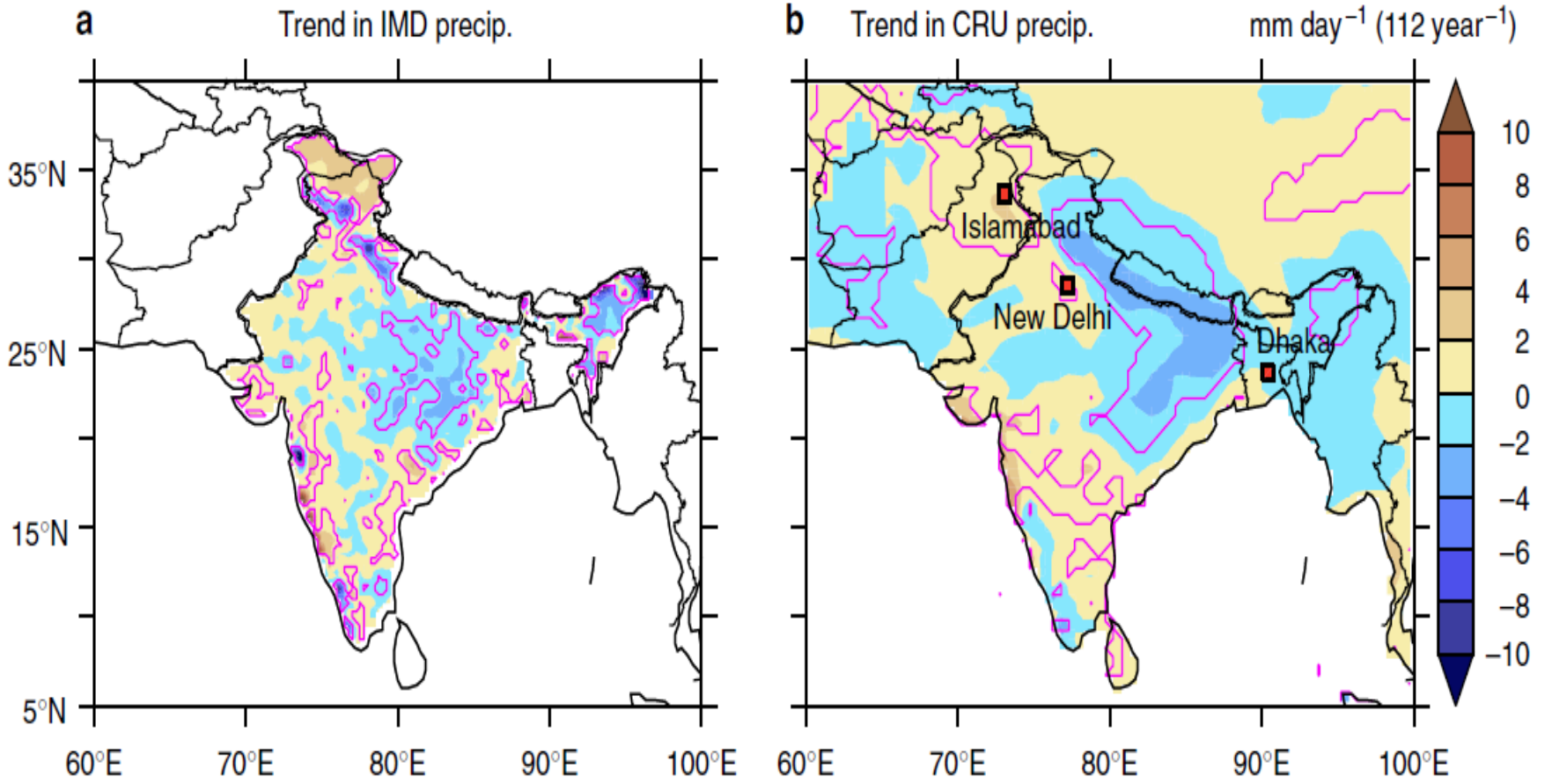

Figure 1 | Summer monsoon precipitation trends for the years 1901-2012. Observed trend in precipitation (mm day^{-1} 112 year^{-1}) in (**a**) IMD and (**b**) CRU datasets, during June-September, for the years 1901-2012. Contours denote regions significant at the 95% confidence level.

Roxy et al. 2015, Nature Communications

Indian Ocean Warming?

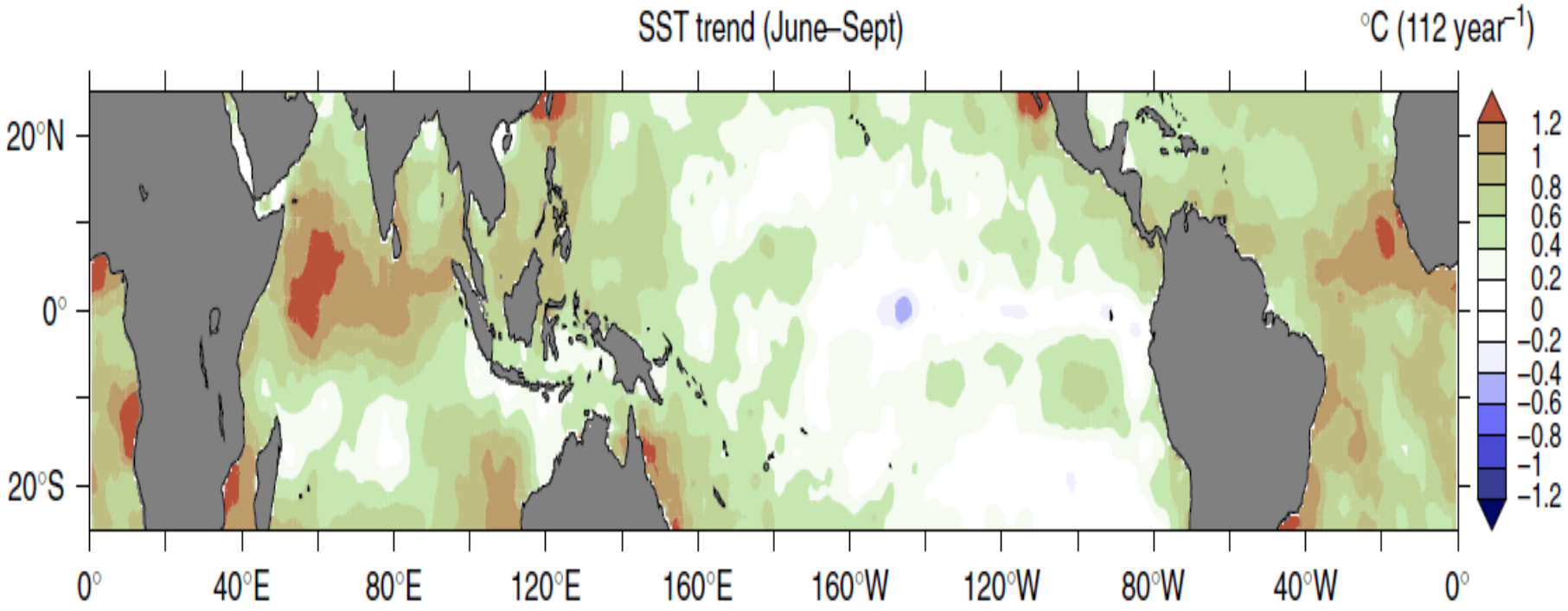

Figure 2 | Summer sea surface temperature trends for the years 1901–2012. Observed trend in mean summer (June–September) SST (°C 112 year^{-1}) over the global tropics during 1901–2012.

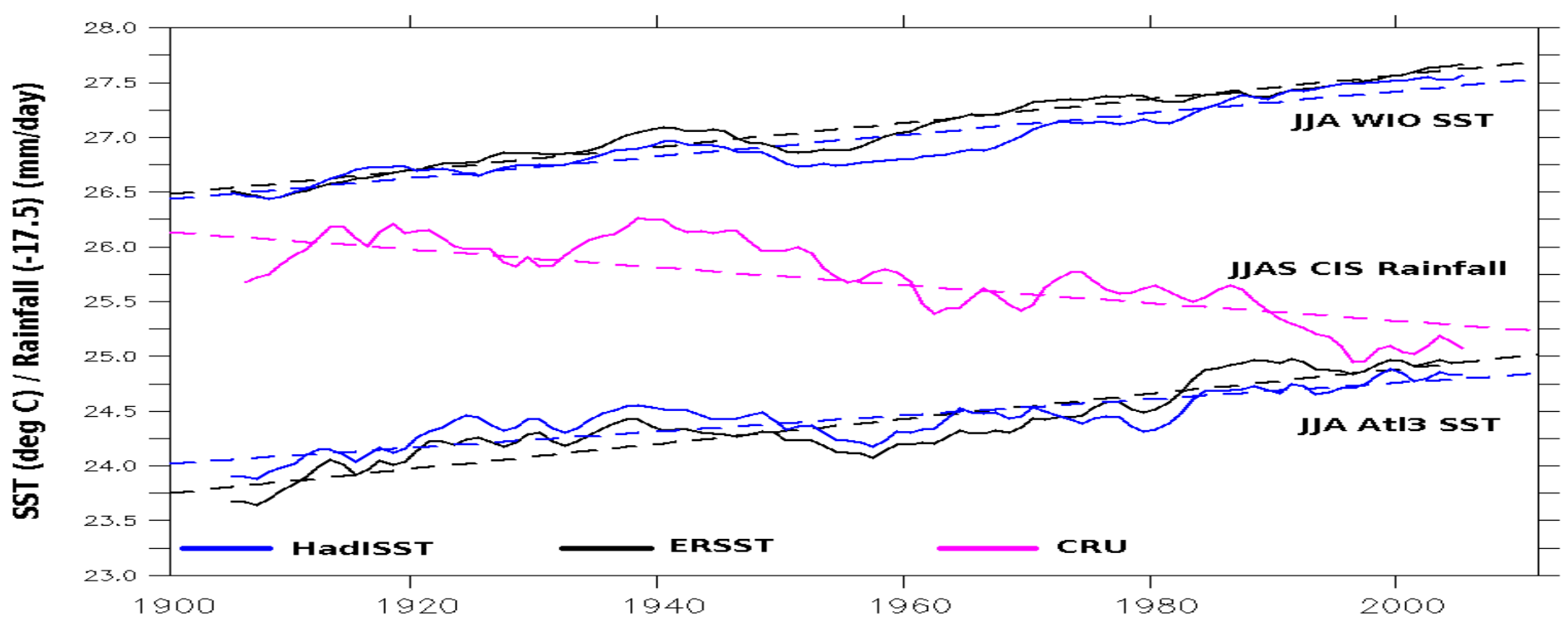

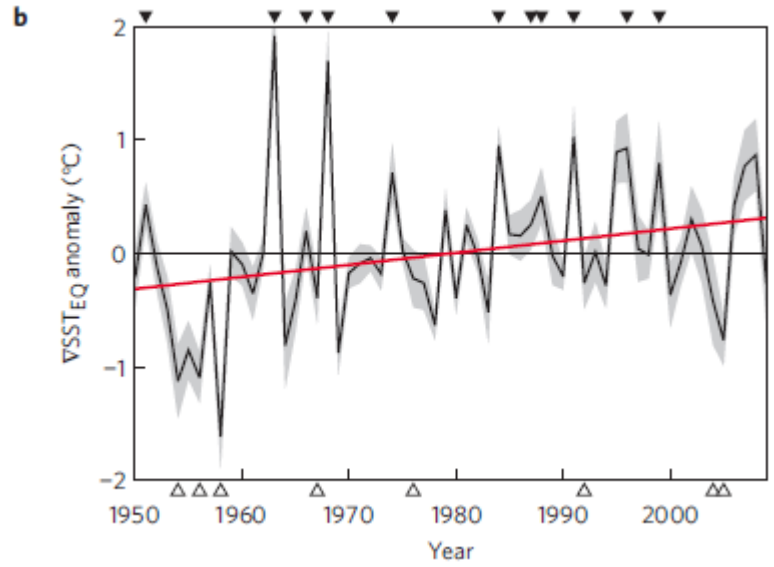

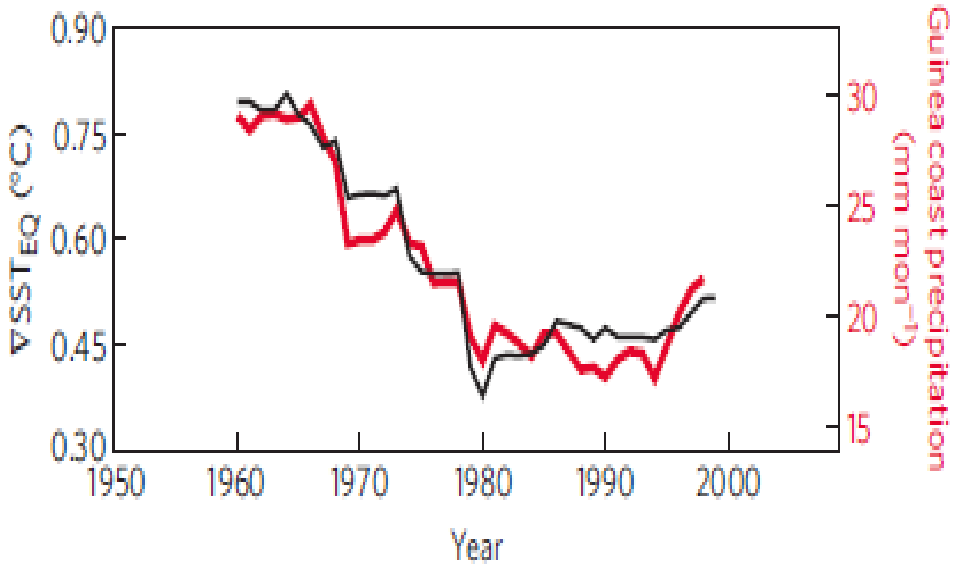

Tokinaga and Xie 2011

Equatorial SST gradient and Running mean variance

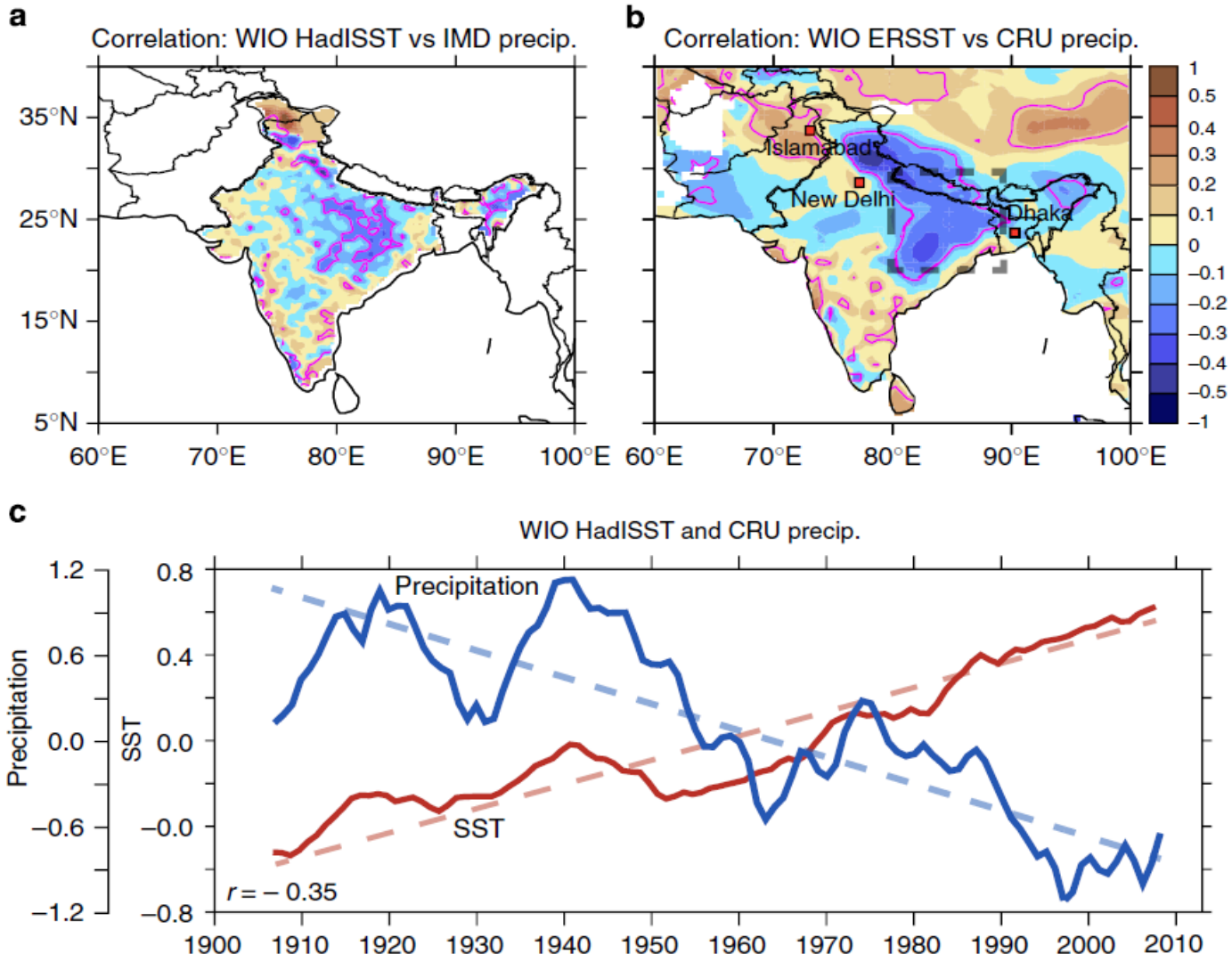

Causal?

Figure 3 | Correlation between western Indian Ocean sea surface temperatures and monsoon precipitation. Correlation between SST over the western Indian Ocean (WIO, 50-65°E, 5°S-10°N) and precipitation over the South Asian subcontinent, for (**a**) HadISST and IMD precipitation, and (**b**) ERSST and CRU precipitation, for June–September 1901–2012. Contours denote regions significant at the 95% confidence level. The inset box includes parts of the central Indian subcontinent where the weakening trend in precipitation is significant (**c**) Time series of SST anomalies (°C, *red*) over western Indian Ocean along with CRU (*blue*) precipitation (mm day^{-1}) over central Indian subcontinent (80–90°E, 20–30°N, inset box in ***b***), smoothed with a 10 year moving average. Note that the correlation coefficient ($r = -0.34$) between HadISST and CRU precipitation is estimated using non-smoothed time series. Kendall's rank correlation test for the two variables provided a tau coefficient of -0.3 ($P<0.01$, two tailed). Mann–Kendall test for the trend in the time series provided a tau coefficient of 0.6 for SST and -0.2 for precipitation, both significant at 95% confidence level.

ITCZ – The Global Tropical Conveyor

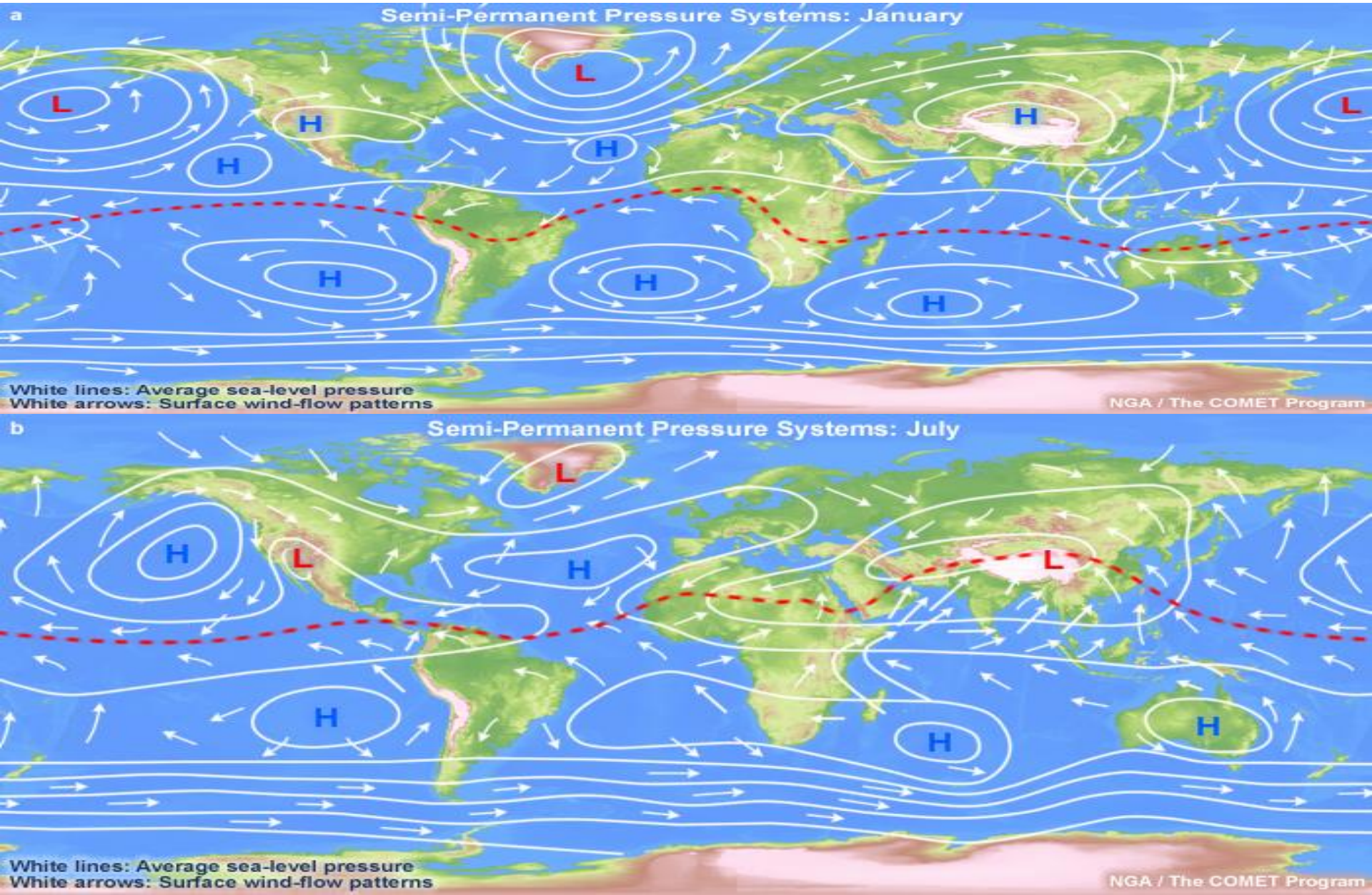

We should obviously be able to relate the ITCZ to rainy seasons on land

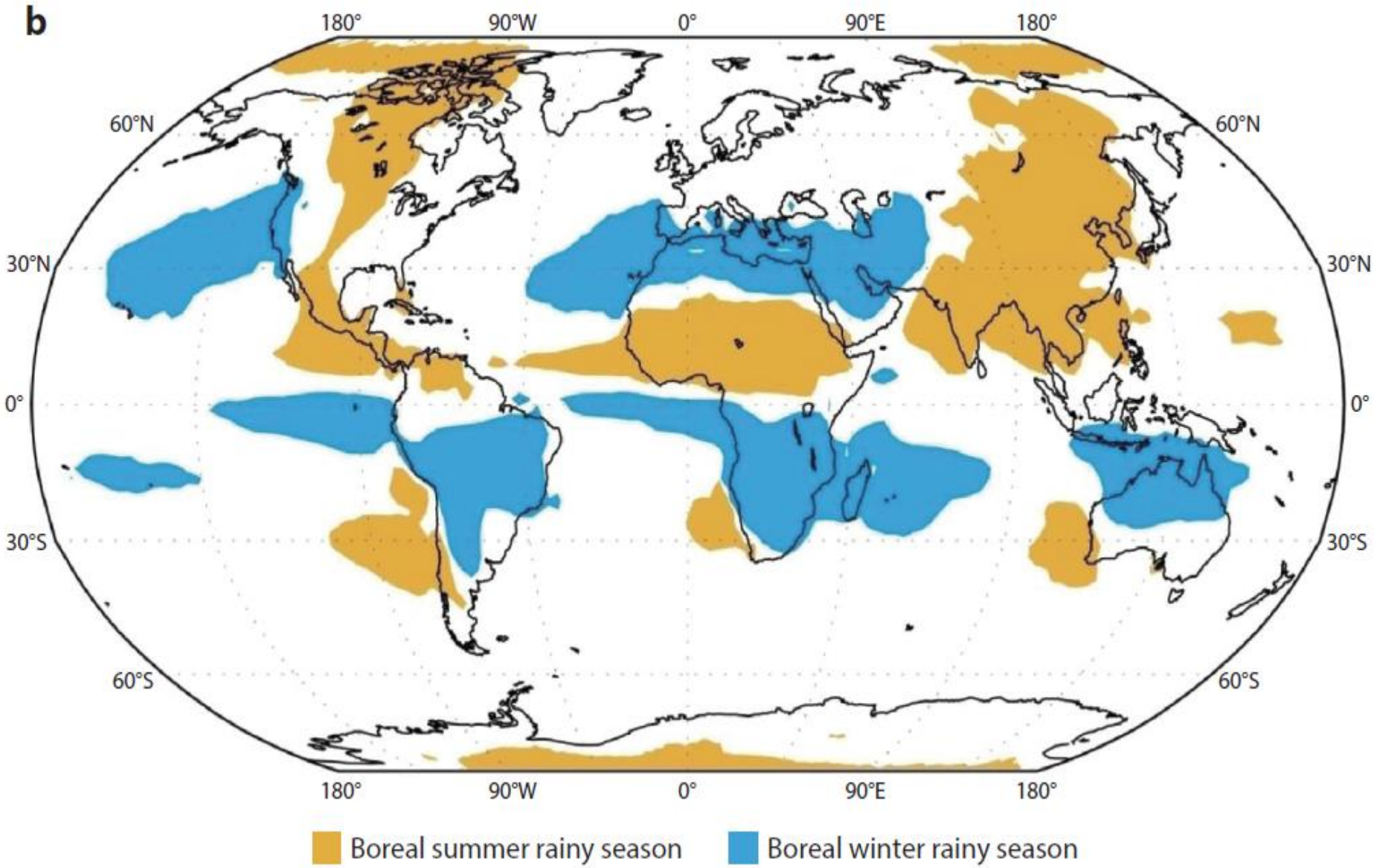

But also more specifically to the Global Monsoon

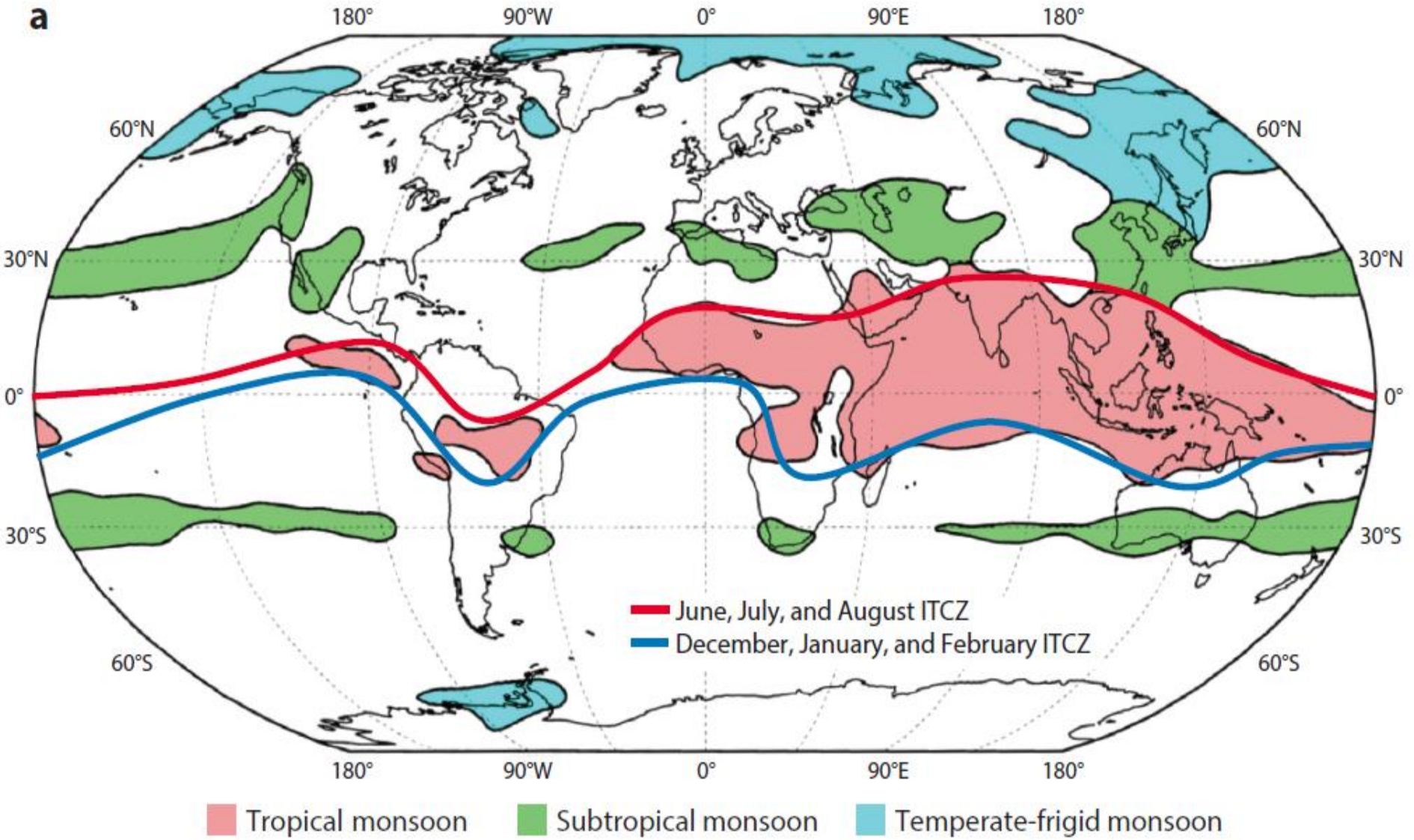

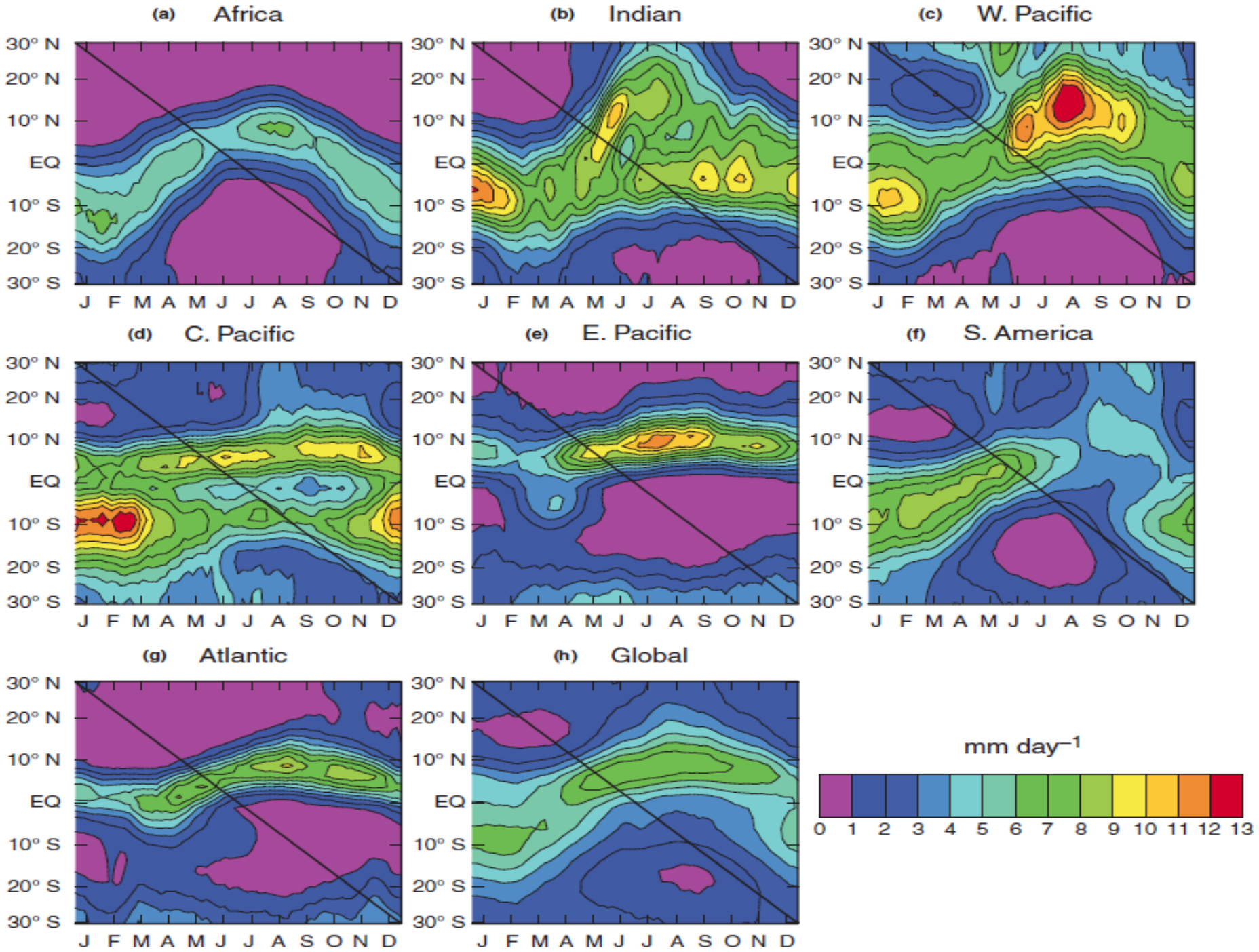
(a) Africa
(b) Indian
(c) W. Pacific
(d) C. Pacific
(e) E. Pacific
(f) S. America
(g) Atlantic
(h) Global
30° N
20° N
10° N
EQ
10° S
20° S
30° S
J F M A M J J A S O N D
mm day−1
0 1 2 3 4 5 6 7 8 9 10 11 12 13

The ITCZ moves north over the maritime continent to create seasonality

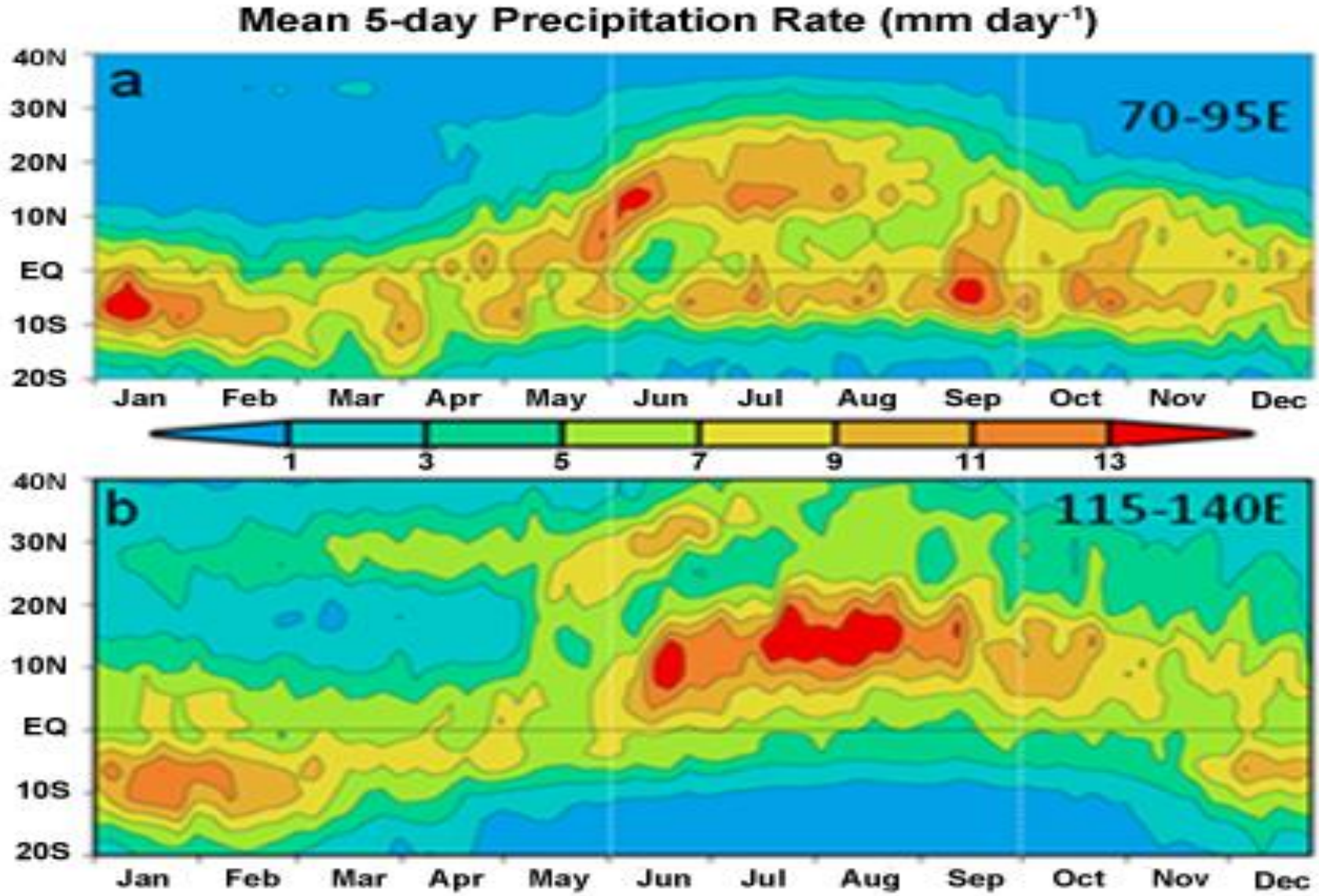

WMO

What are the interactions between the components of the Global Monsoon?Is the ISM boxed in by Orography?

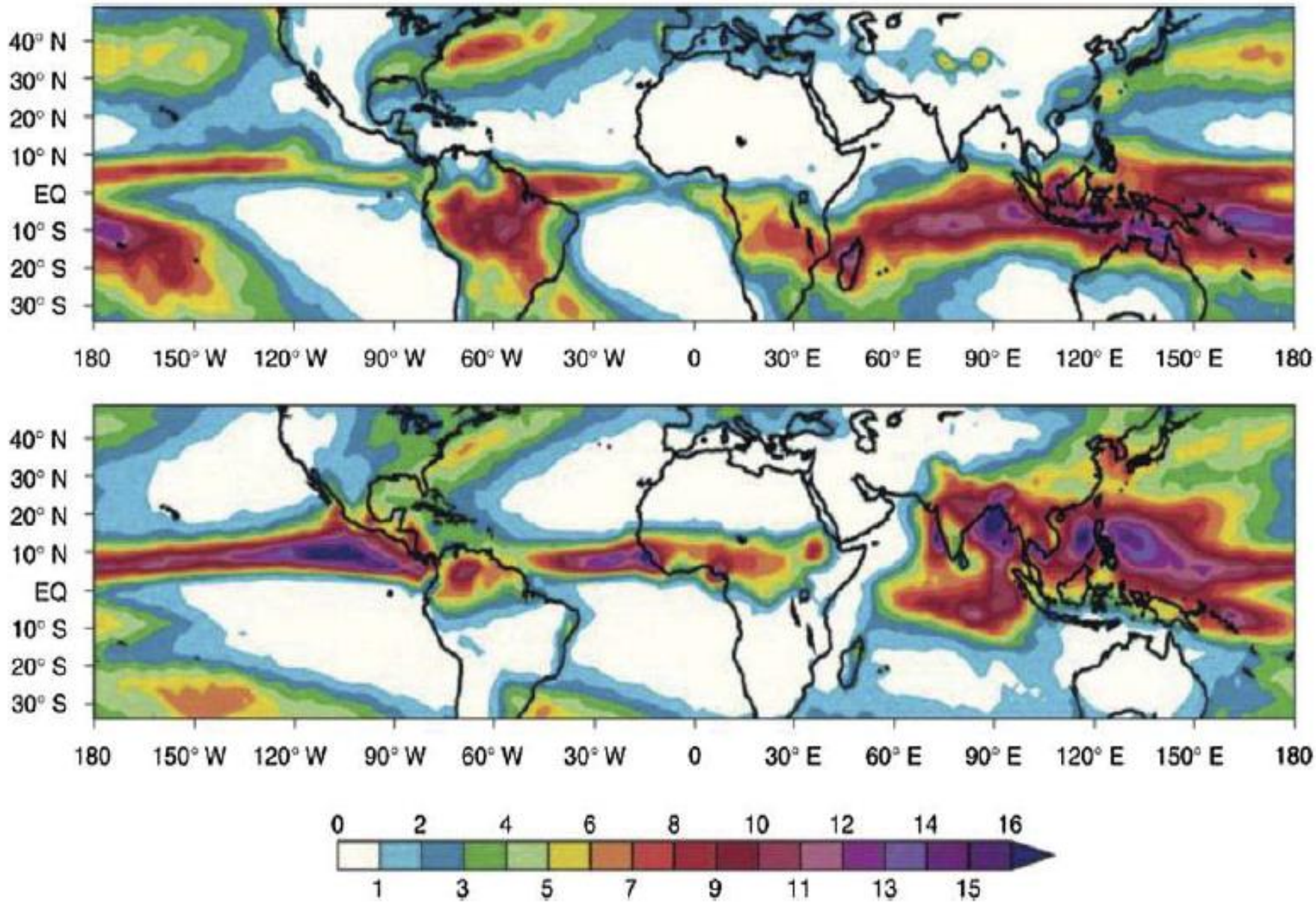

Timescales: We will not tlak much about diurnal cycle

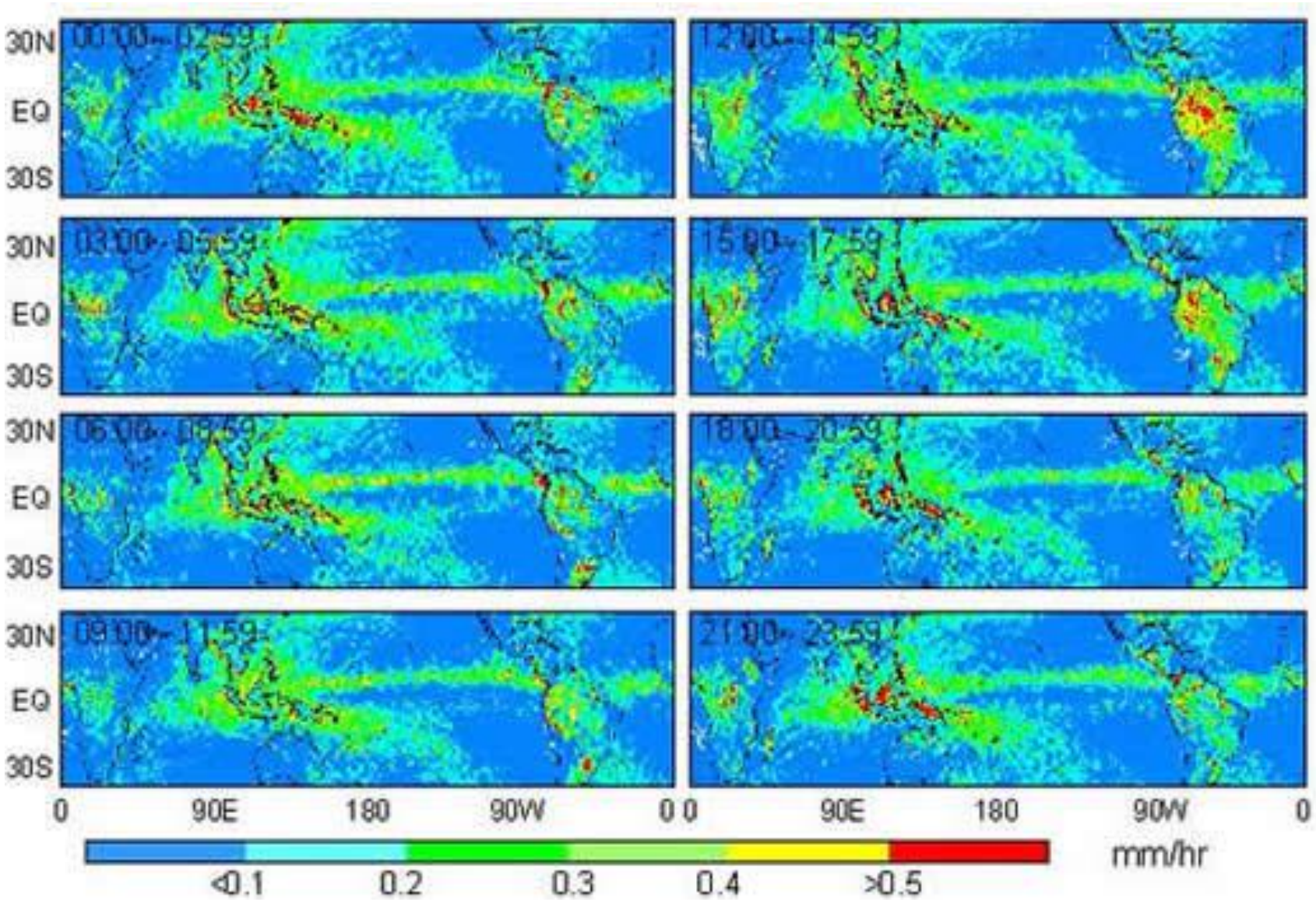

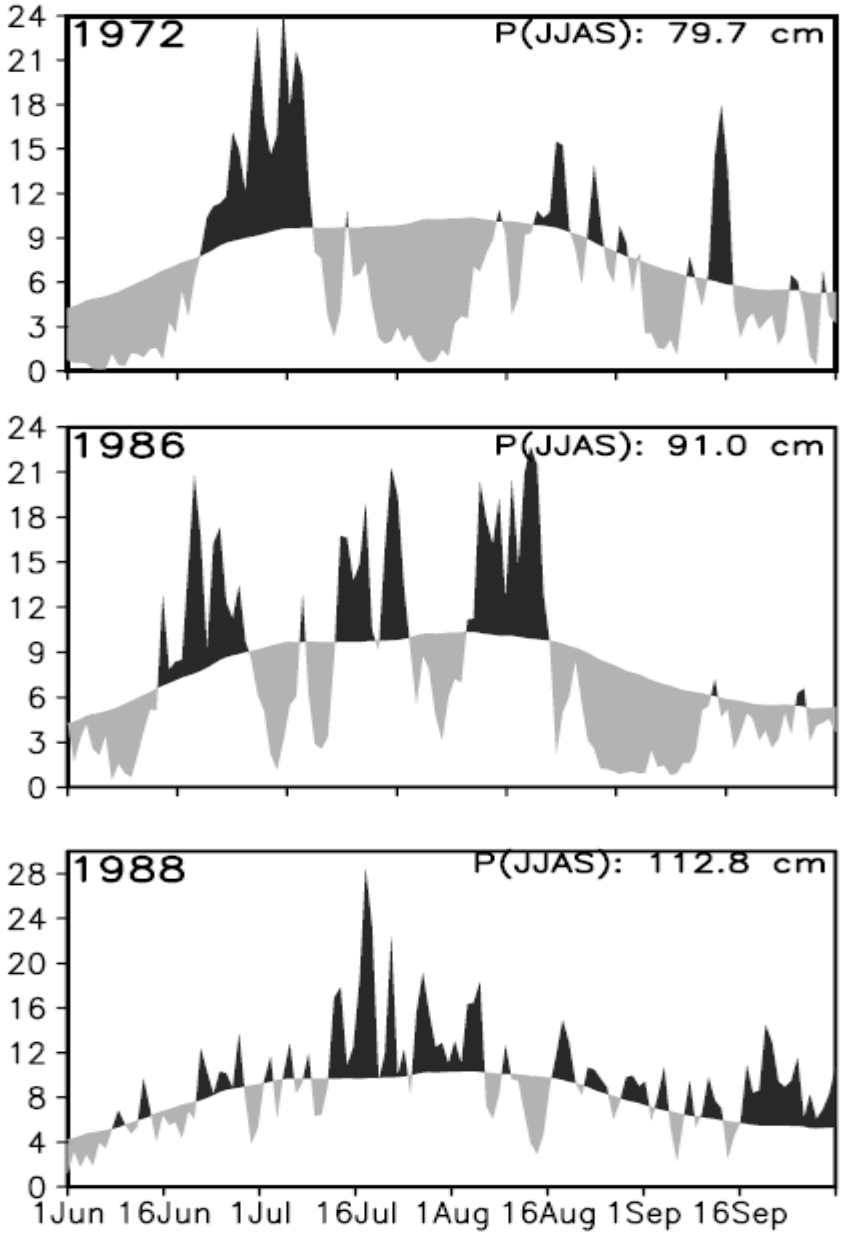

Figure 2.2. Daily rainfall (mm day^{-1}) averaged over 72°E–87°E and 10°N–25°N based on station data over the Indian continent during the summer monsoon season for three years, 1972, 1986, and 1988. Departure from the mean annual cycle (shown as the envelope) are shaded. Seasonal mean rainfall for each year are also shown in the top-right corners.

ISVs and ISV Variability –

Does the ITCZ link ISVs across basins?

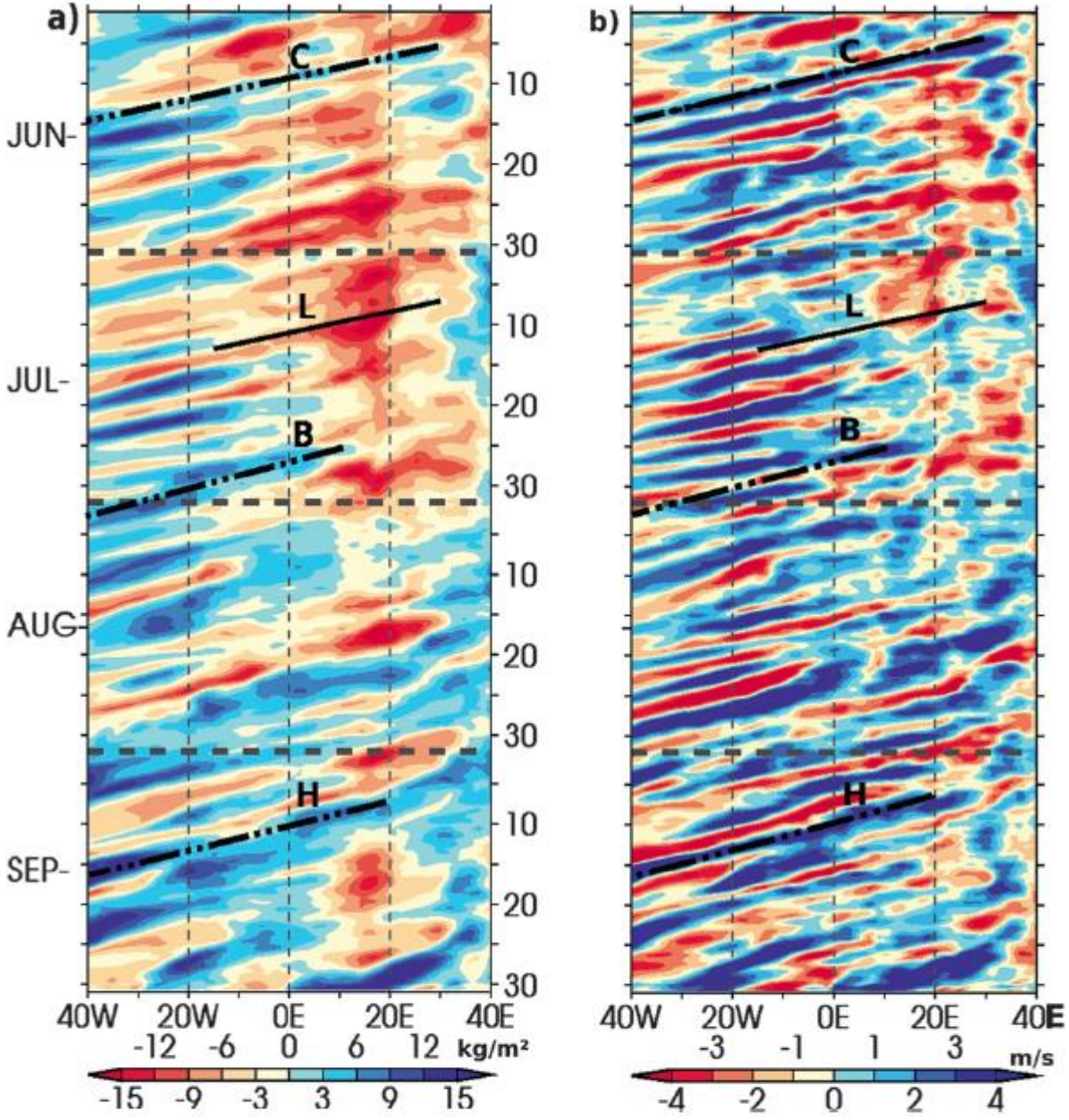

FIG. 3. Time–longitude diagram of the 2006 JJAS intraseasonal anomalies averaged over 12°–20°N: (a) PW (kg m^{-2}) and (b) 850-hPa meridional wind (m s^{-1}). The black solid lines materialize a slope of a 9 m s^{-1} velocity. C, L, B, and H refer to events referenced in section 3.

Are the ISVs linked some how?

AEWs, MJOs, MISOs

West African Monsoon Intraseasonal Variability: A Precipitable Water Perspective

D. EMMANUEL POAN, ROMAIN ROEHRIG, FLEUR COUVREUX, AND JEAN-PHILIPPE LAFORE

CNRM-GAME, Météo France, and CNRS, Toulouse, France

ISVs in warm SSTs are small because convection smooths them out.

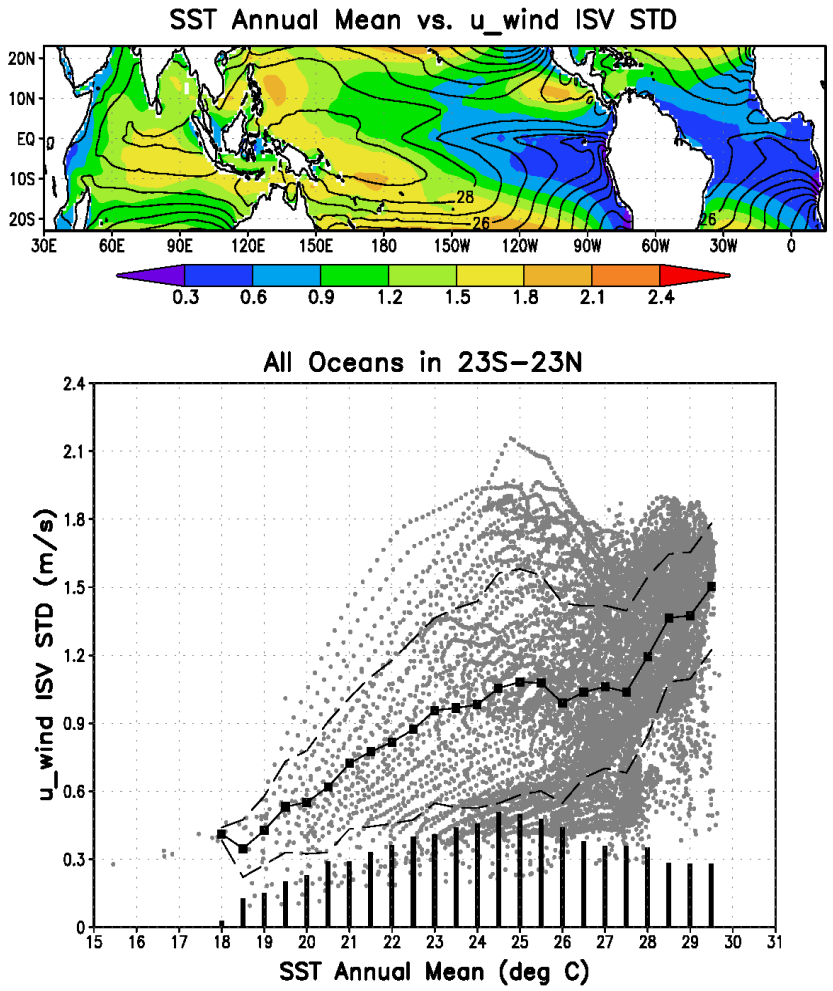

Fig. 1 Standard deviation (std) of band-pass filtered (30-120 days) zonal wind (m/s) and annual mean SST (°C) in the latitude range 23°S–23°N. (Upper panel) u wind std is color shaded, and mean SST is contoured. Contour level is 1°C. (Lower panel) Scatter plot between SST annual mean and u wind filtered std. Black squares indicate average of wind std on each SST bin the size of which is 0.5°C. Black dash lines indicate the average plus/minus one std, and black bar is std of u wind std.

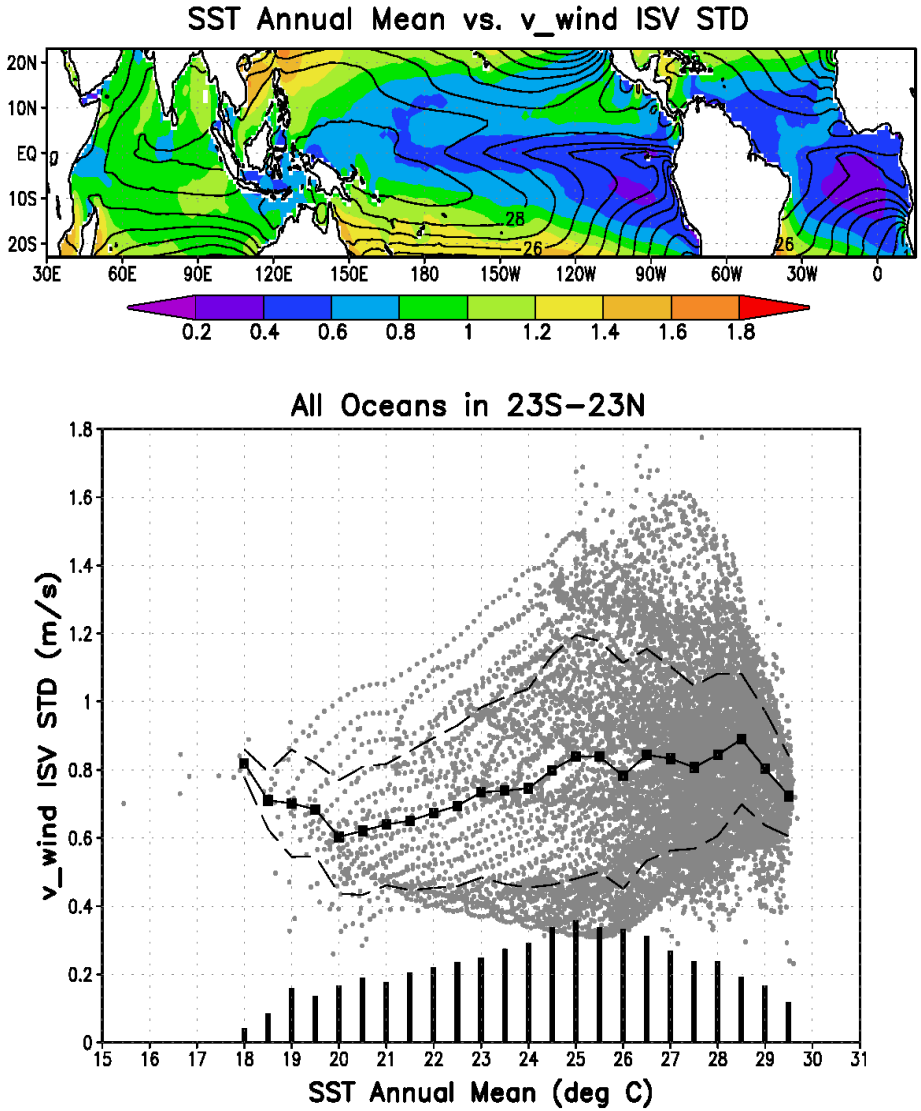

Fig. 2 Same as Fig. 1 except meridional wind (v) instead of zonal wind.

SSTs are an integrated response to momentum, heat, and freshwater fluxes – but feedbacks can be critical

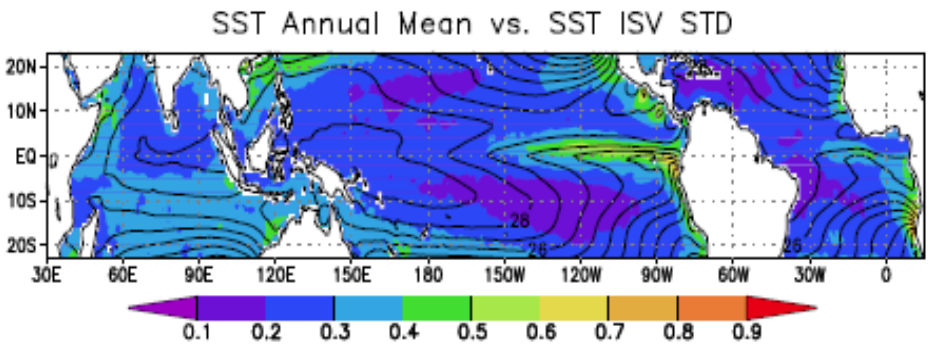

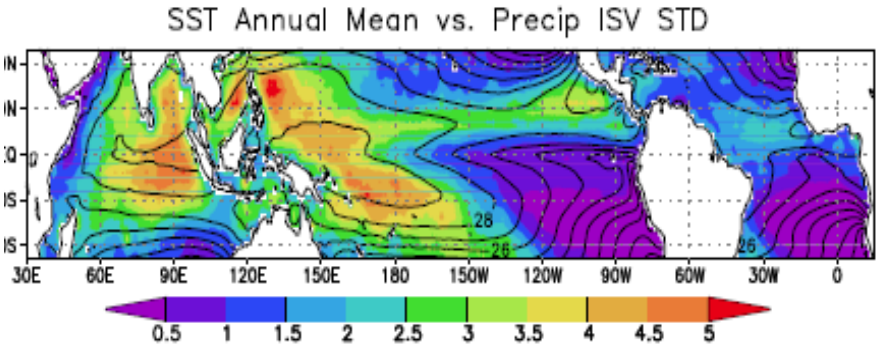

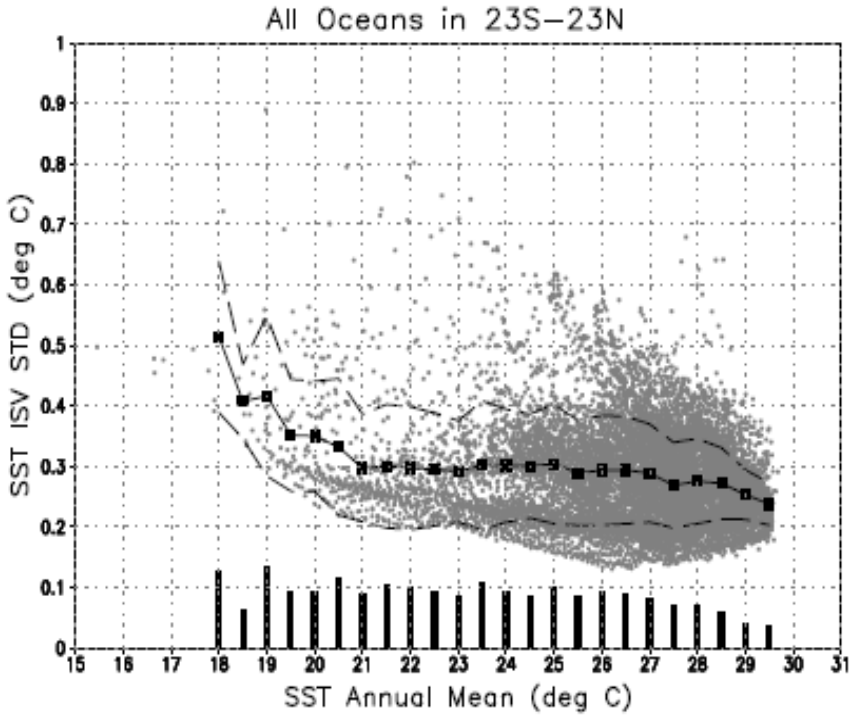

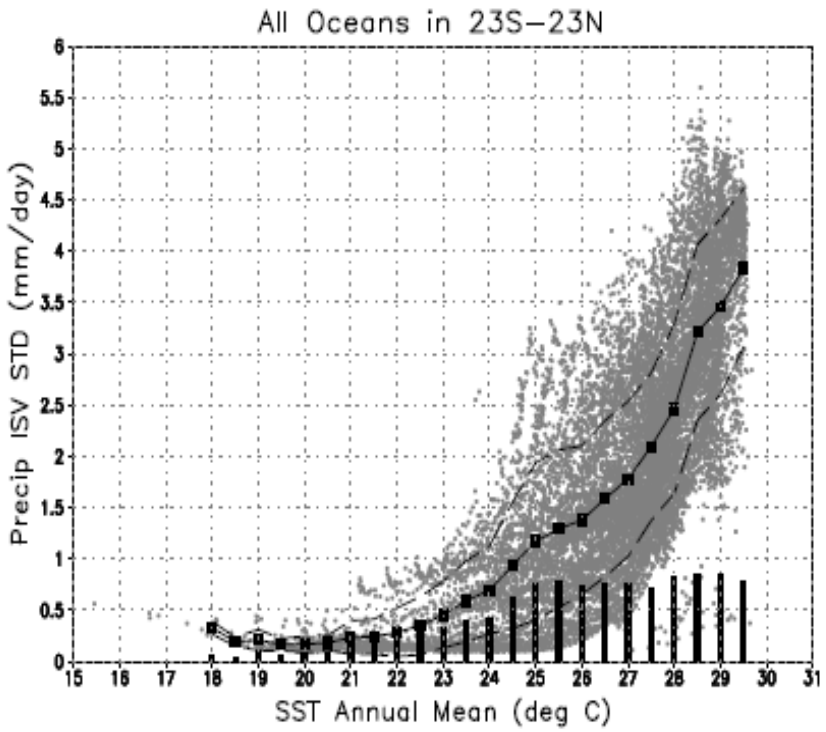

Fig. 11 Same as Fig. 1 except for sea surface temperature (SST).

g. 9 Same as Fig. 1 except for precipitation (mm/day).

Model biases persist in the Tropical Atlantic. But are they local? Amplified locally? Or is it the ITCZ?

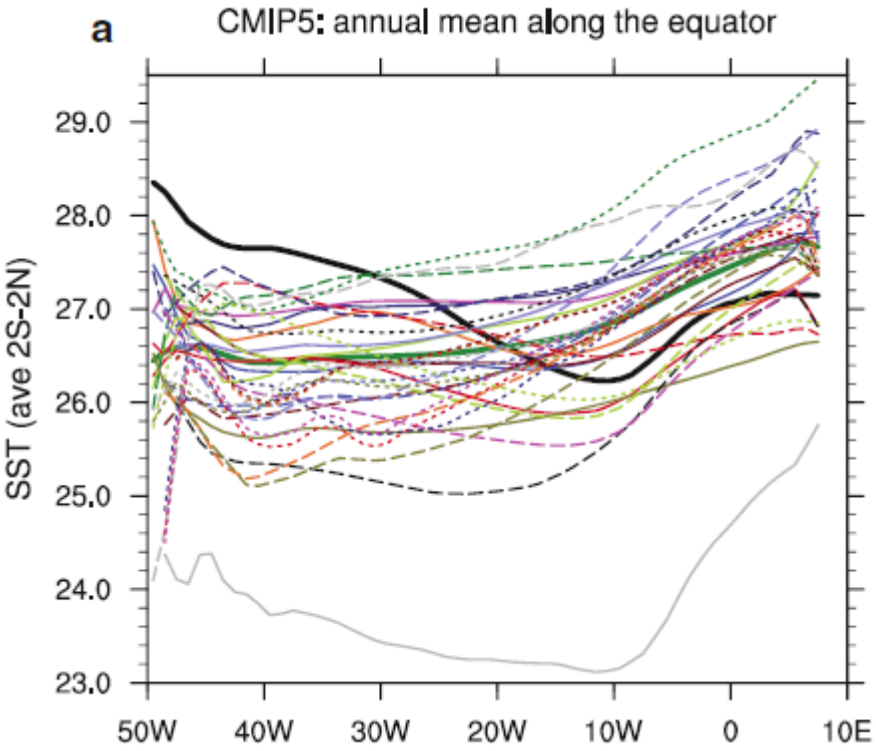

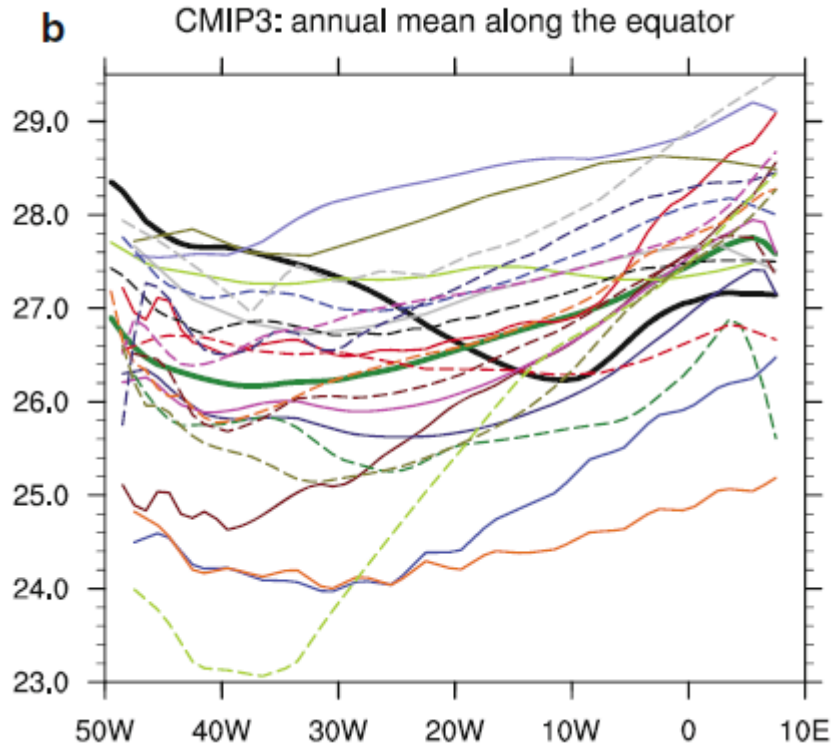

It is not a good idea to diagnose biases basin-by-basin

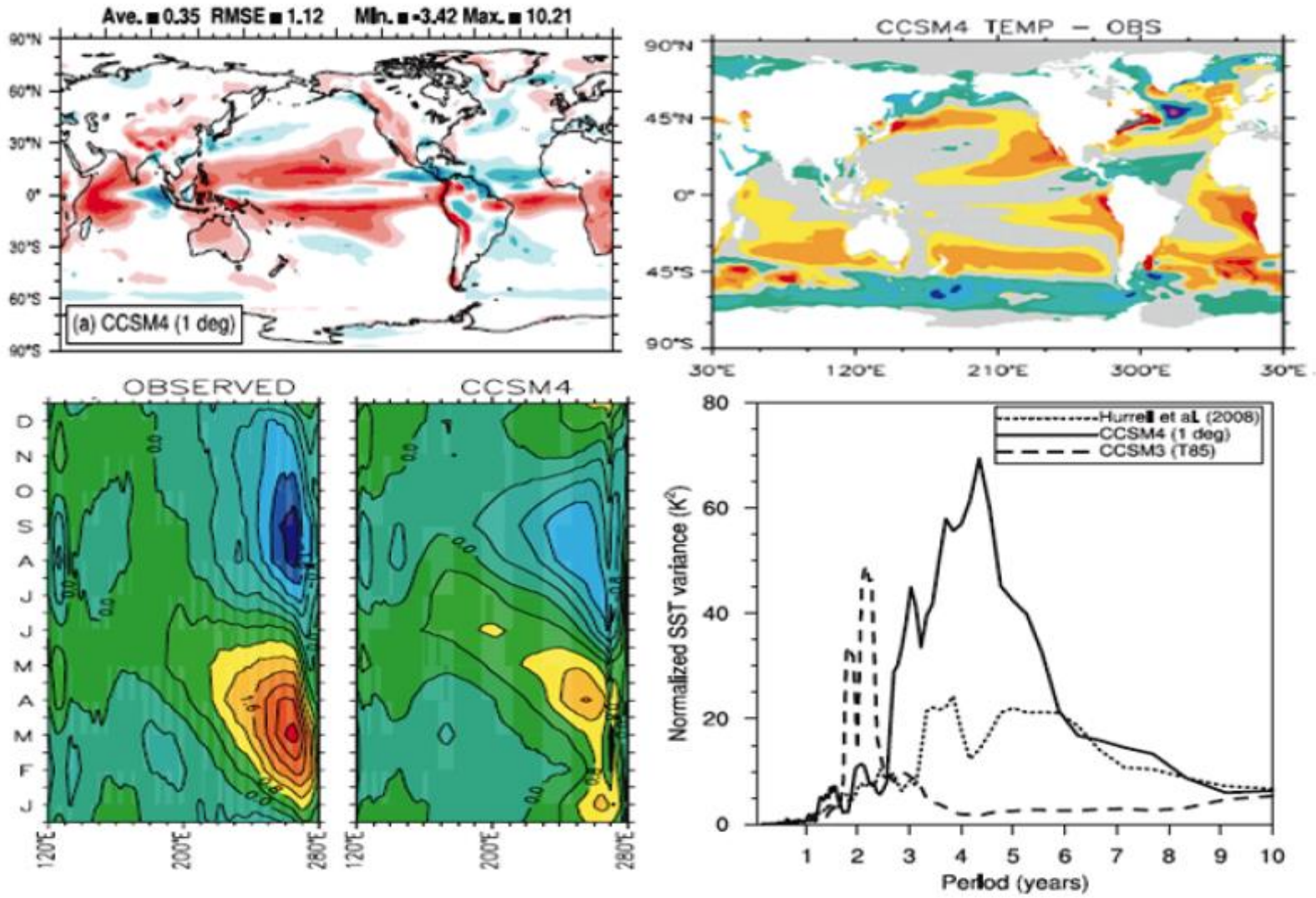

Figure 2. Top: Differences in CCSM4 and observed precipitation (left) and SSTs (right). Bottom: Annual cycle of CCSM4 and observed SSTs in the equatorial Pacific (left) and normalized NINO3.4 SST variance for observations, CCSM3 and CCSM4. The double ITCZ persists despite a warm bias in the cold tongue. The annual cycle of SST is weaker but ENSO variance is much stronger than observations even though they are improved compared to CCSM3. (From Gent et al. 2011 and Danabasoglu et al. 2012).

Fig. 12 Latitude-time sections of climatological precipitation (*shading*; mm days^{-1}) and surface wind stress (vectors; reference 5 Nm^{-2} × 10^{-2}) averaged between (40–30°W). The panels show **a** GPCP precipitation and WASWind surface wind stress, **b** ERA interim reanalysis, **c** ensemble MOST, **d** ensemble AN. The *orange contour lines* in panels **b**, **c**, and **d** show the precipitation difference with the GPCP climatology

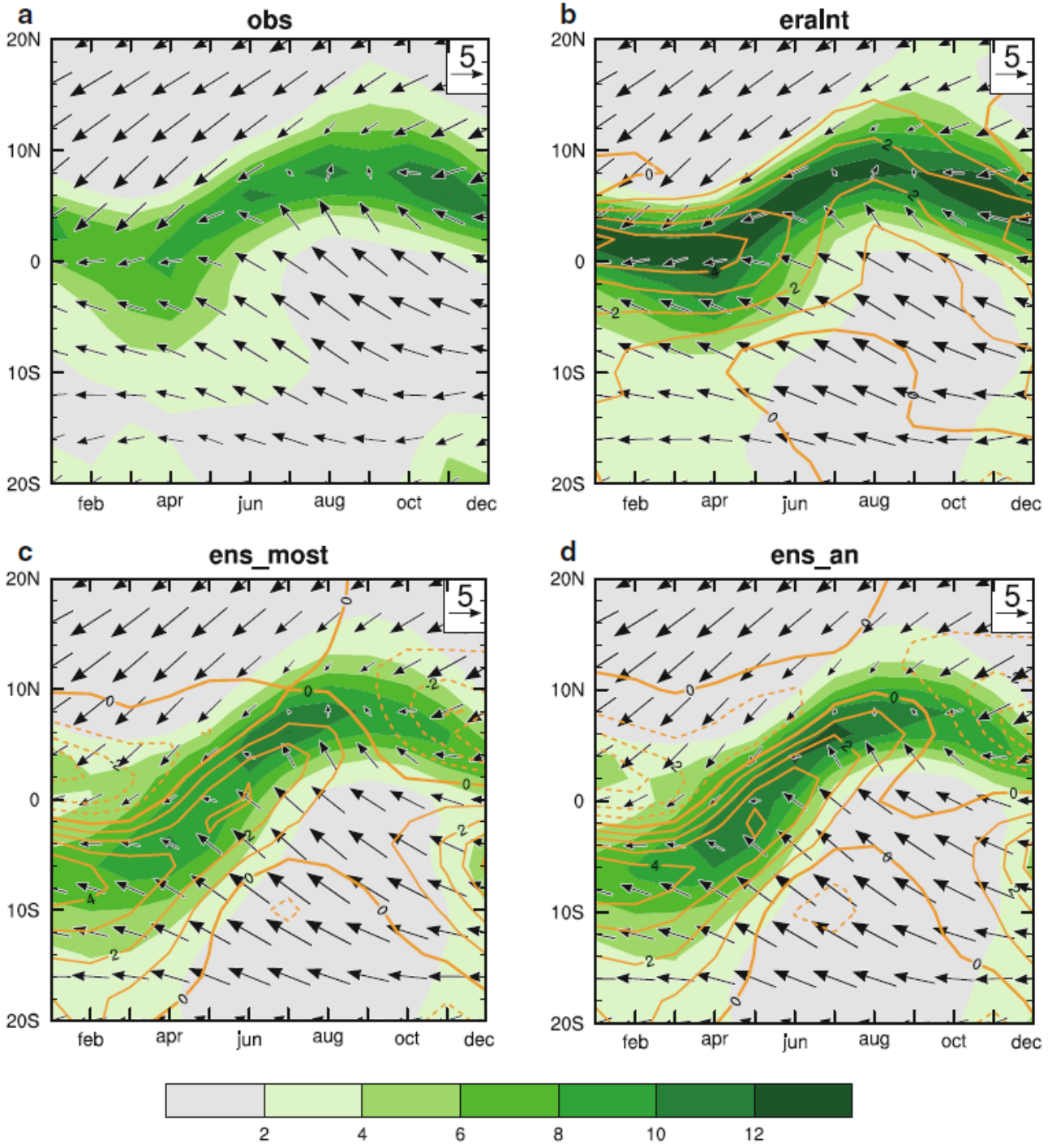

Richter et al. 2011

ITCZ touching the equator can trigger zonal and meridional modes.

AN: Atl Niño realistic

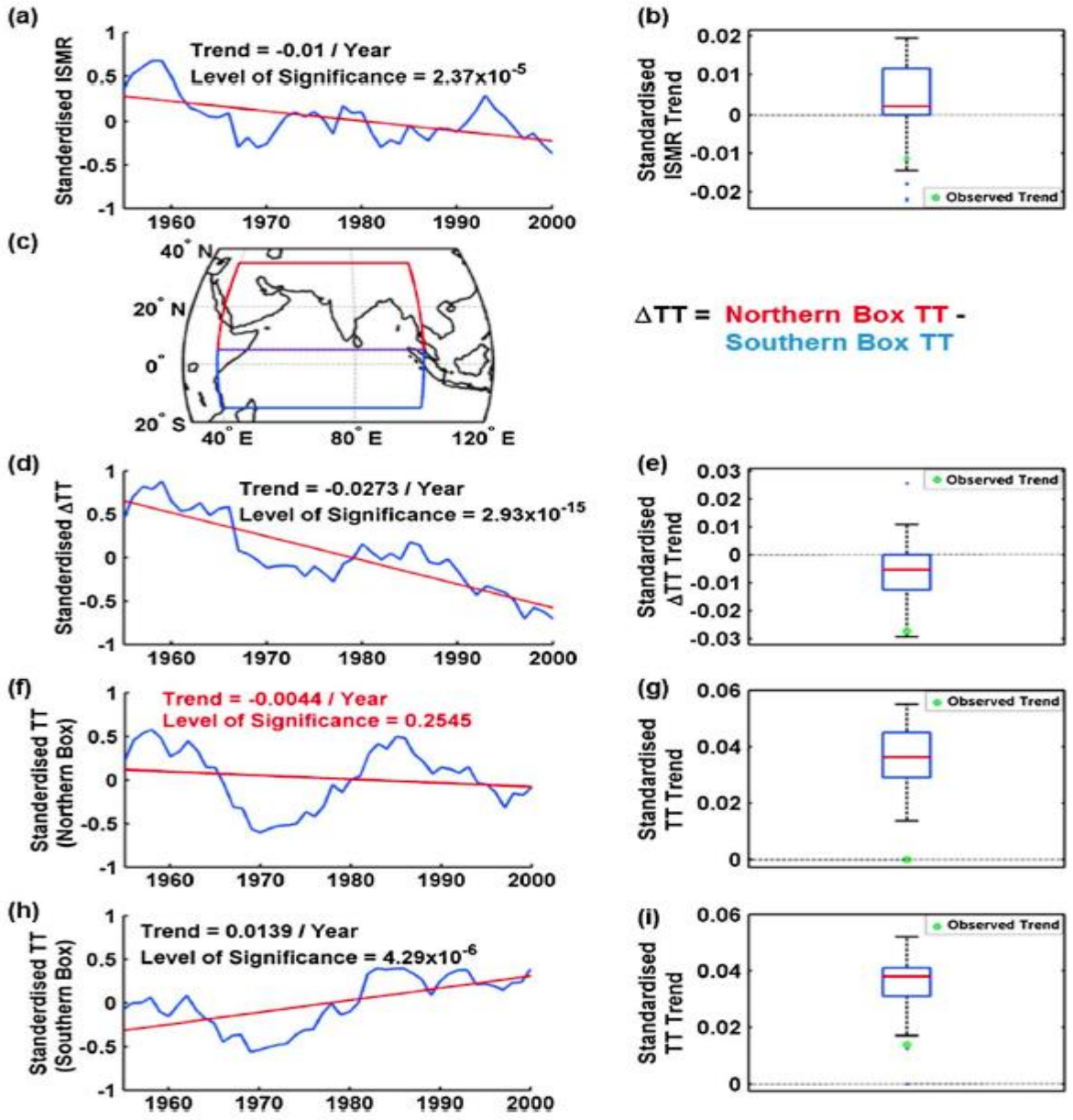

Not surprisingly, East African monsoon is also unreliable in CMIP5 models

Figure 1. Failure of CMIP5 models in simulation of ISMR trends. (a, c, d, f, h) The observed trend and (b, e, g, i) the GCM simulated trends of ISMR (Figures 1a and 1b), ΔTT (Figures 1d and 1e), Northern box TT (Figures 1f and 1g), and Southern box TT (Figures 1h and 1i). The blue line represents the observed time series and the red line represents linear trend (Figures 1a, 1c, 1d, 1f, and 1h). Lower and upper bound of the box represents 25 and 75 percentiles, respectively, and the red line indicates 50 percentile (Figures 1b, 1e, 1g, and 1i). The green dot represents observed trend. Figure 1c shows the northern and southern boxes used for ΔTT computation.

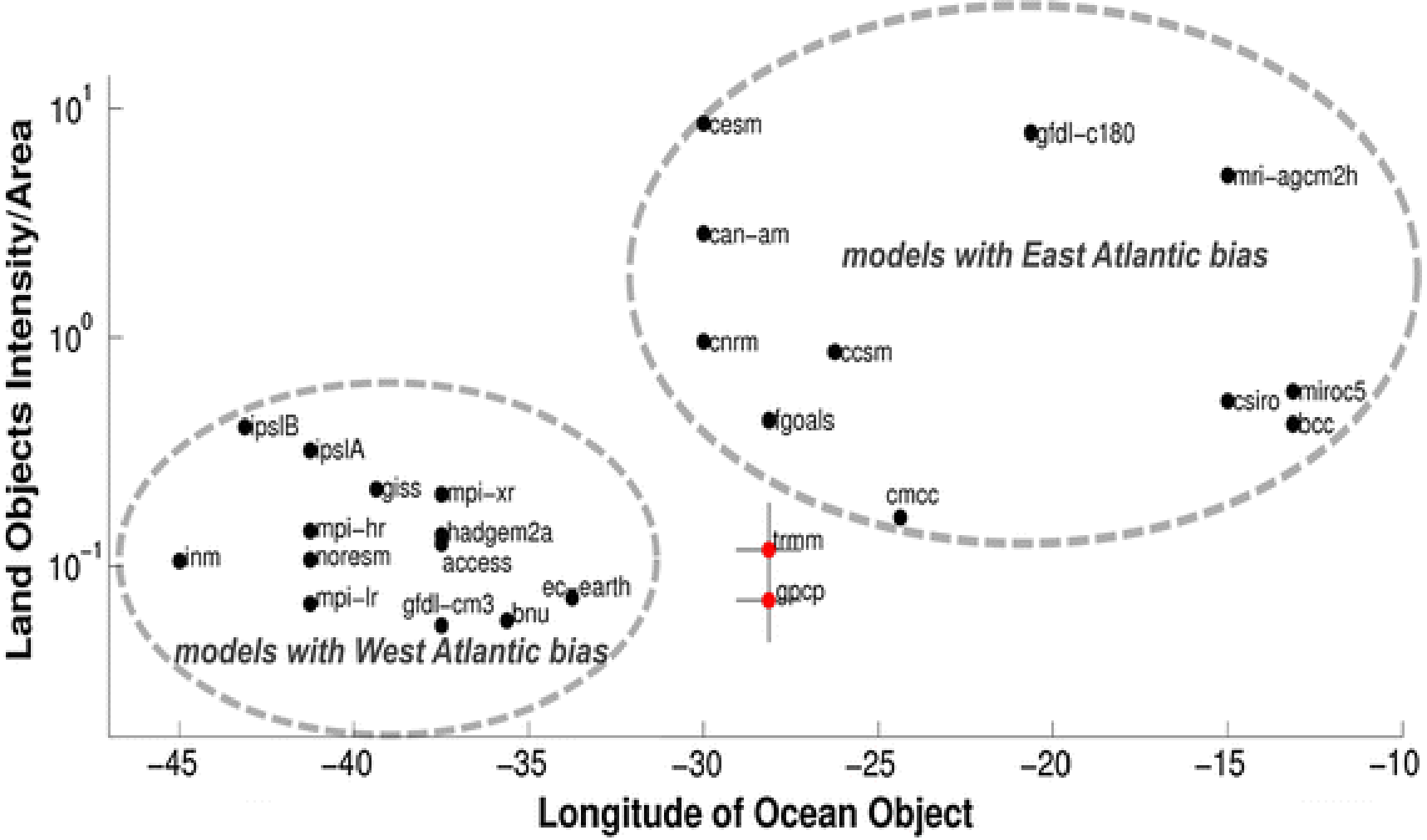

Longitude of the ocean object plotted against the intensity-area ratio (measure of peakedness) averaged over the three most rainy objects over land. The *gray lines* in GPCP and TRMM show the interquartile range of the interannual variability of their object properties

West and East Atlantic Biases – Land and Ocean convection?

Siongco et al. 2015

Obviously this shows up as model bias at global scale

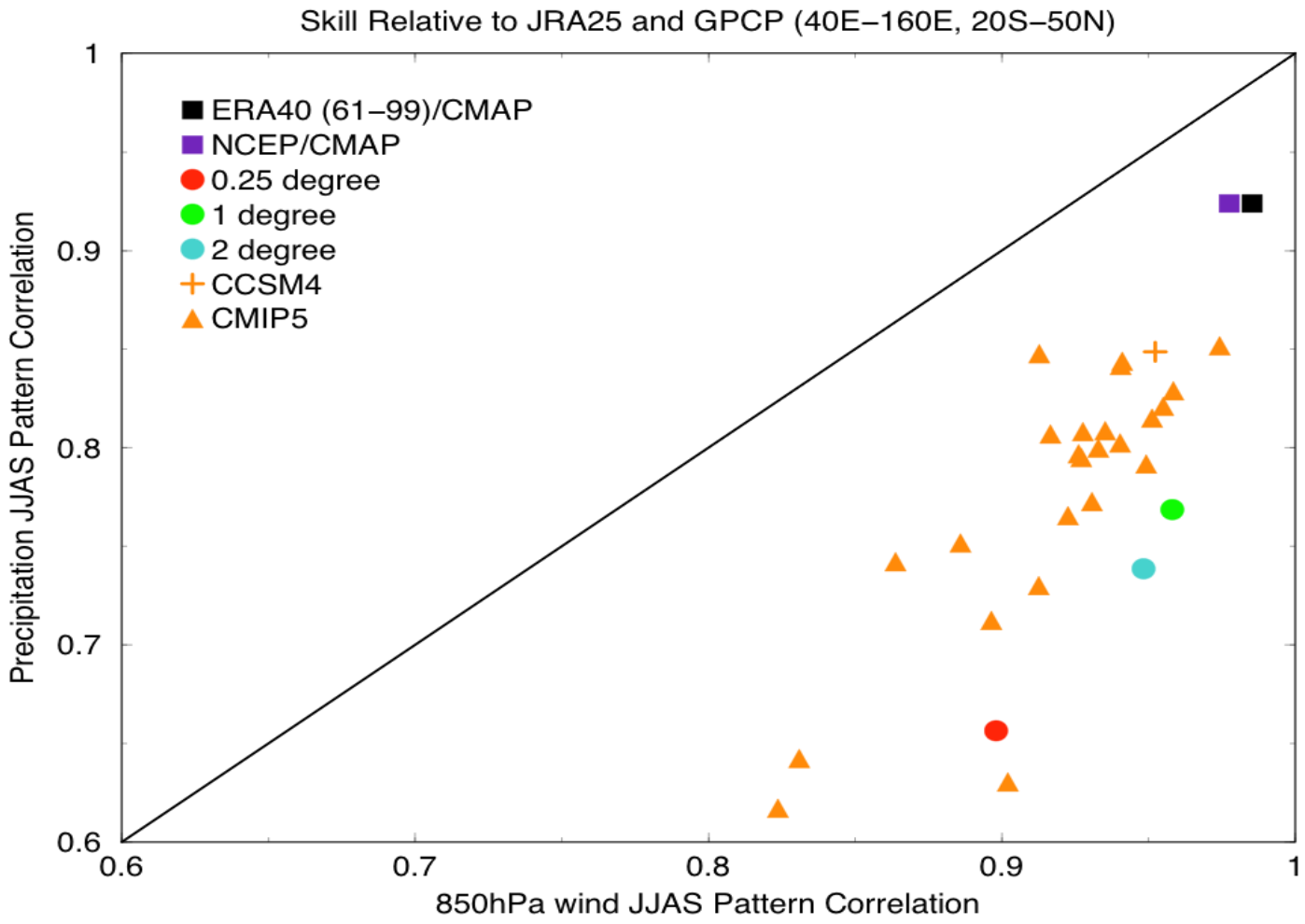

Figure 1. Pattern correlation skill scores of the June-Sept. climatologies of precipitation and 850hPa wind for observations, CCMS4, three versions of CAM5.1 that differ in horizontal resolution, and the CMIP5 models for the region 40°E-160°E, 20°S-50°N (Sperber, personal communication, 2014).

But the tropics themselves have multiple timescales

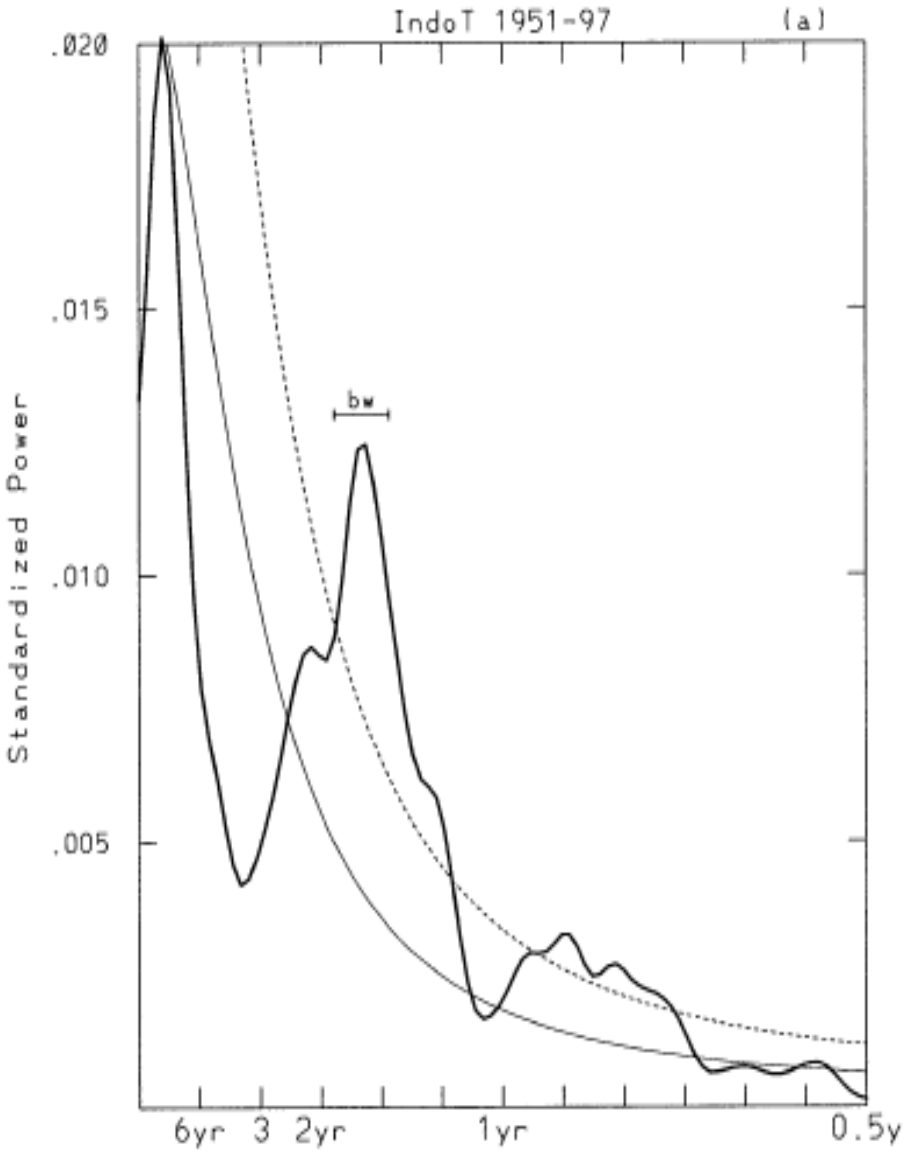

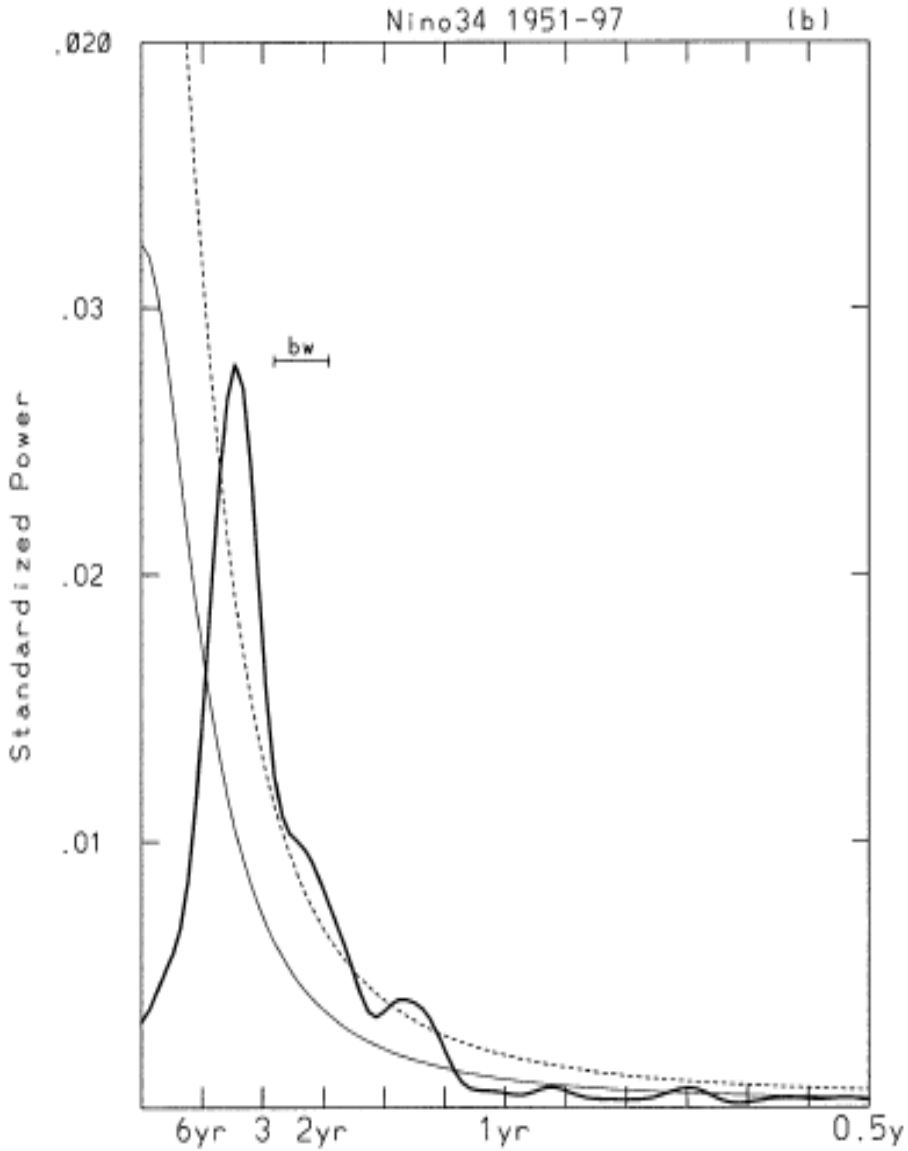

ITCZ – Cold Tongue Complex and Meridional Modes
But what is the relation between Zonal and Meridional Modes?

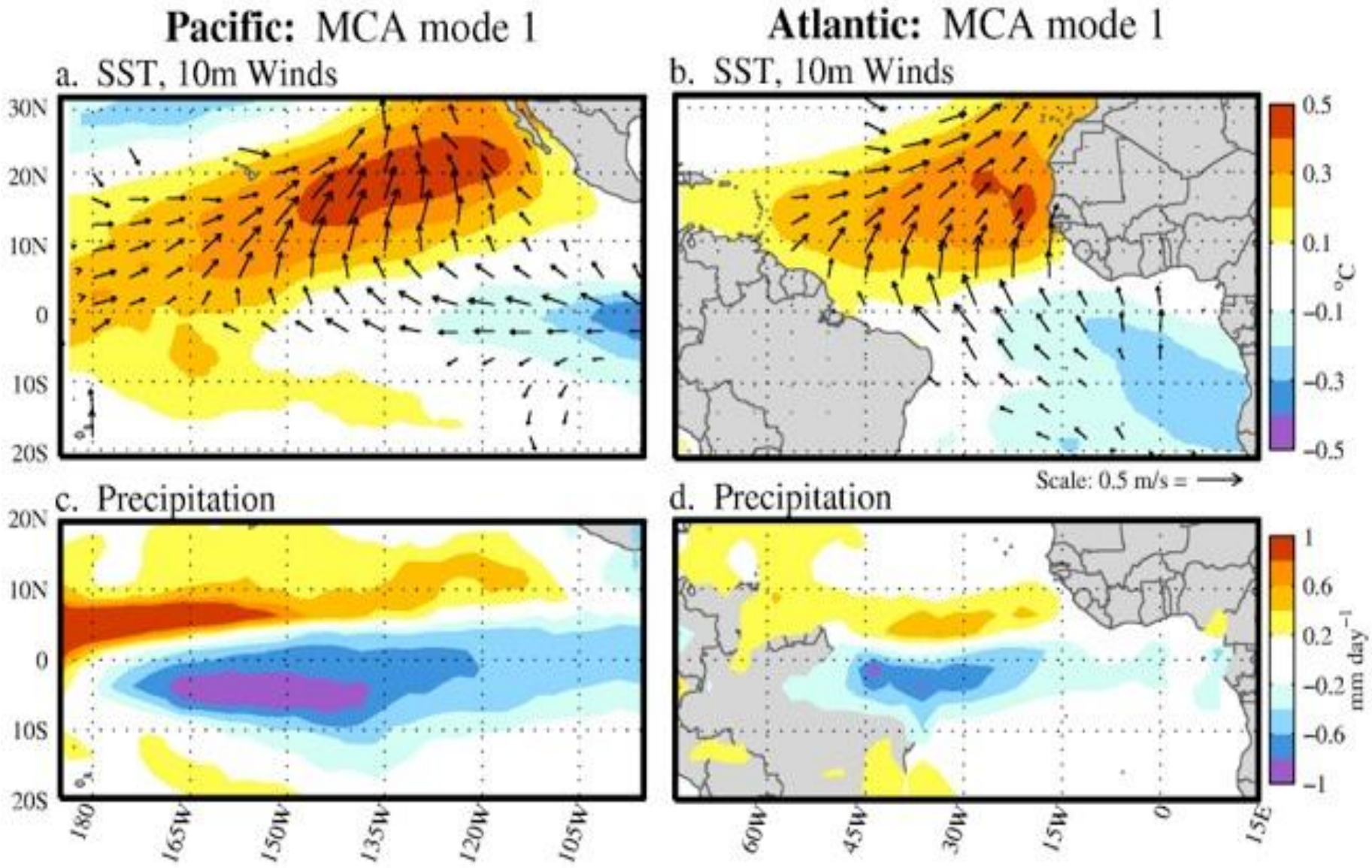

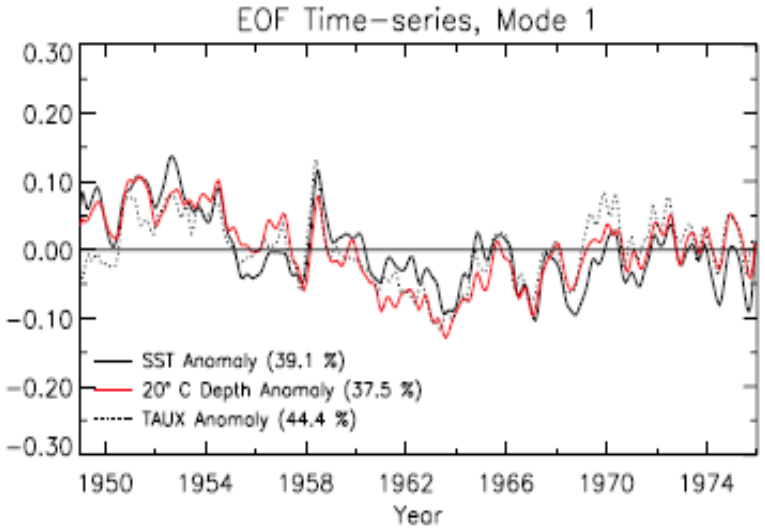

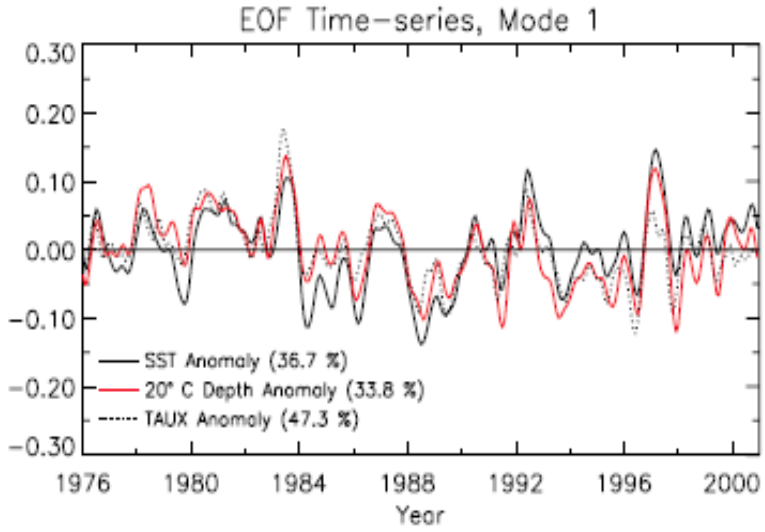

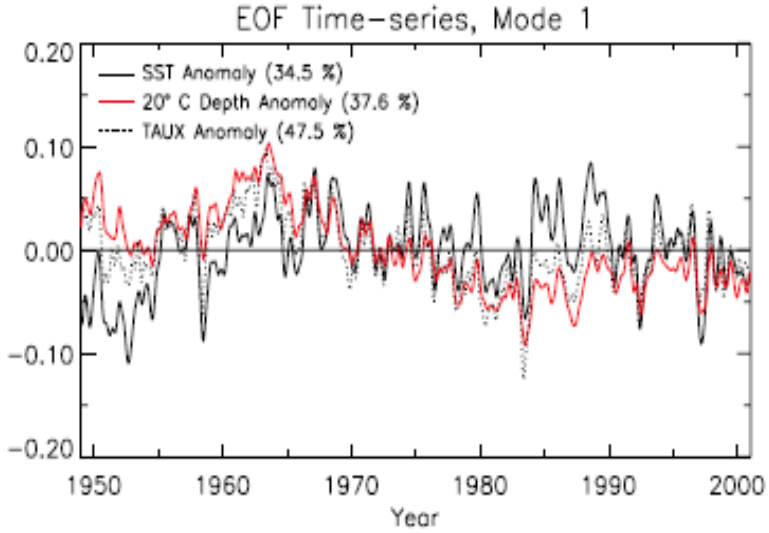

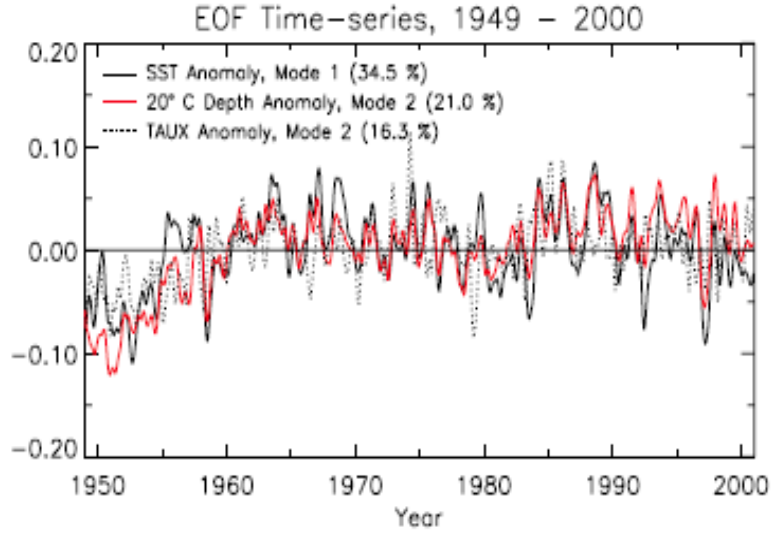

Zonal and Meridional Modes and the ITCZ in the tropical Atlantic. What is the role of Regime Shifts?

Seasonal cycle of the ITCZ position in the Atlantic (+/- 1 StD)

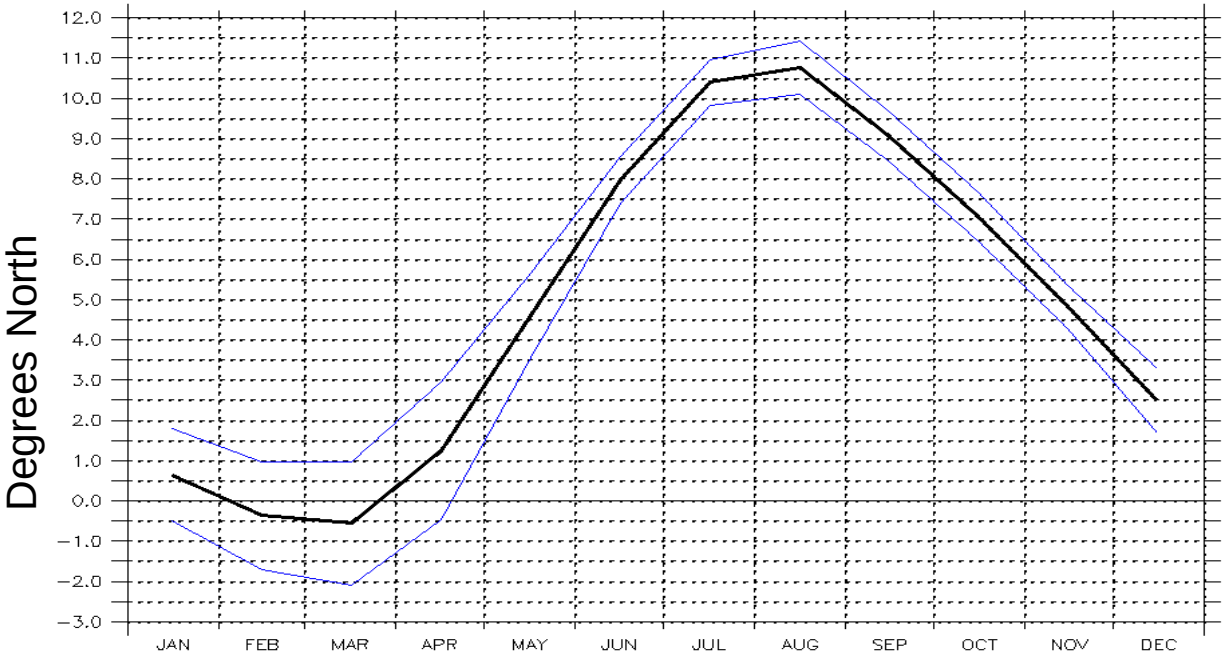

Data:ERA-Interim
Period:1979-2013

Climatological position

+/- 1 StD

Evolution of ITCZ position during the years when MAM ITCZ is anomalously away (North / South) from its climatological position

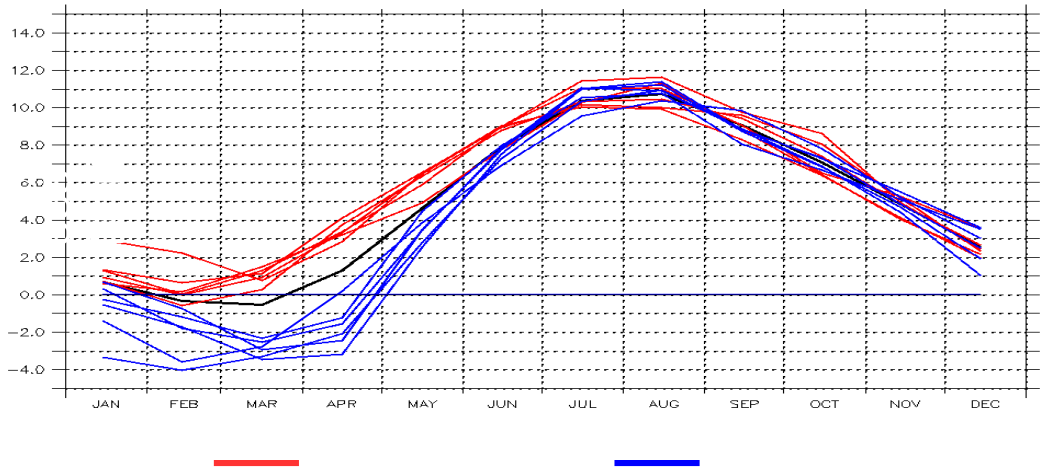

Composites of anomalies of MAM SST and OLR (winds overlaid) when MAM ITCZ North/South

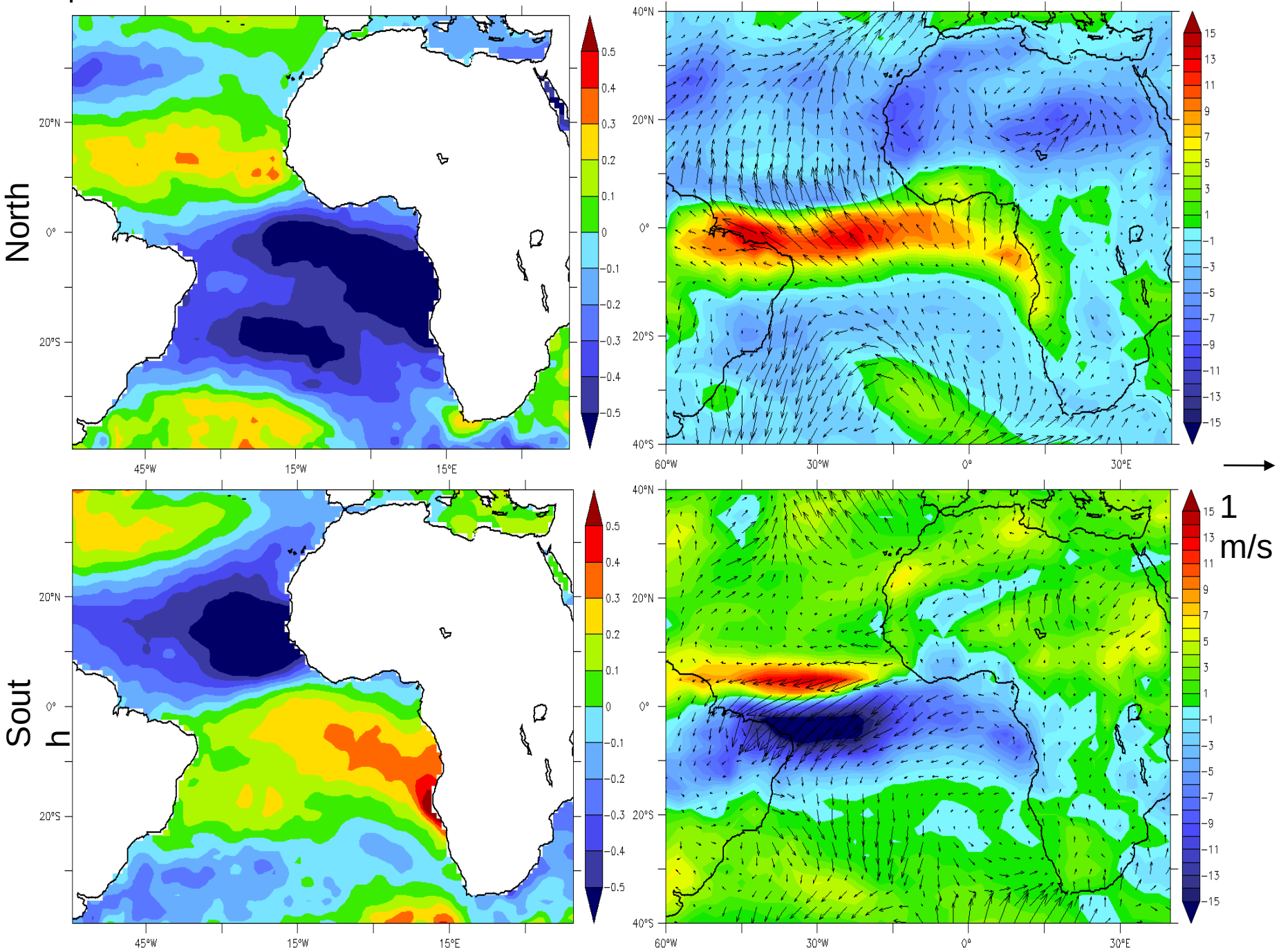

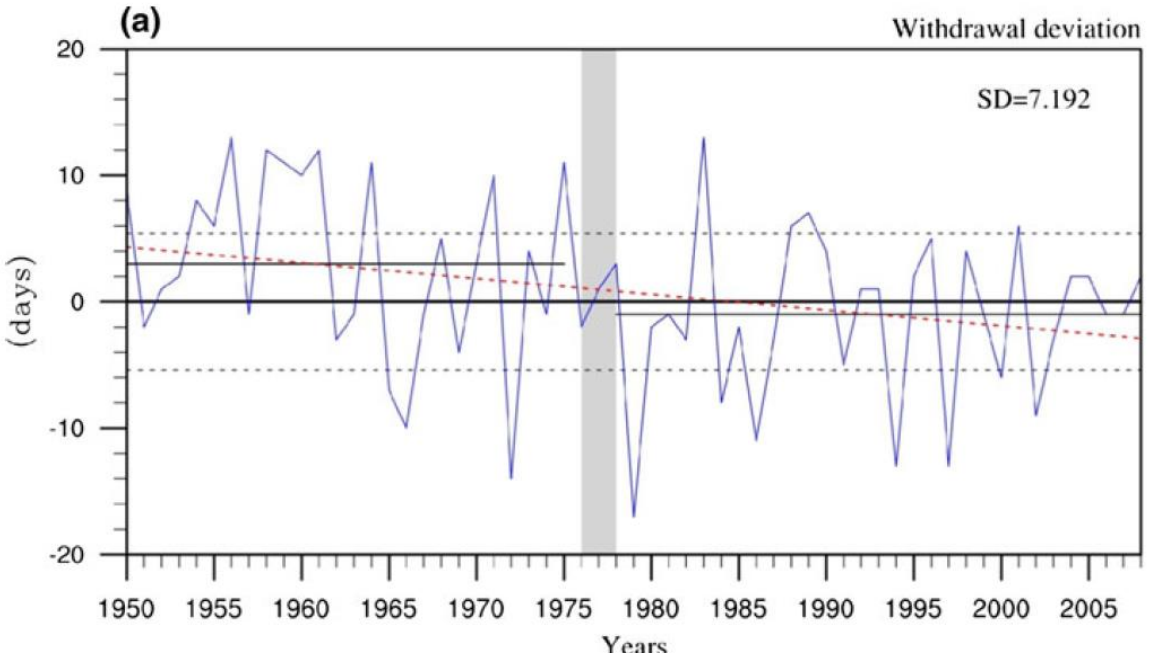

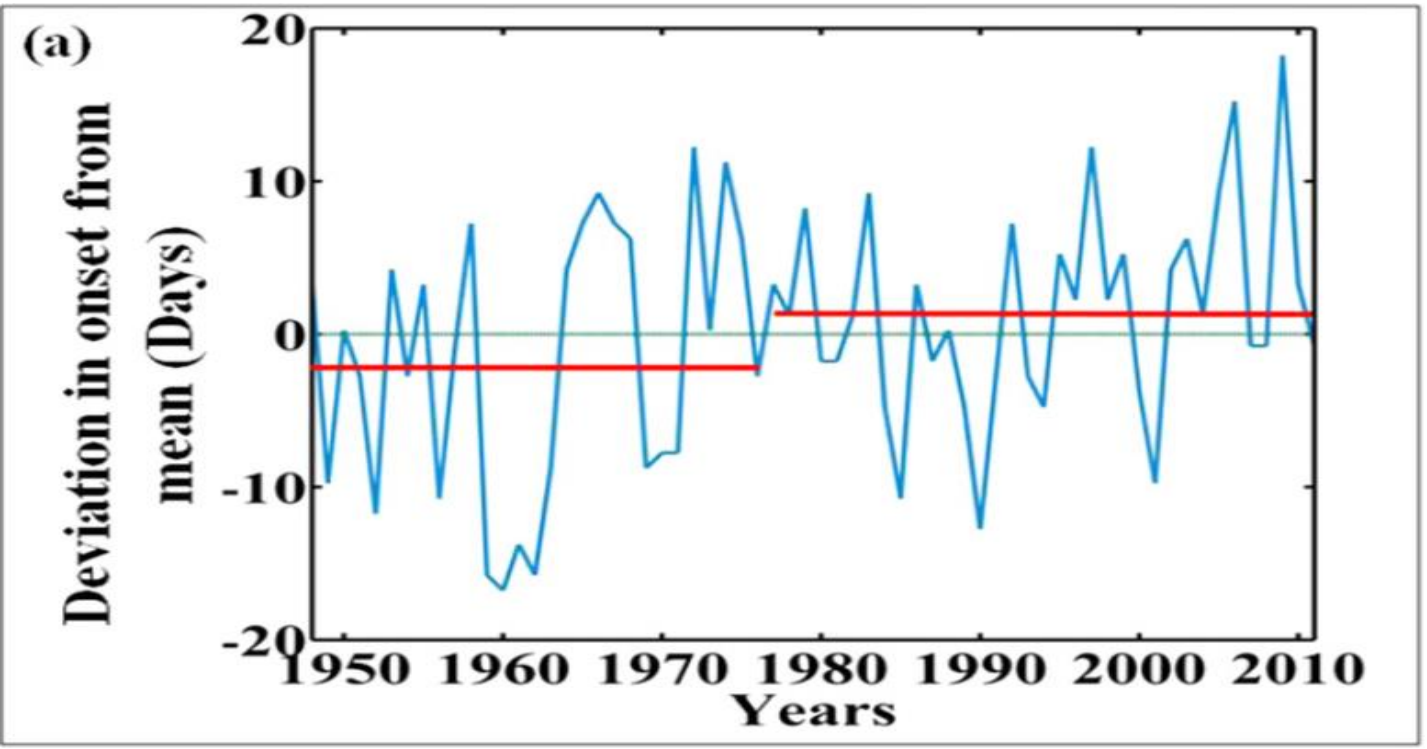

Returning to the Indian Monsoon:

Are the onset and withdrawal weather events? How are other timescales related to the onset and withdrawal?

Relation between Onset and Northward Propagating Systems

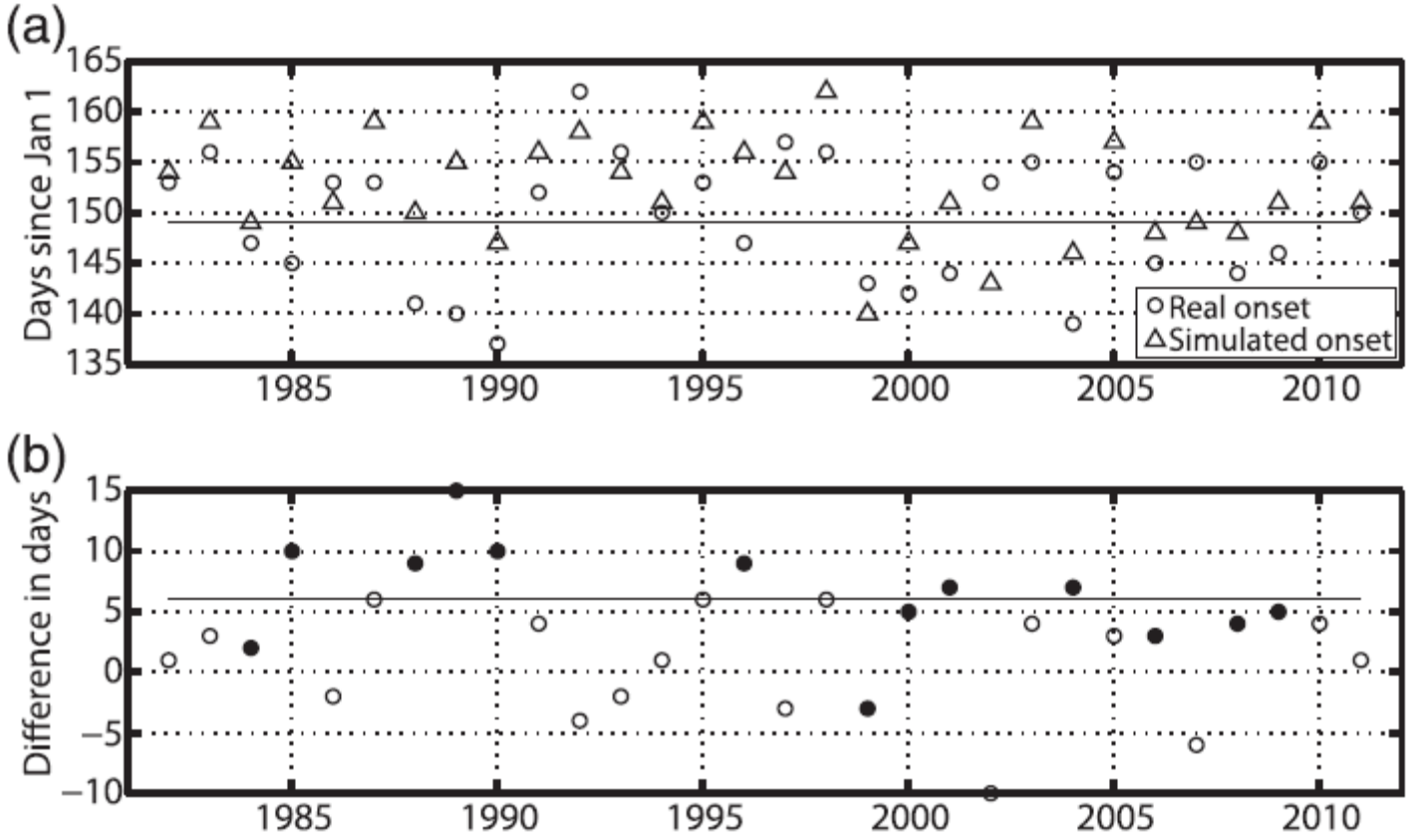

FIG. 1. (a) Circles denote onset dates of ISM defined with daily TT index from 1982 to 2011. Triangles denote onset dates of ISM based on simulated TT index (see text for details). The horizontal line marks the mean of onset dates. (b) Differences between real and simulated onset dates in (a). Solid circles denote the years with an onset date earlier than the mean onset date, and open circles denote all the other years. The horizontal line marks the std dev of the differences in onset dates.

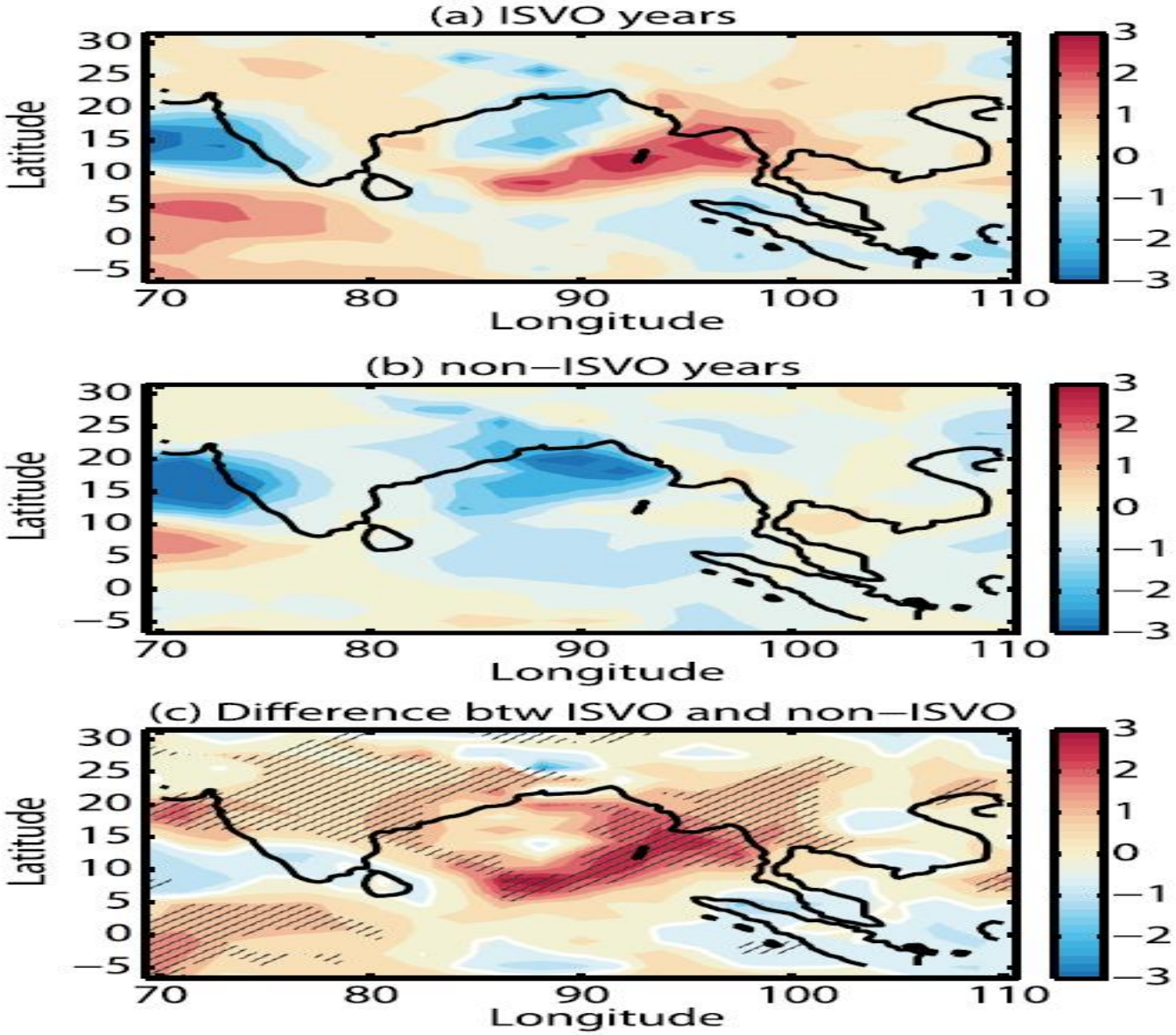

FIG. 4. (a) Intraseasonal convective precipitation anomalies (10^{-5} kg m^{-2} s^{-1}; averaged from the ISM onset day to 10 days before the onset day) for the ISVO years. (b) As in (a), but for the non-ISVO years. (c) Differences in the intraseasonal convective precipitation anomalies between the ISVO and the non-ISVO years. The intraseasonal signals are obtained with a bandpass filter of 30–90 days. Significant differences at the significance level of 99% are hatched. Zero is shown with white contours.

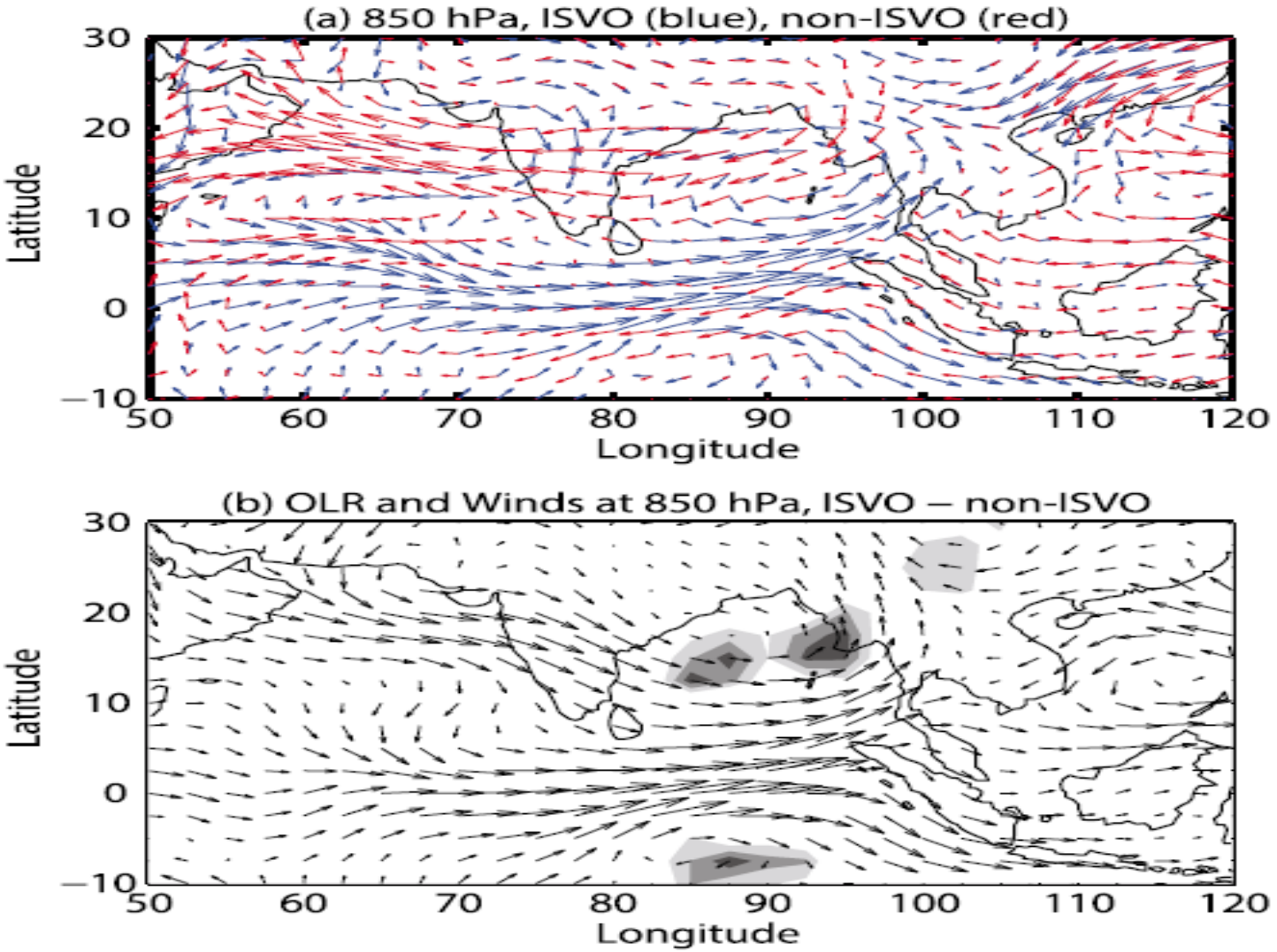

FIG. 5. (a) Winds at 850 hPa 1 day before the onset of ISM. Blue arrows represent the composite of the early onset years, while red arrows represent the composite of the other years. (b) Arrows give the differences of the winds at 850 hPa between the early onset years and normal years. Gray shading gives the difference of OLR between the two categories of years. The shading contours start at $-10\,\mathrm{W\,m^{-2}}$ (lightest gray) with an interval of $-2\,\mathrm{W\,m^{-2}}$.

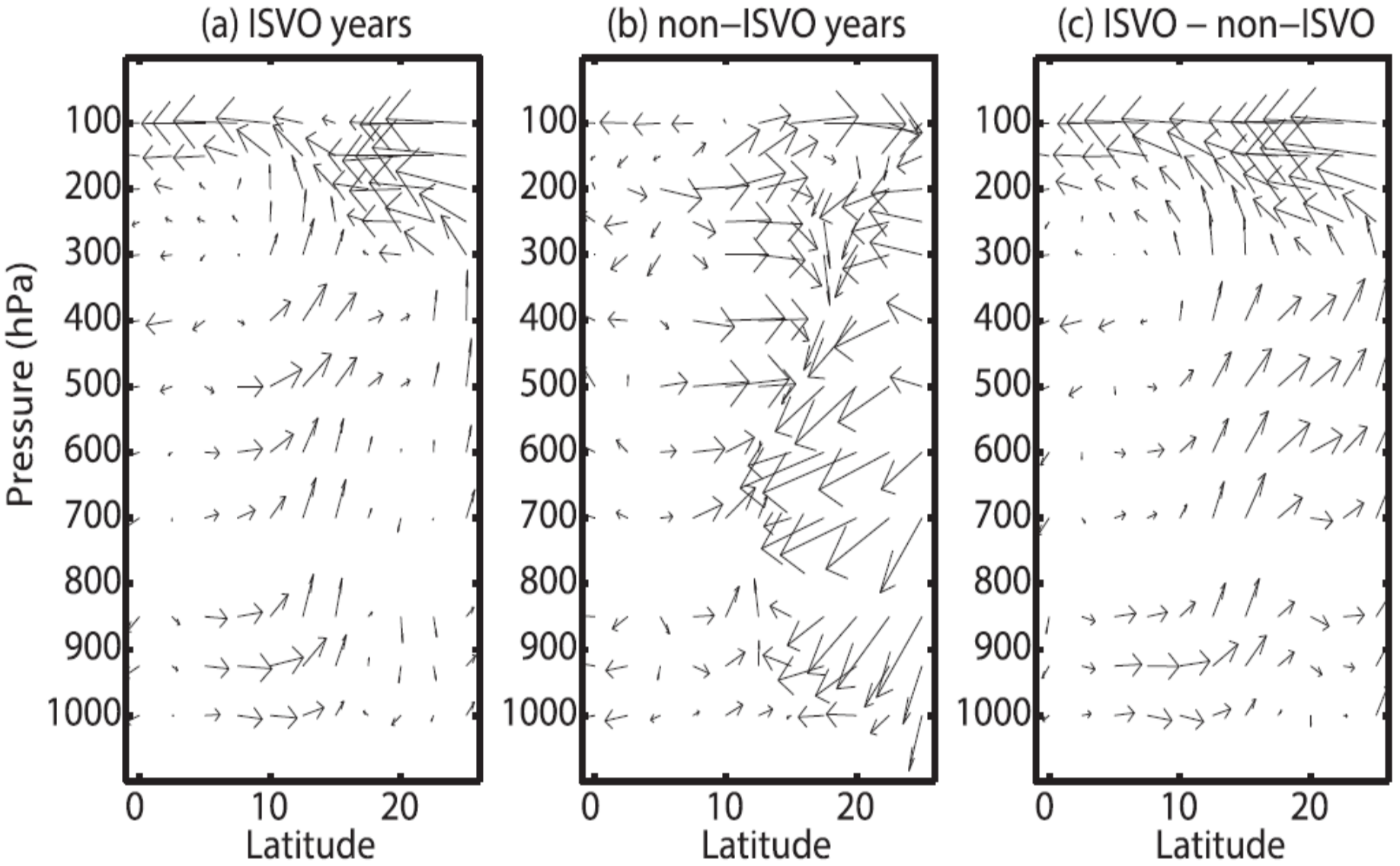

FIG. 6. (a) The meridional and pressure velocities 1 day before the onset date averaged between 85° and 100°E in the ISVO years. (b) As in (a), but for the non-ISVO years. (c) As in (a), but for the differences between the ISVO and non-ISVO years.

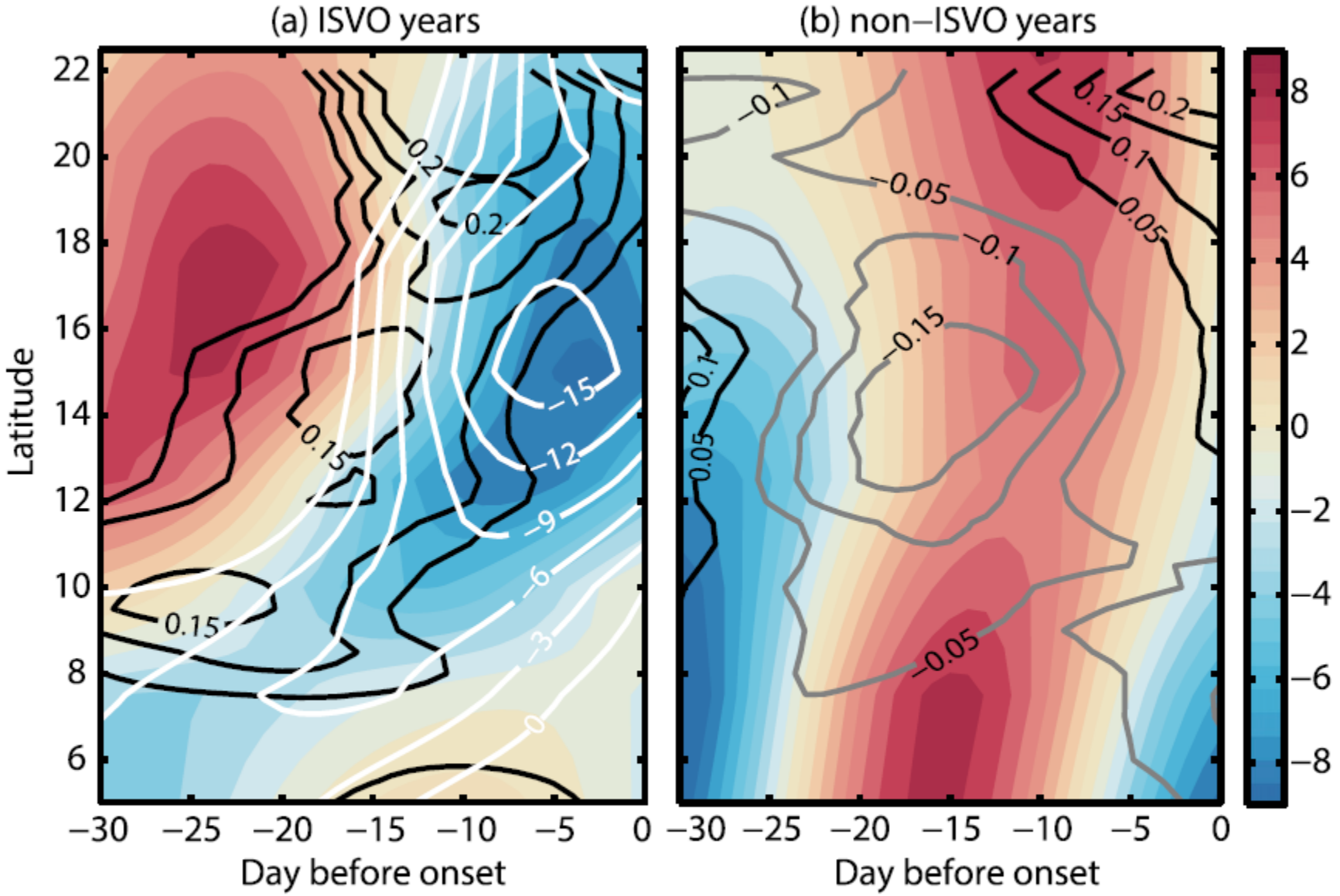

FIG. 8. (a) As in Fig. 7a, but for the intraseasonal OLR anomalies ($W m^{-2}$; color shading), the positive intraseasonal SST anomalies (K; black contours), and GMS ($kg m^{-2}$; white contours). (b) As in Fig. 7a, but for the intraseasonal OLR anomalies ($W m^{-2}$; color shading), the positive intraseasonal SST anomalies (K; black contours), and negative intraseasonal SST anomalies ($kg m^{-2}$; gray contours).

Early monsoon onset is related to the strength of northward propagating systems

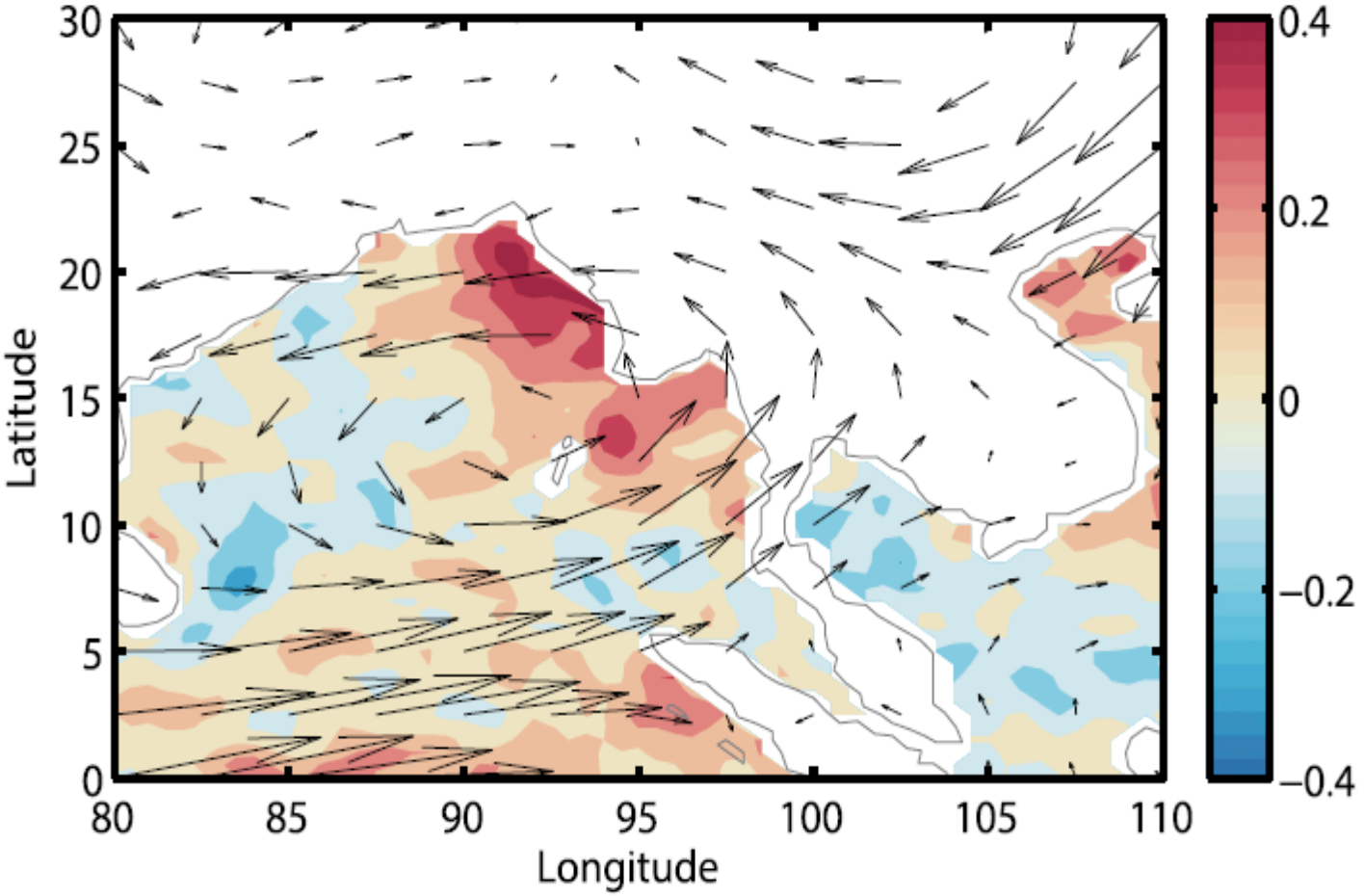

FIG. 9. Intraseasonal wind anomalies at 850 hPa and intraseasonal SST anomalies on the onset dates of ISM in the ISVO years.

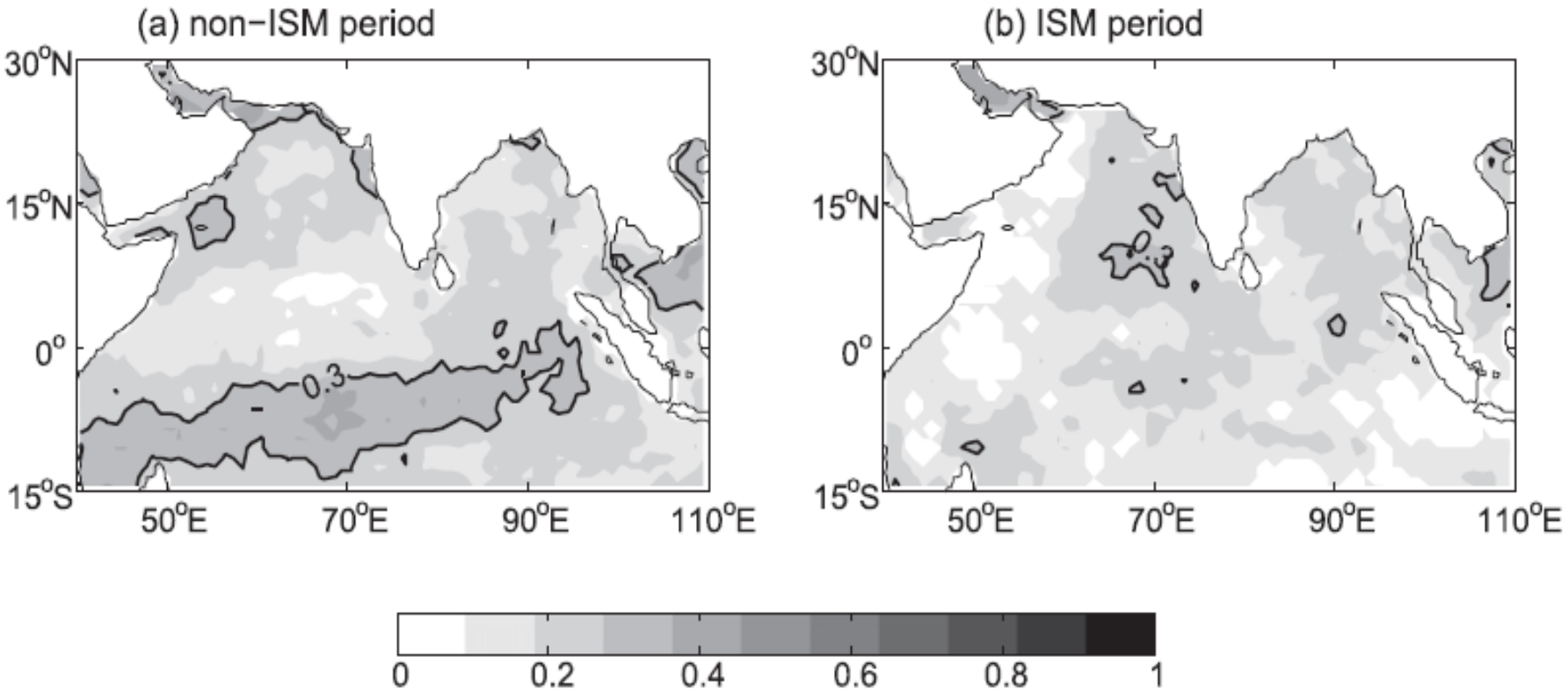

FIG. 1. Correlations in the intraseasonal band from 1998 to 2009 between downward Q'_{net} and $\partial \text{SST}'/\partial t$ for the (a) non-ISM and (b) ISM periods. The intraseasonal signals are obtained with a 5–90-day bandpass filter. Only statistically significant correlations at the 99% confidence level are shaded. The black solid contours represent the correlations larger than 0.3, with an interval of 0.2. The mean effective sample size is 426, and the threshold for the 99% confidence level is 0.1127 (Bretherton et al. 1999).

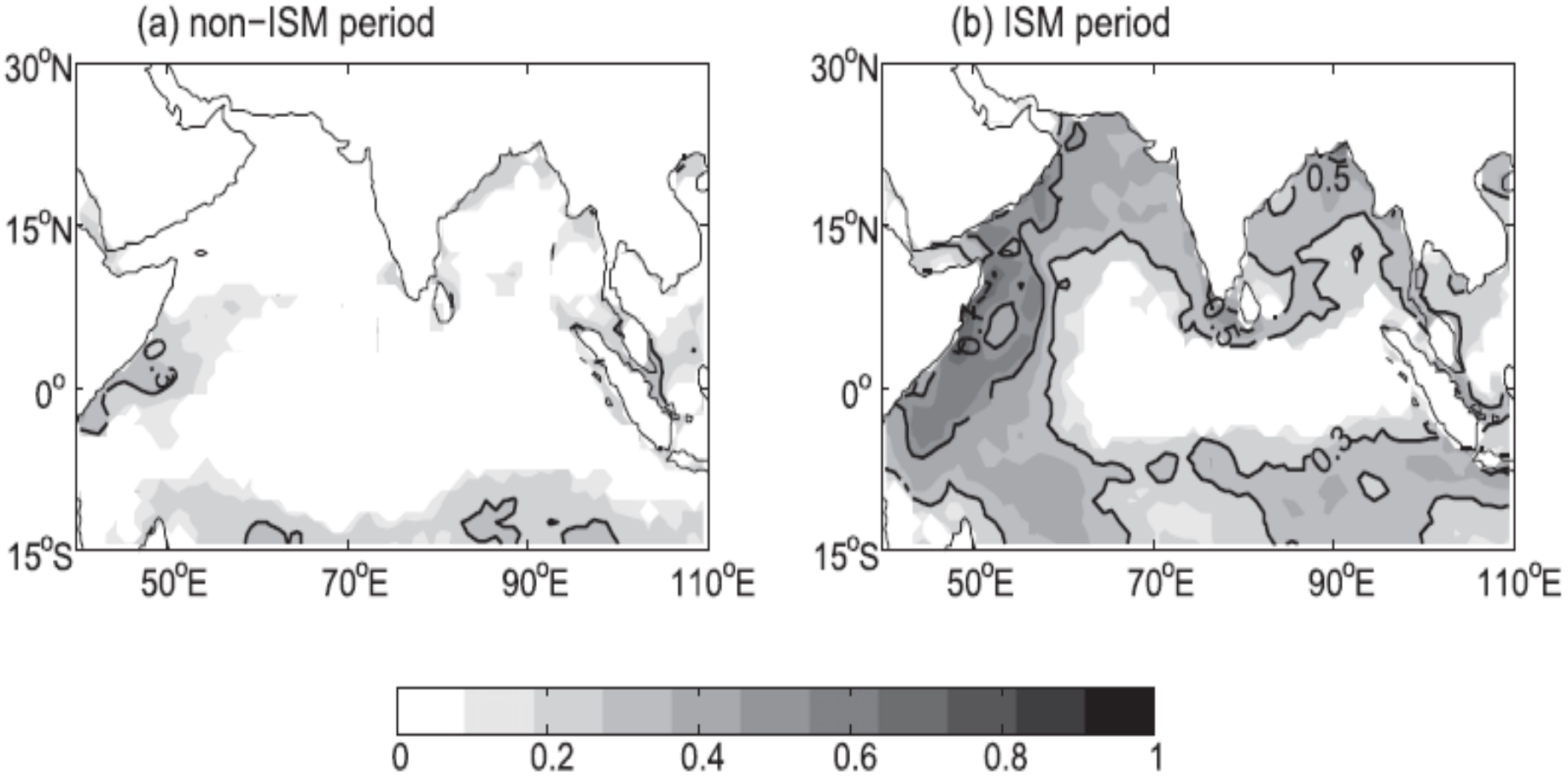

FIG. 2. As in Fig. 1, but for correlations between upward $Q'_{LH} + Q'_{SH}$ and SST′ in the intraseasonal band. The mean effective sample size is 246, and the threshold for the 99% confidence level is 0.1482 (Bretherton et al. 1999).

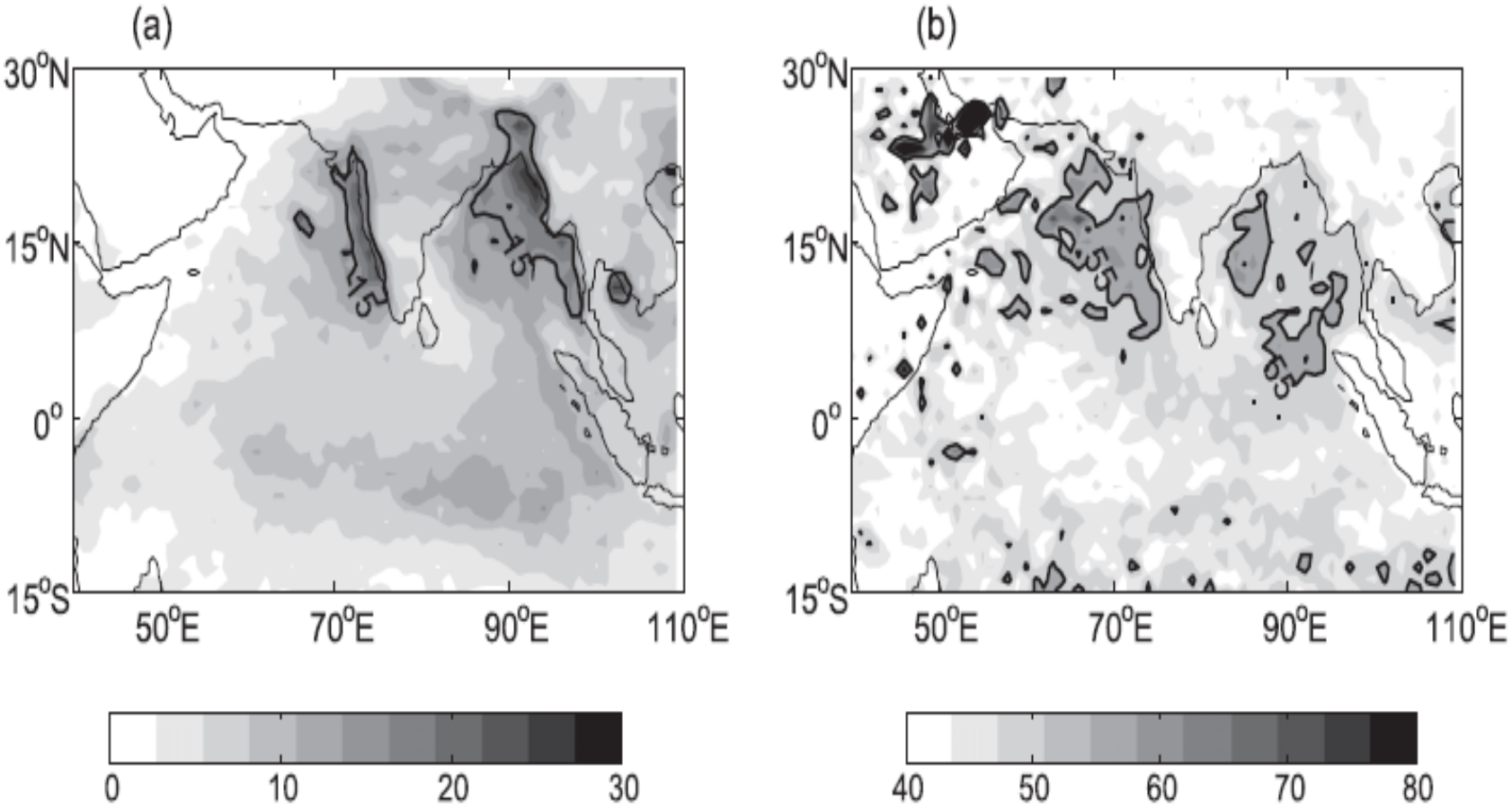

FIG. 3. (a) Std dev of intraseasonal precipitation (mm day^{-1}) during the ISM from 1998 to 2009. The black contours represent std devs larger than 15 mm day^{-1}. (b) Ratios between the variance of the intraseasonal rainfall and the variance of the total rainfall (%). The black contours represent 55%.

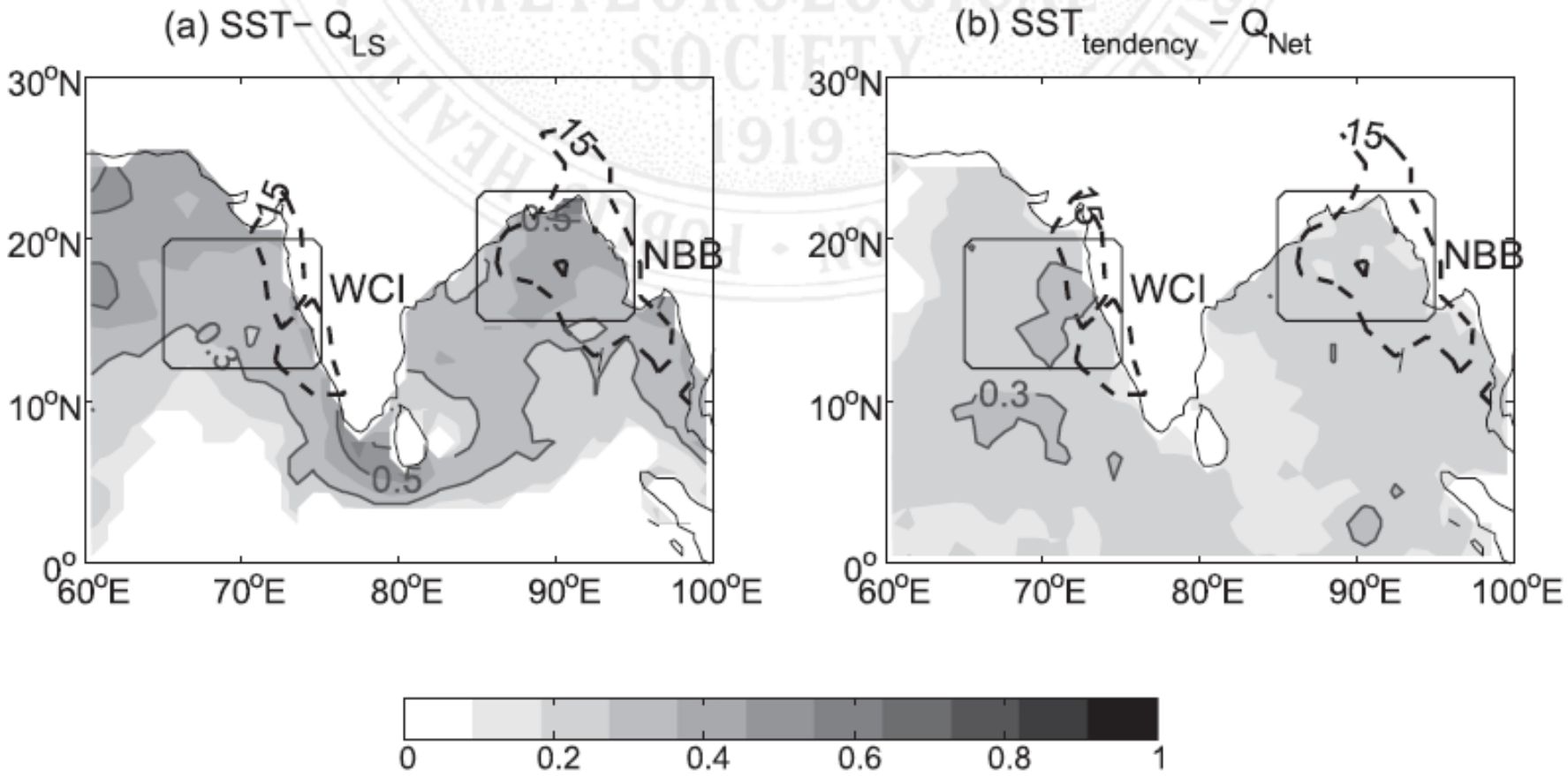

FIG. 4. Correlations in the intraseasonal band during May–August between (a) SST′ and upward $Q'_{LH} + Q'_{SH}$ and between (b) $\partial SST'/\partial t$ and downward Q'_{net}. Only statistically significant correlations at the 99% confidence level are shaded. The black solid contours represent the correlations larger than 0.3, with an interval of 0.2. The black dotted contours represent std devs of precipitation larger than 15 mm day^{-1}, with an interval of 10 mm day^{-1}. The two selected regions—WCI (12°–20°N and 65°–75°E) and NBB (15°–23°N and 85°–95°E)—are denoted by black boxes.

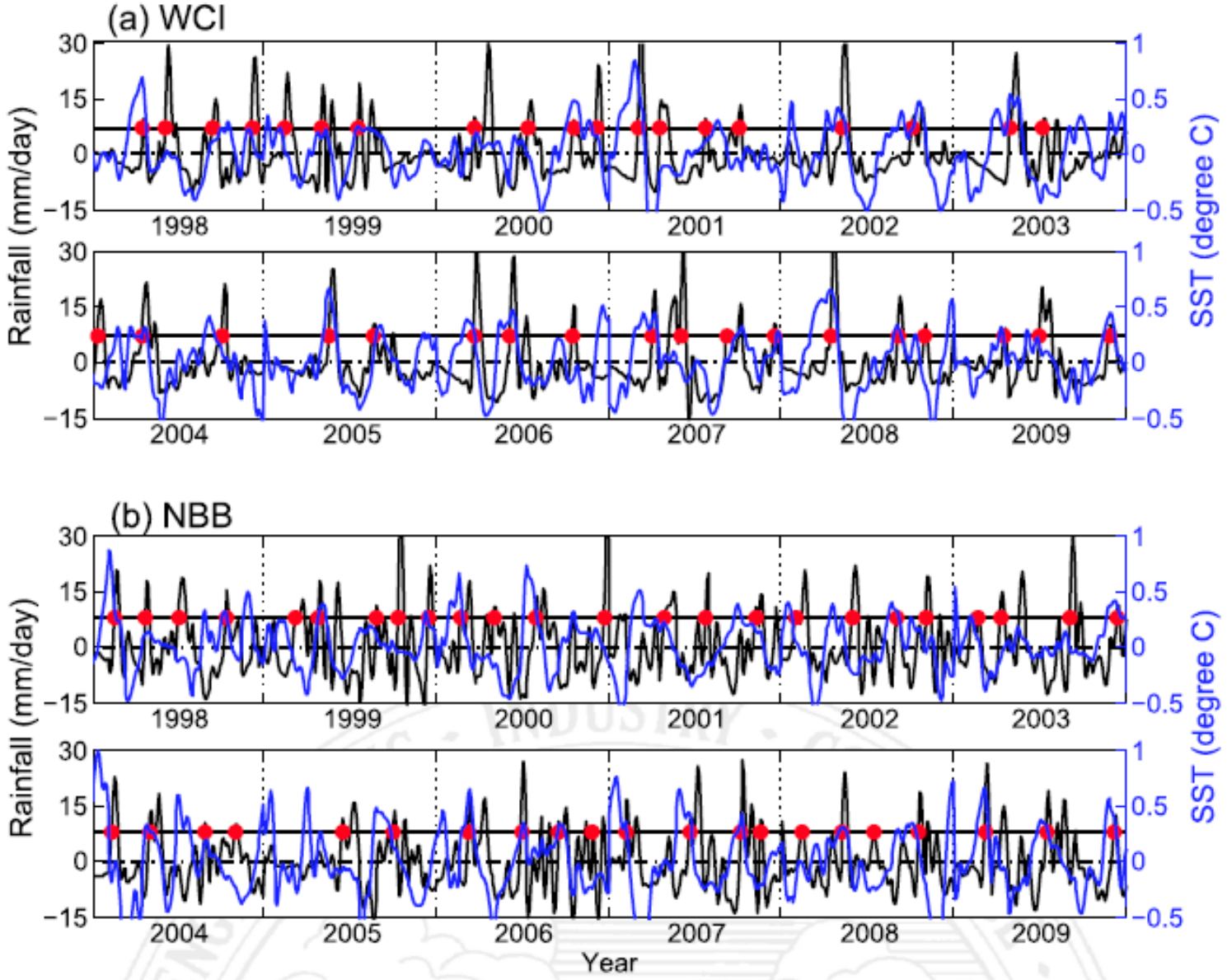

FIG. 5. Regional mean intraseasonal precipitation (mm day^{-1}; black solid curves) and intraseasonal SST anomalies (°C; blue solid curves) in (a) WCI and (b) NBB. The time mean of precipitation (black dotted lines) and one std dev above the mean (black solid lines) are superimposed. The beginning of each heavy precipitation event is marked with a red dot.

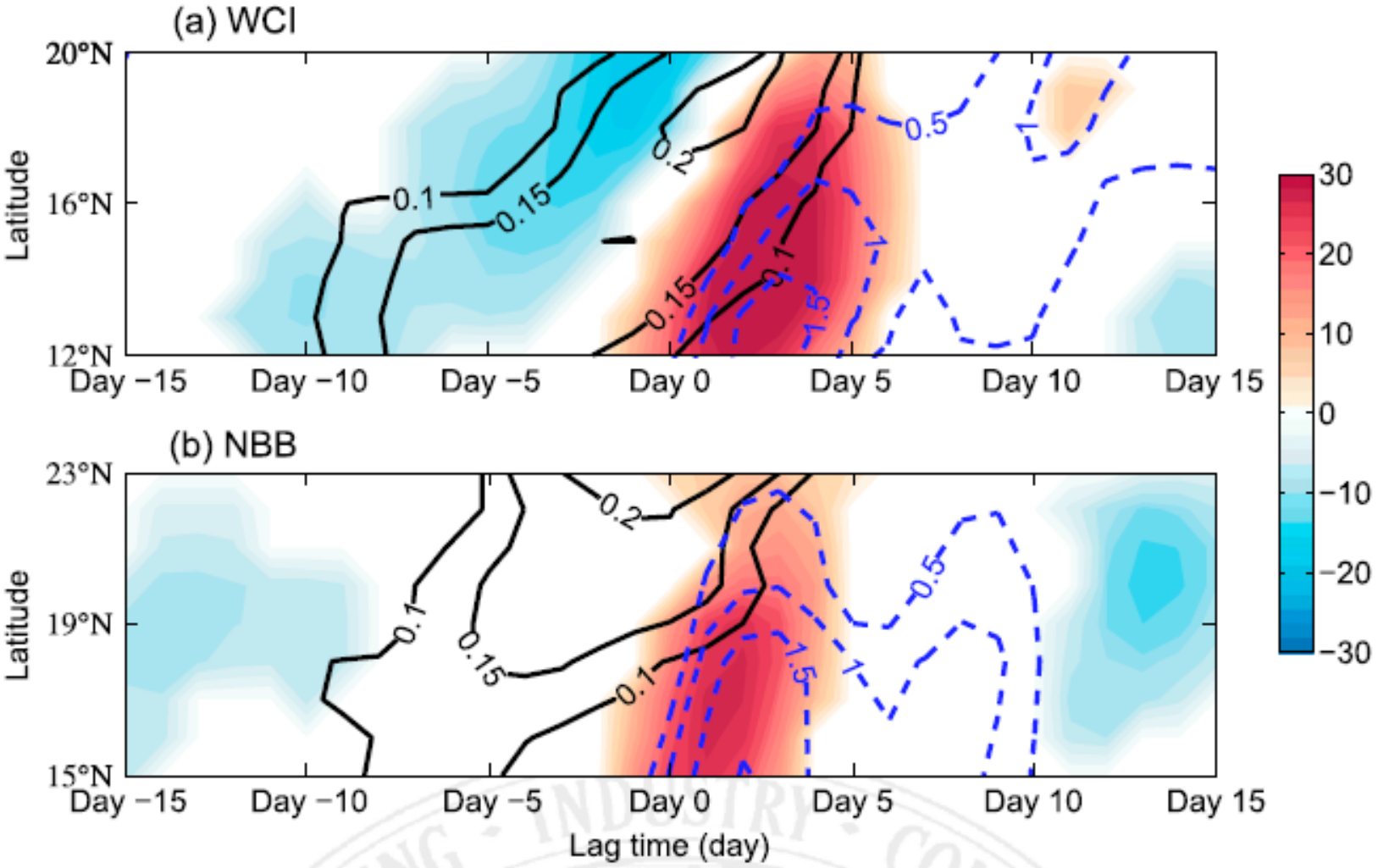

FIG. 6. Hovmöller diagrams of zonal mean intraseasonal latent heat flux anomalies ($W\ m^{-2}$; color shaded), positive SST anomalies (°C; black solid lines), and positive wind anomalies ($m\ s^{-1}$; blue dashed lines) in (a) WCI and (b) NBB for the composite heavy precipitation events. All the composites are significant at the 95% confidence level. Day 0 is when the heavy precipitation event begins.

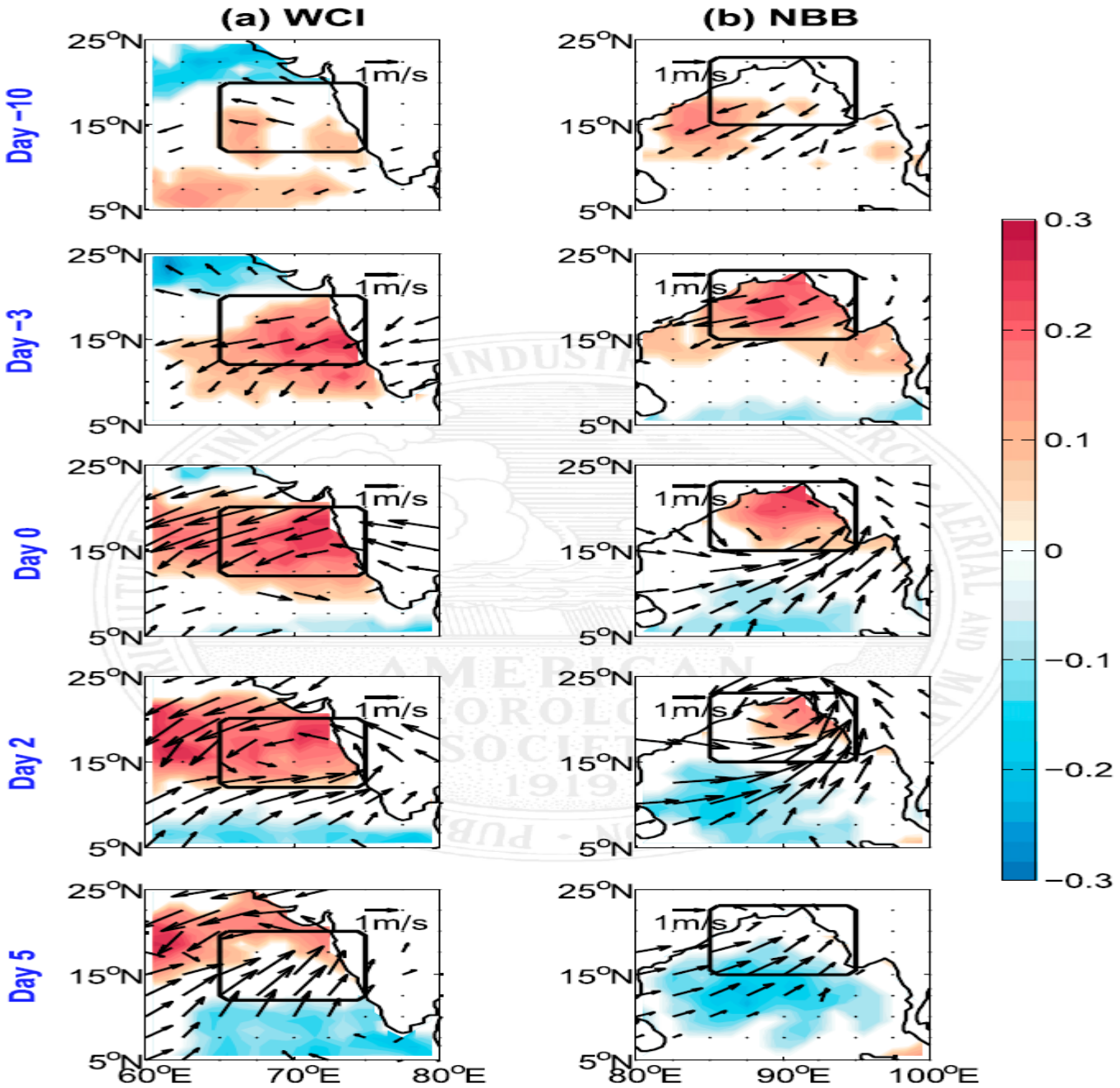

FIG. 7. Intraseasonal SST anomalies (°C; color shaded) and surface wind anomalies (m s^{-1}; black vectors) for the heavy precipitation events in (a) WCI and (b) NBB. Day 0 is when the composite heavy precipitation event begins. The two selected regions of WCI and NBB are marked with black boxes. All the composites are significant at the 95% confidence level.

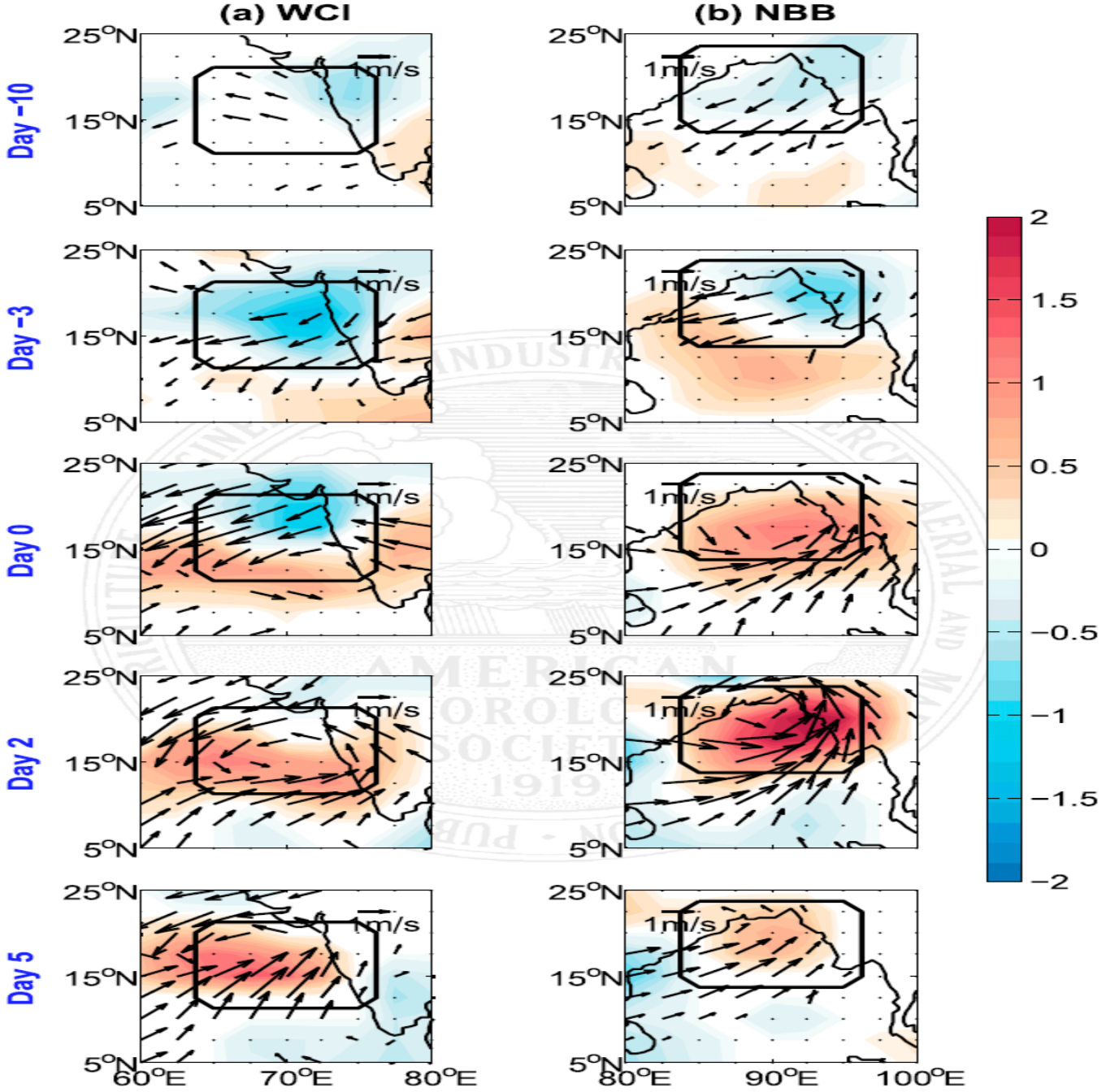

FIG. 8. As in Fig. 7, but for the intraseasonal vertical moisture advection $-(\omega\partial q/\partial p)'$ (g kg^{-1} day^{-1}; color shaded) and surface wind anomalies (m s^{-1}; black vectors). All variables are at 850 hPa, and all the composites are significant at the 95% confidence level.

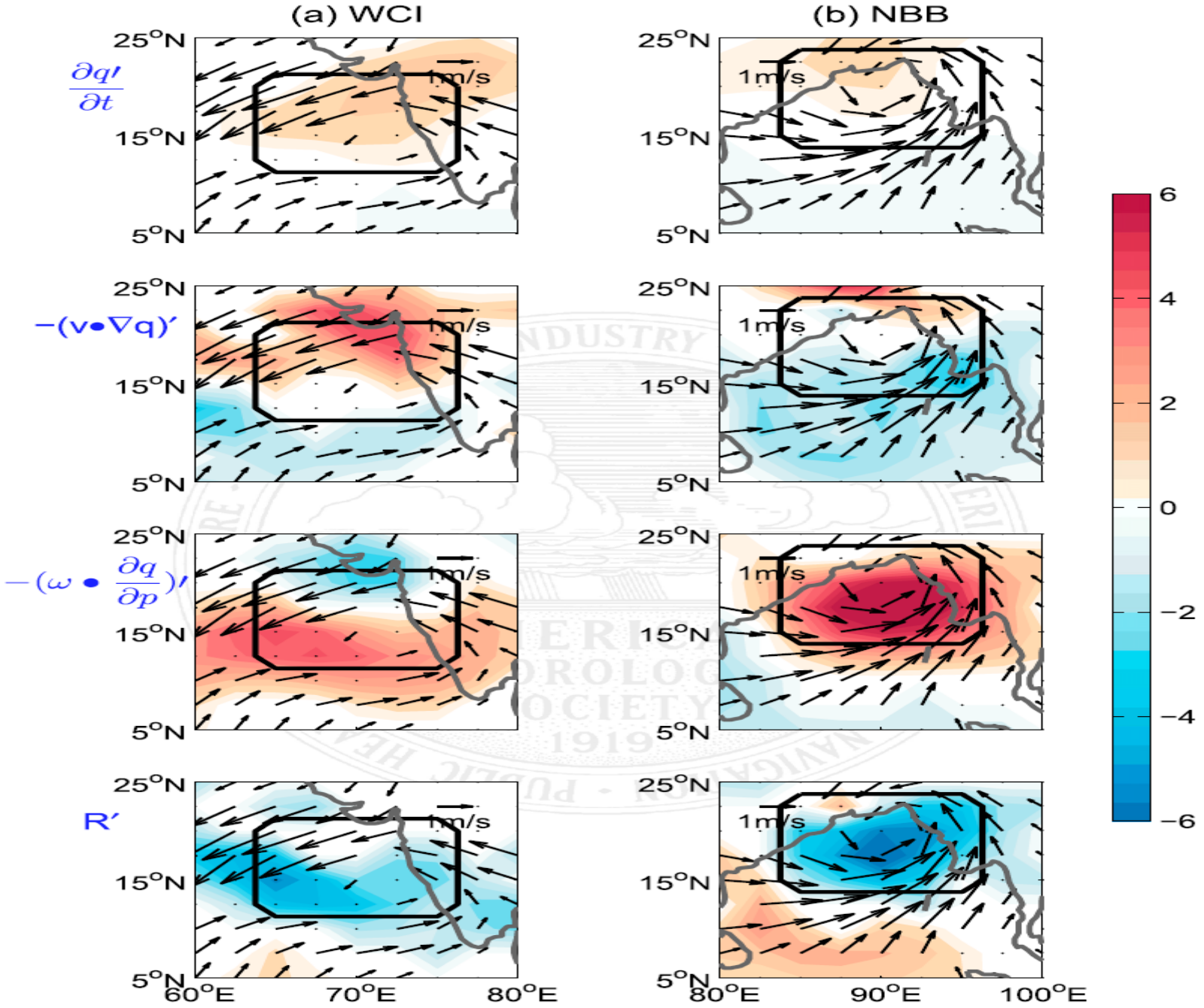

FIG. 9. As in Fig. 7, but for all terms in the moisture budget (kg m^{-2} day^{-1}) averaged from day 0 to day 2. All terms are vertically integrated between 1000 and 300 hPa. The shown composites are significant at the 95% confidence level.

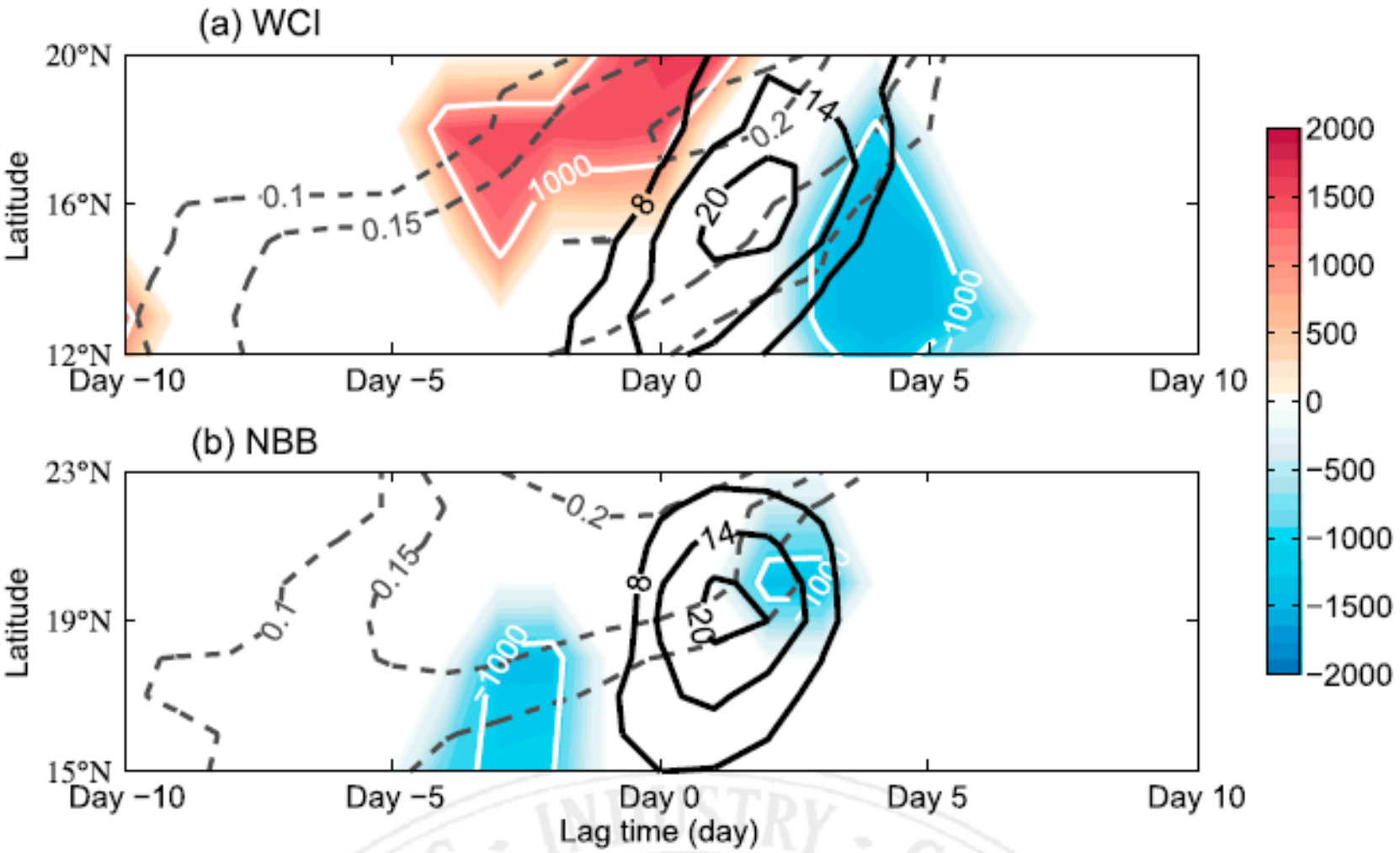

FIG. 10. Hovmöller diagrams of the zonal mean intraseasonal ΔMSE (J kg^{-1}; color shaded), positive SST anomalies (°C; gray dashed lines), and precipitation anomalies (mm day^{-1}; black solid lines) in (a) WCI and (b) NBB for the composite heavy precipitation events. All the composites are significant at the 95% confidence level. Day 0 is when the heavy precipitation event begins.

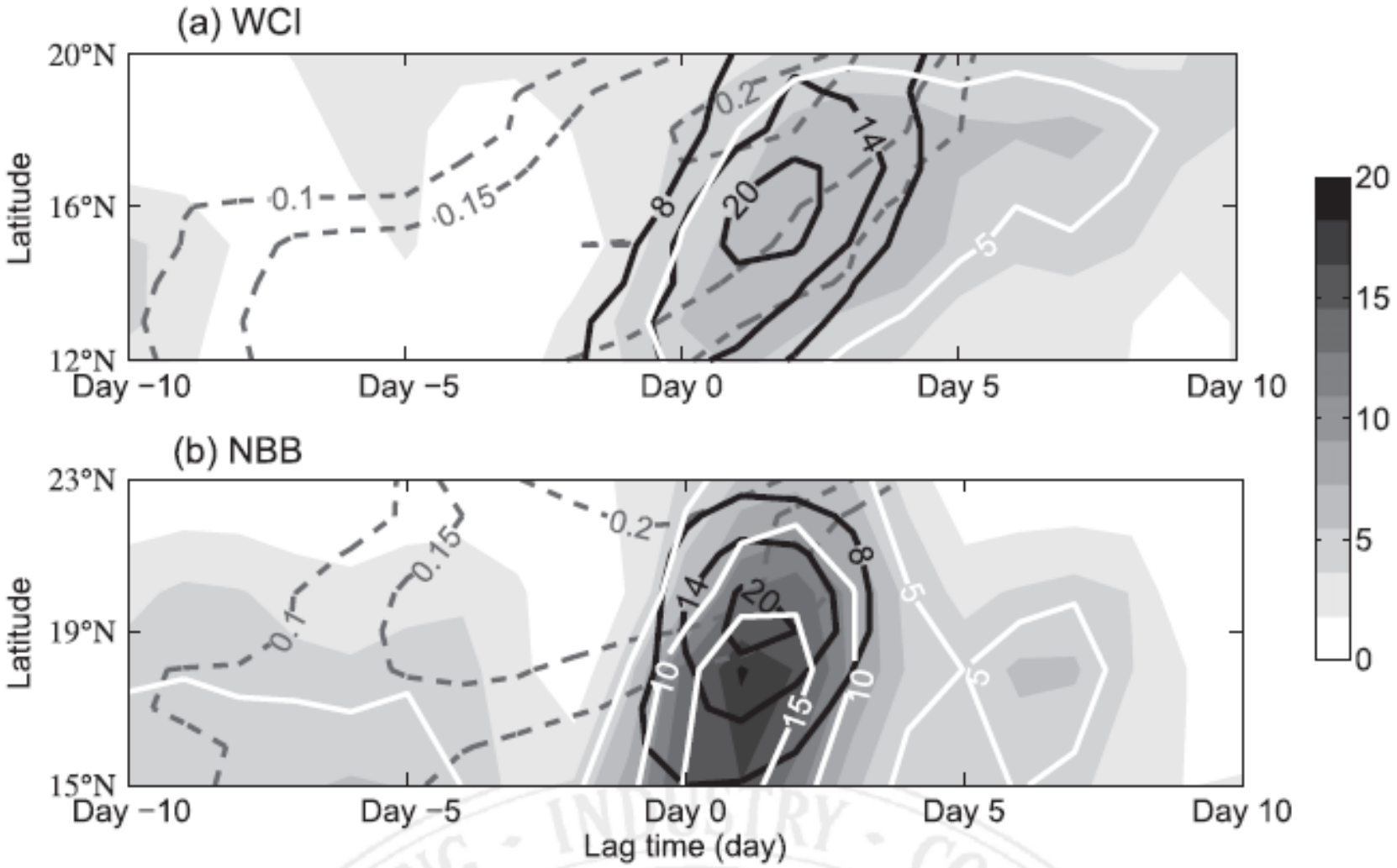

FIG. 11. As in Fig. 10, but for the zonal mean ($PE' \cdot KE'$) averaged from 1000 to 100 hPa (J day^{-1} kg^{-1}; shaded), positive SST anomalies (°C; gray dashed lines), and precipitation anomalies (mm day^{-1}; black solid lines).

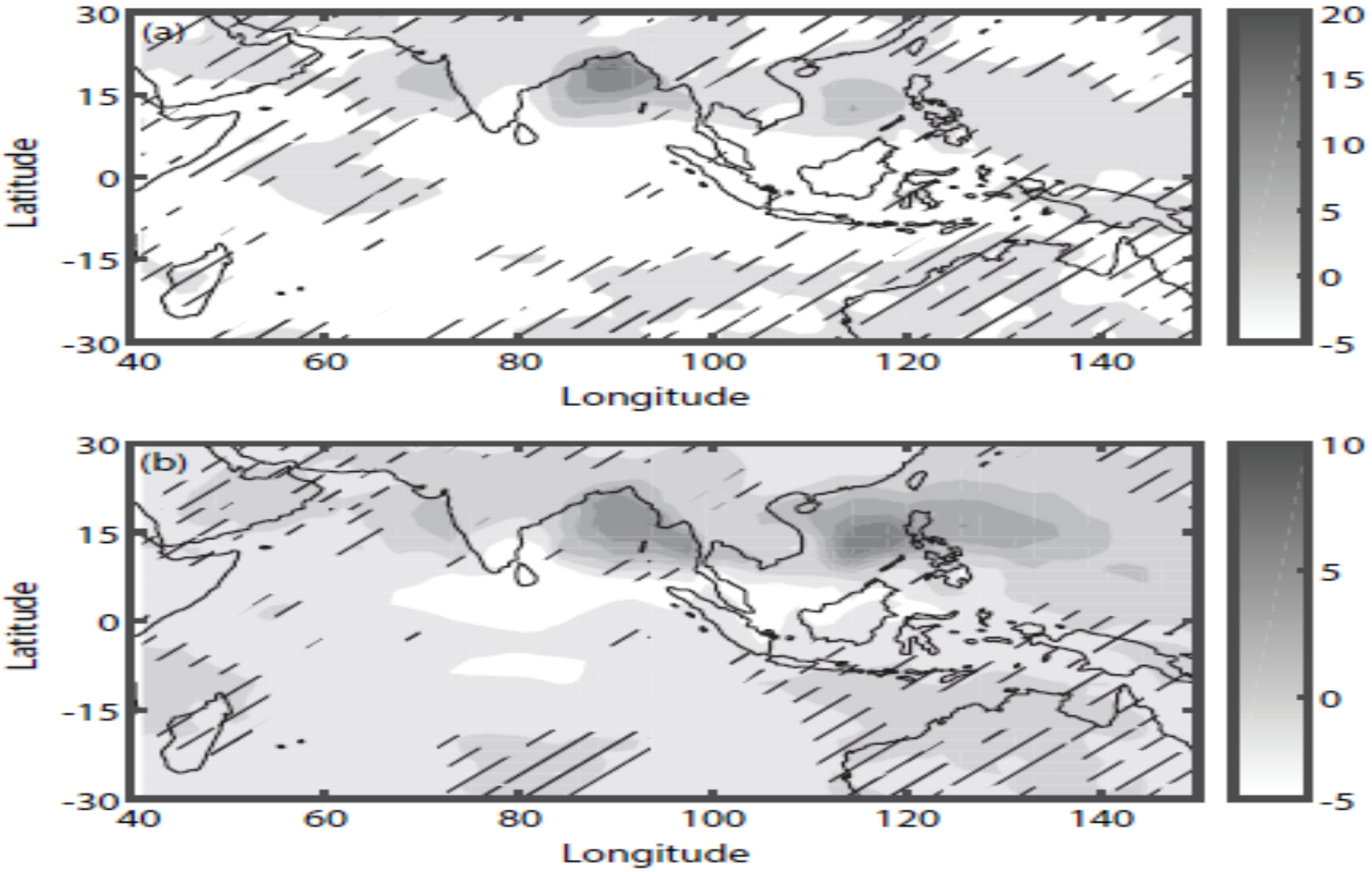

The differences in intraseasonal precipitation between the large- group and small-rainfall groups. (b) Same as (a), but for the differences between the positive and negative phases of the CIO mode. Units are 10^{-5} kg^2 m^{-2} s^{-1}. The differences in the areas with no hatch lines are statistically significant at a 95% confidence level.

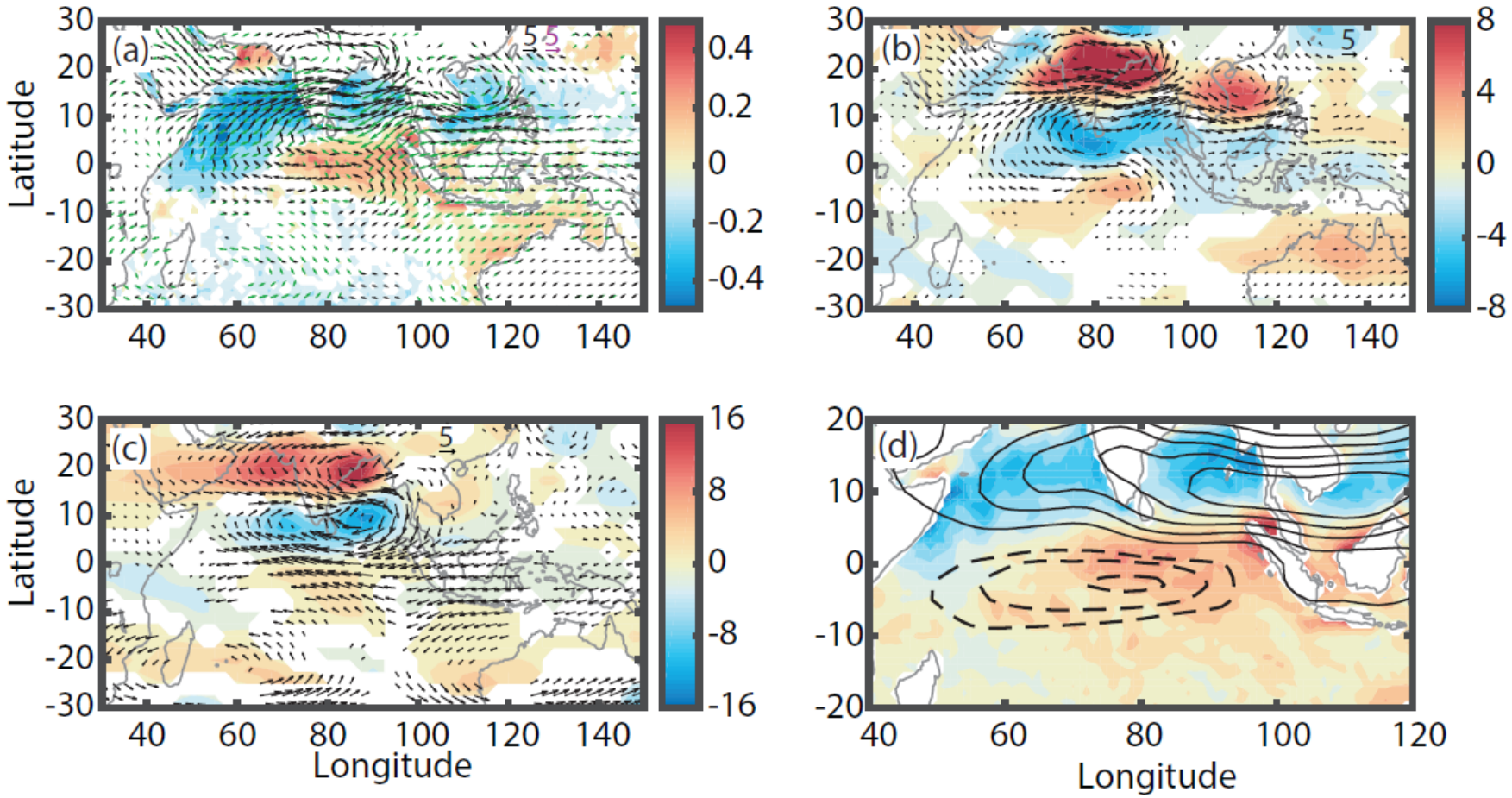

(a) The differences between the large- and small-rainfall groups in intraseasonal SST anomalies (colors, unit: °C), intraseasonal wind anomalies at 850 hPa (black vectors, unit: m s^{-1}), and vertical wind shear (green vectors, unit: kg m^{-2} s^{-1}). For clarity of depiction in (a), the directions of green vectors are opposite to the actual vertical wind shear. (b) The differences in intraseasonal PV anomalies at 850 hPa (colors, unit: 10^{-2} PVU; 1 PVU = 10^{-6} m^2 K s^{-1} kg^{-1}) and intraseasonal wind anomalies at 850 hPa (black vectors, unit: m s^{-1}). (c) Same as (b), but for the upper troposphere at 300 hPa. (d) The pattern of the positive CIO mode. Reddish (bluish) color denotes the positive (negative) node of the SST mode. Solid (dash) contours denote the positive (negative) node of the zonal wind mode. All colors and vectors shown in (a) – (c) are significant at a 95% confidence level.

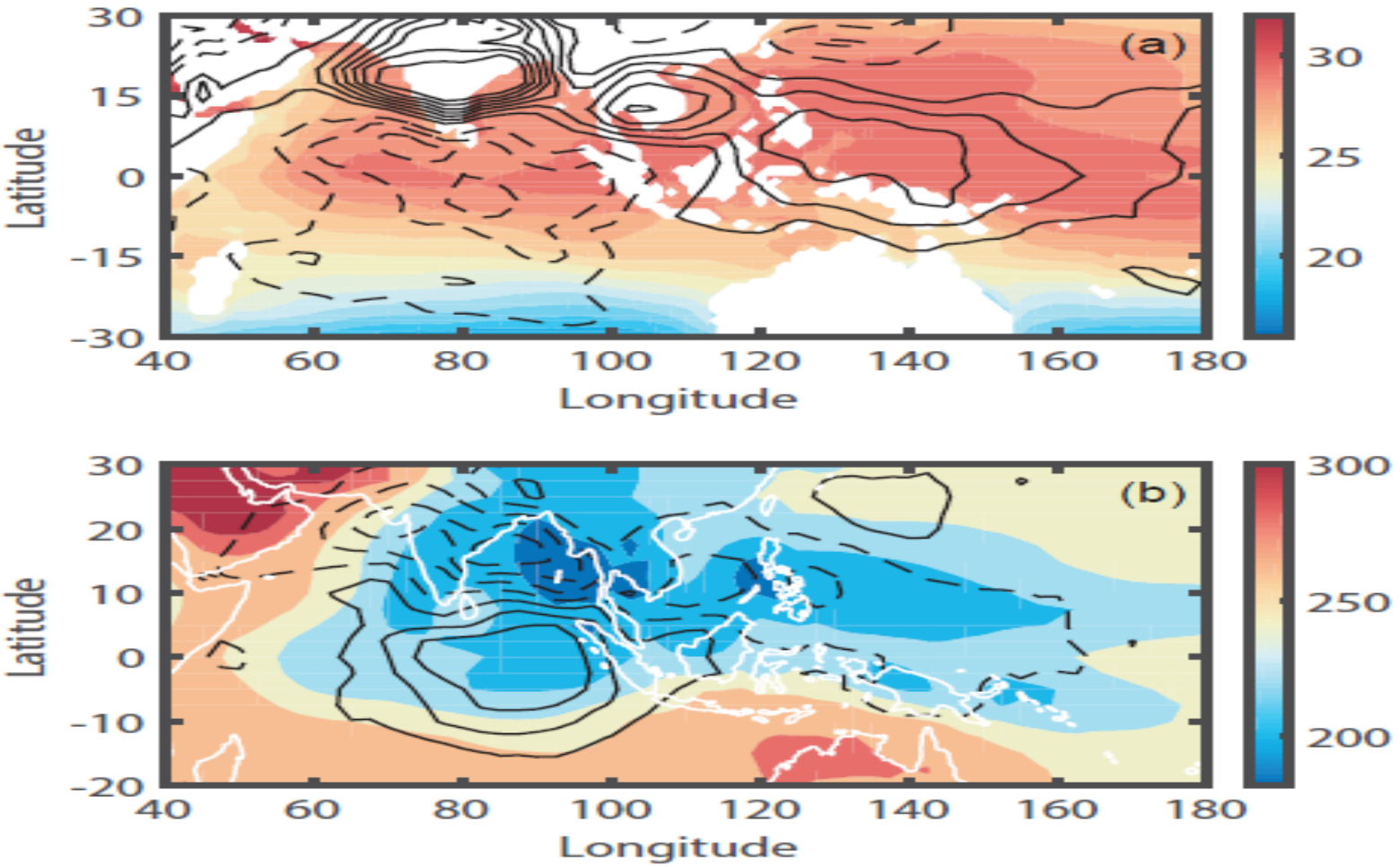

(a) Mean SST (unit: °C) during the ISM (colors) and differences in intraseasonal specific humidity at 500 hPa between the large-rainfall group and the small-rainfall group (contours). The contours start from ± 10^{-4} kg kg^{-1} and the interval is 10^{-4} kg kg^{-1}. (b) Mean OLR (colors; unit: W m^{-2}) during the ISM and differences in the intraseasonal OLR anomalies between the large-rainfall group and the small-rainfall group (contours). The contours start from ± 5 W m^{-2} and the interval is 10W m^{-1}. Solid (dashed) contours denote positive (negative) anomalies. All differences shown with the contours are statistically significant at a 95% confidence level.

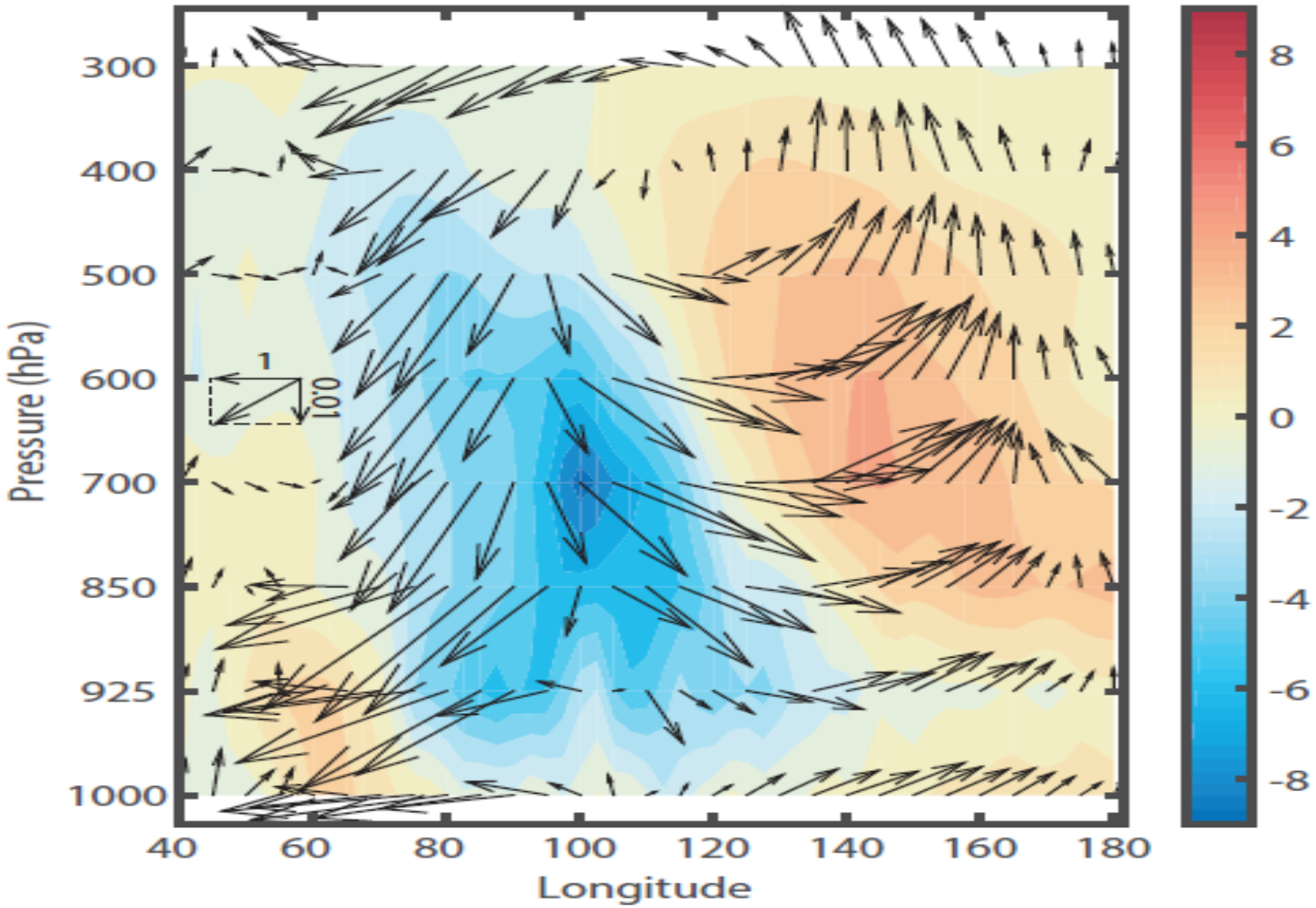

Differences of specific humidity (colors; unit: 10^{-4} kg kg^{-1}) and zonal momentum (ρu) and vertical momentum ($\rho\omega$; ω is the vertical pressure velocity). Units for zonal momentum are kg m^{-2} s^{-1} and for vertical momentum are kg Pa m^{-3} s^{-1}.

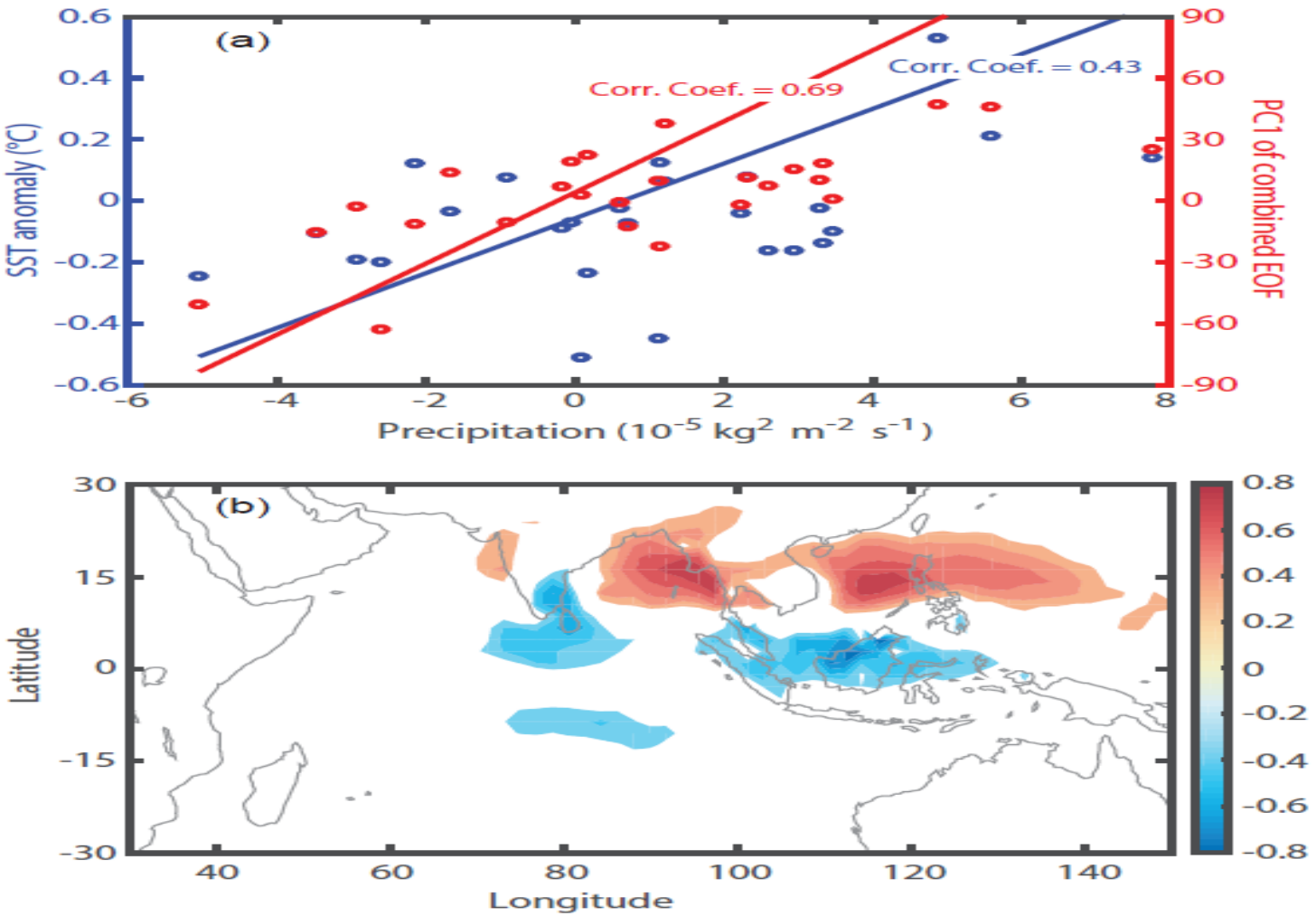

(a) The scatter plot of the intraseasonal SST anomalies (averaged over 5°N to 5°S; 80°E to 90°E) and the intraseasonal precipitation anomalies (averaged over 15°N to 24°N; 85°E to 95°E) for convection events over western Indian Ocean. All anomalies are averaged between 5 days and 10 days after the central day of the convection events, when the intraseasonal OLR anomalies over western Indian Ocean reach their minimum. (b) Correlation coefficients between PC1 of the CIO mode and intraseasonal precipitation during ISM, which are statistically significant at a 95% confidence level. The effective sample size is adjusted following Bretherton et al. (1999), so that the influence of band-pass filtering on the significance test of the correlation coefficient is removed.

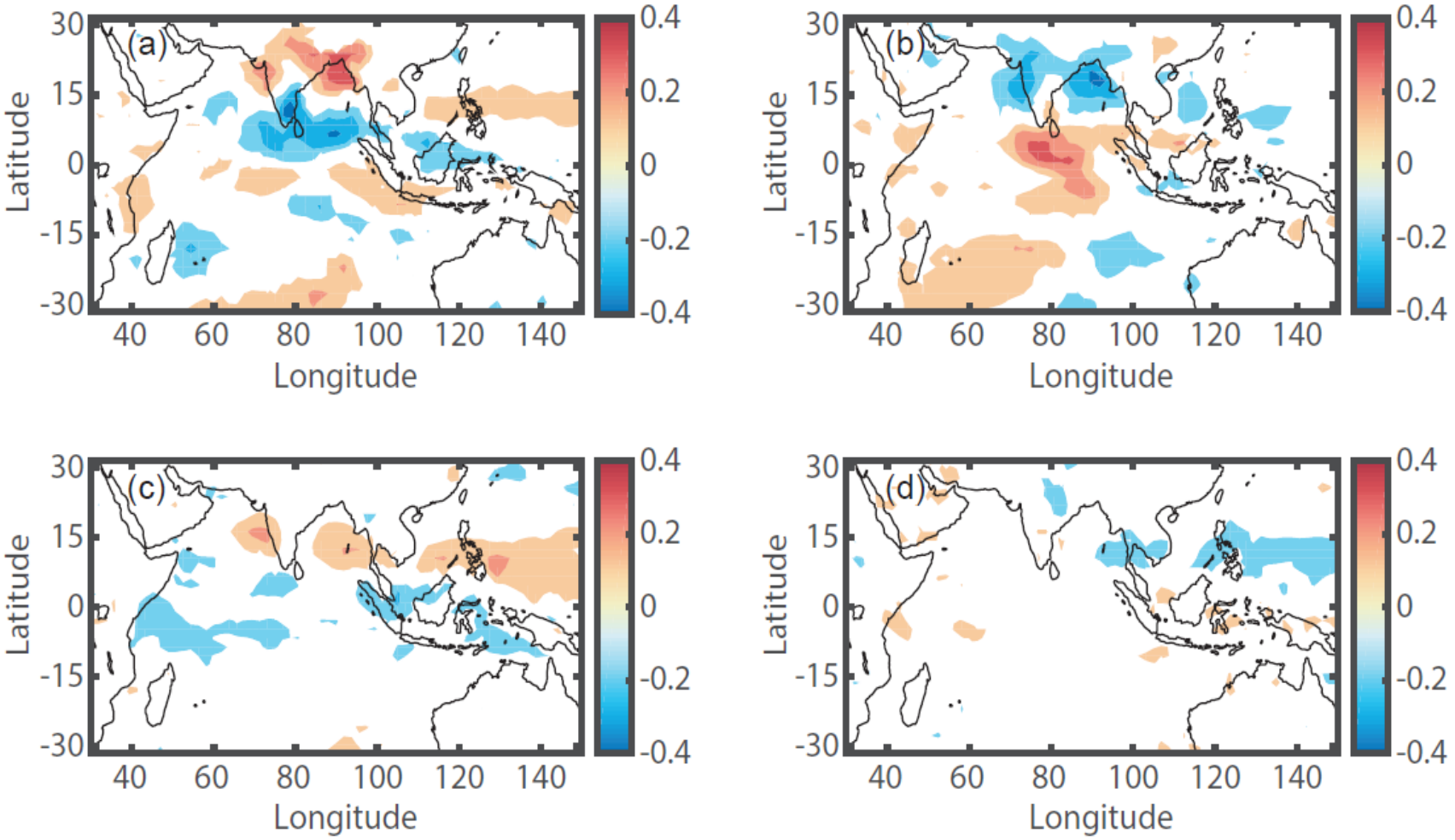

The correlation coefficients between intraseasonal precipitation and (a) intraseasonal SST anomalies averaged over the central Indian Ocean (from 5°N to 5°S; 80°E to 90°E), (b) DMI, (c) TNI, and (d) Niño 3.4 Index. In order to retain the ISVs in all indices, daily data are used for the calculations and no smoothing in time is applied. All correlation coefficients are smaller than 0.4, which are much less than the ones shown in Fig. 8b. All shown coefficients are statistically significant at a 95% confidence level.

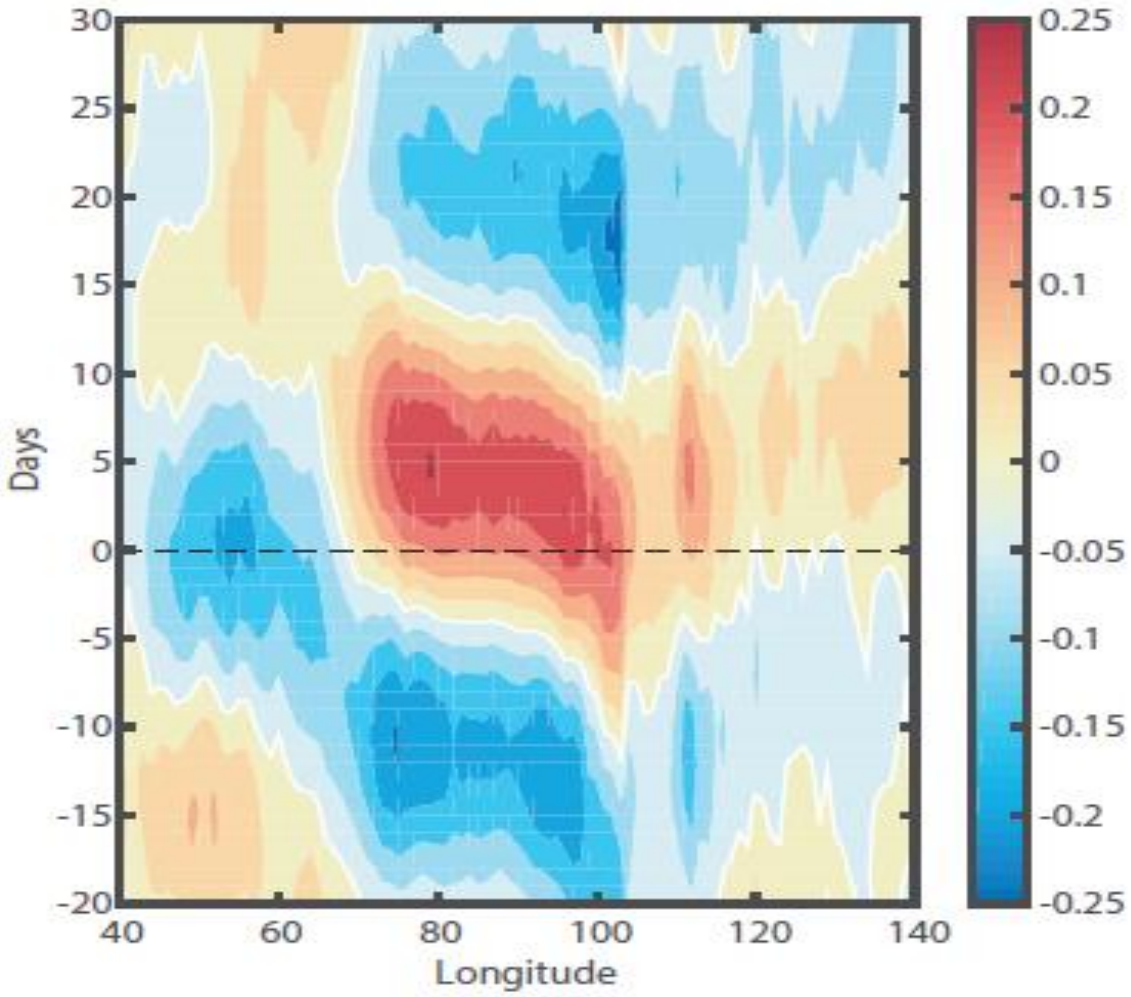

Hovmöller diagram of intraseasonal SST anomalies in the tropics for the positive CIO mode. Intraseasonal SST anomalies are averaged over 5°N to 5°S. Day 0 is the day with heavy precipitation, i.e., the day when the intraseasonal rainfall is larger than the mean plus the STD. There are 644 such days from 1982 to 2014. Negative (positive) days are before (after) Day 0. Unit are °C.

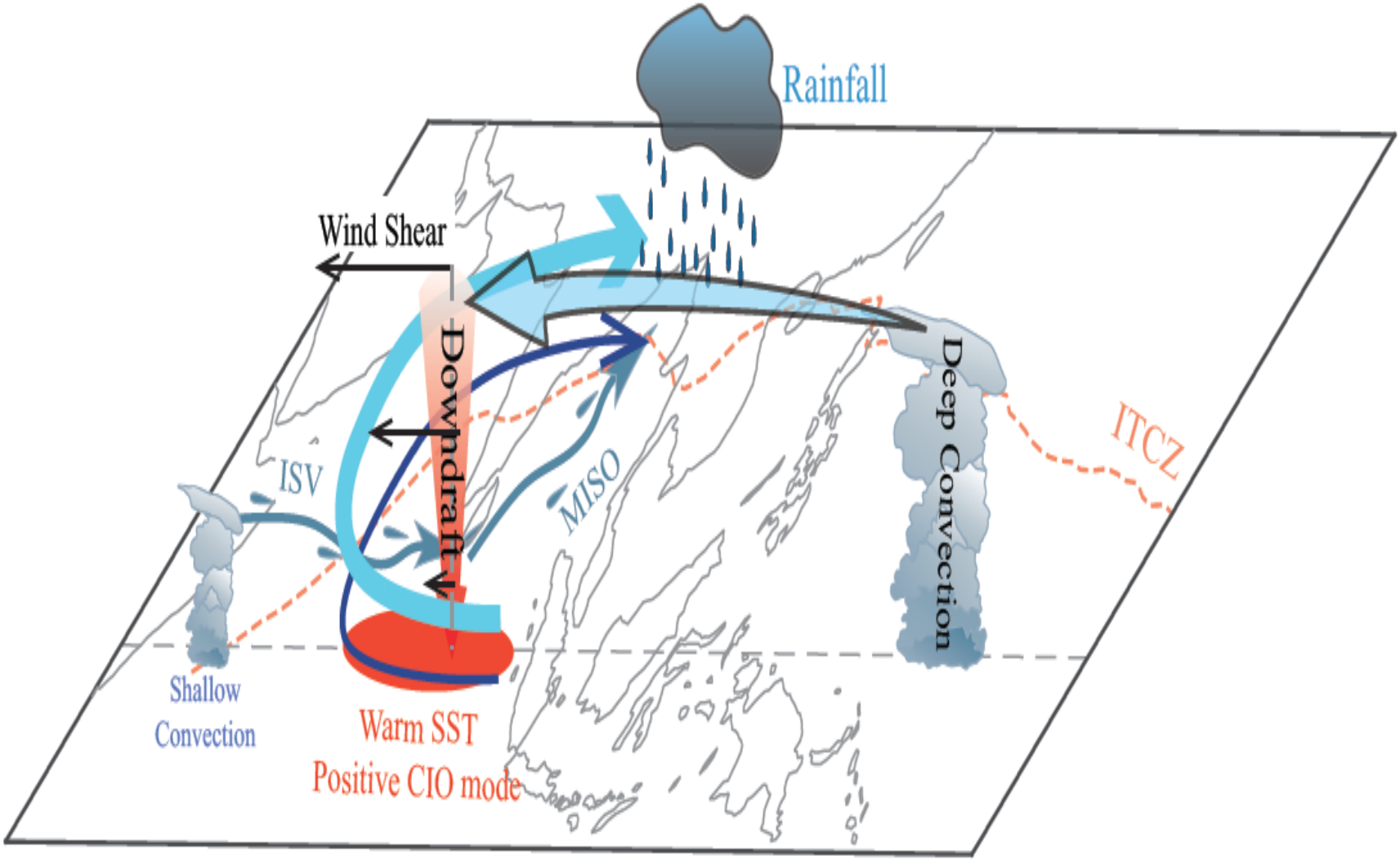

Sketch for the positive CIO mode and the associated atmospheric and oceanic anomalies.

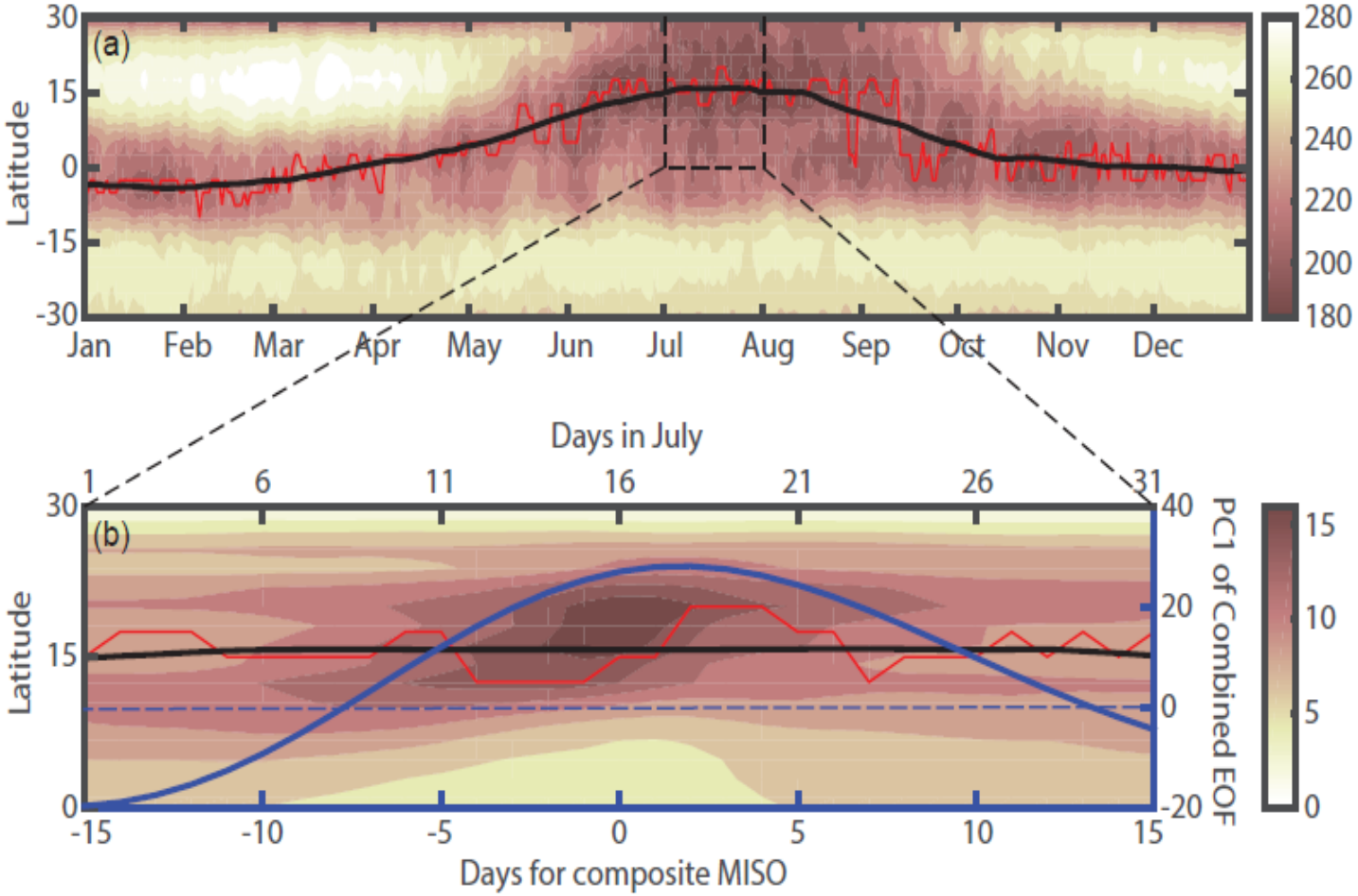

(a) The mean daily OLR averaged from 1982 to 2013 between 80°E and 100°E. The unit is W m^{-2}. The red line marks the latitude with the minimum OLR for each day. The black line denotes the ITCZ which is obtained with a 60-day running mean of the red line, so that the ISVs are largely removed. (b) The red line and the black line are the same as the ones in (a), but zoomed-in during July. The colors represent the northward-propagating MISO with the composite precipitation of the large-rainfall group. Units are 10^{-5} kg m^{-2} s^{-1}. Maximum precipitation over the northern BoB occurs on Day 0 (lower horizontal axis). Negative days are before Day 0 and positive days are after Day 0. The blue line (vertical axis on the right) is the principal component of the CIO mode (i.e., the first combined EOF mode).

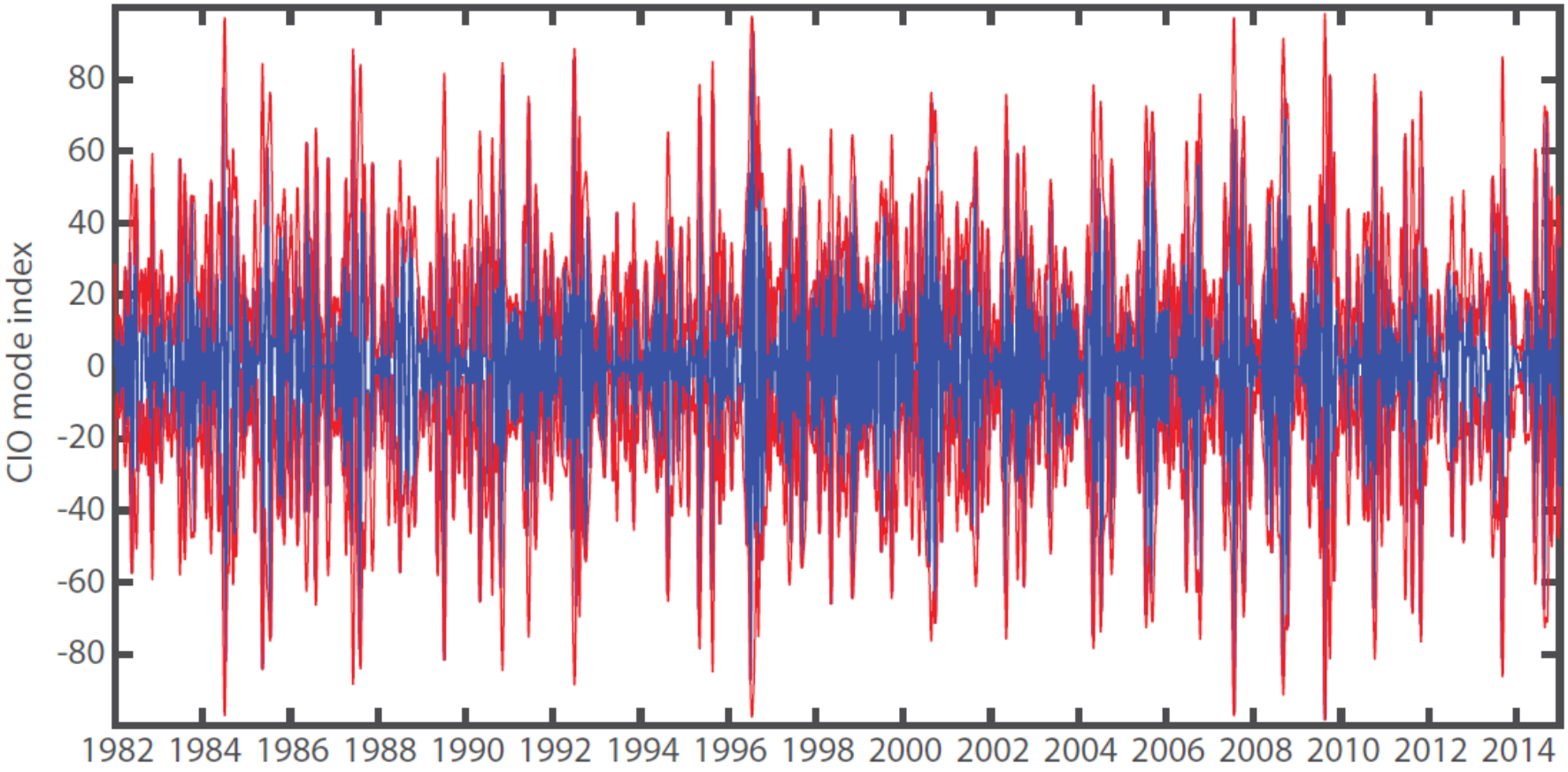

1 The CIO index (CI; blue line, i.e., the PC of the first combined EOF mode) and its envelop (EI; red line) obtained with the Hilbert transform.

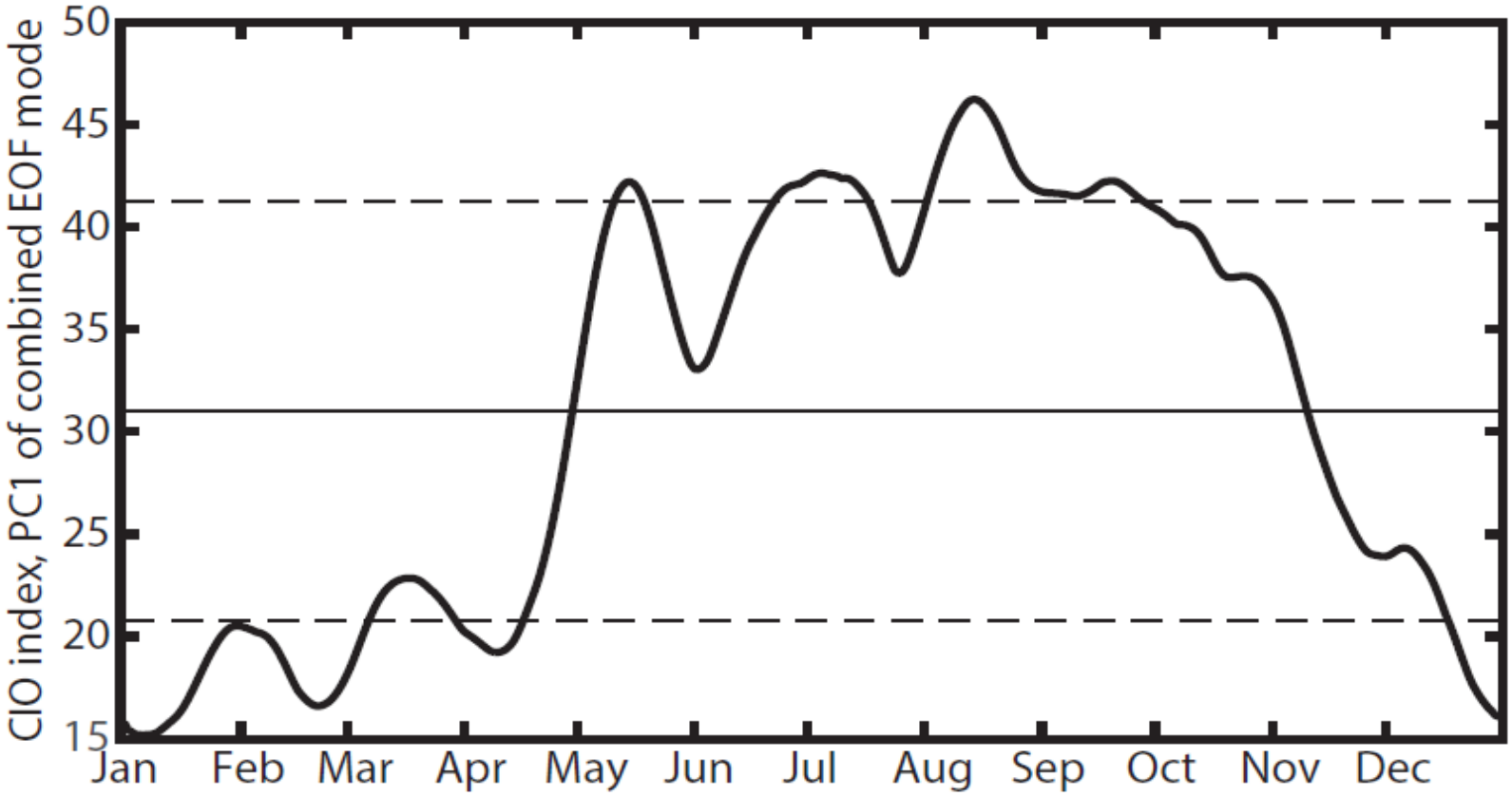

The climatological seasonal variation of EI (the envelope of CI, i.e., the CIO index), which is the mean daily index from 1982 to 20014. The solid line is the mean EI. The two dashed lines are the mean ± one STD of EI.

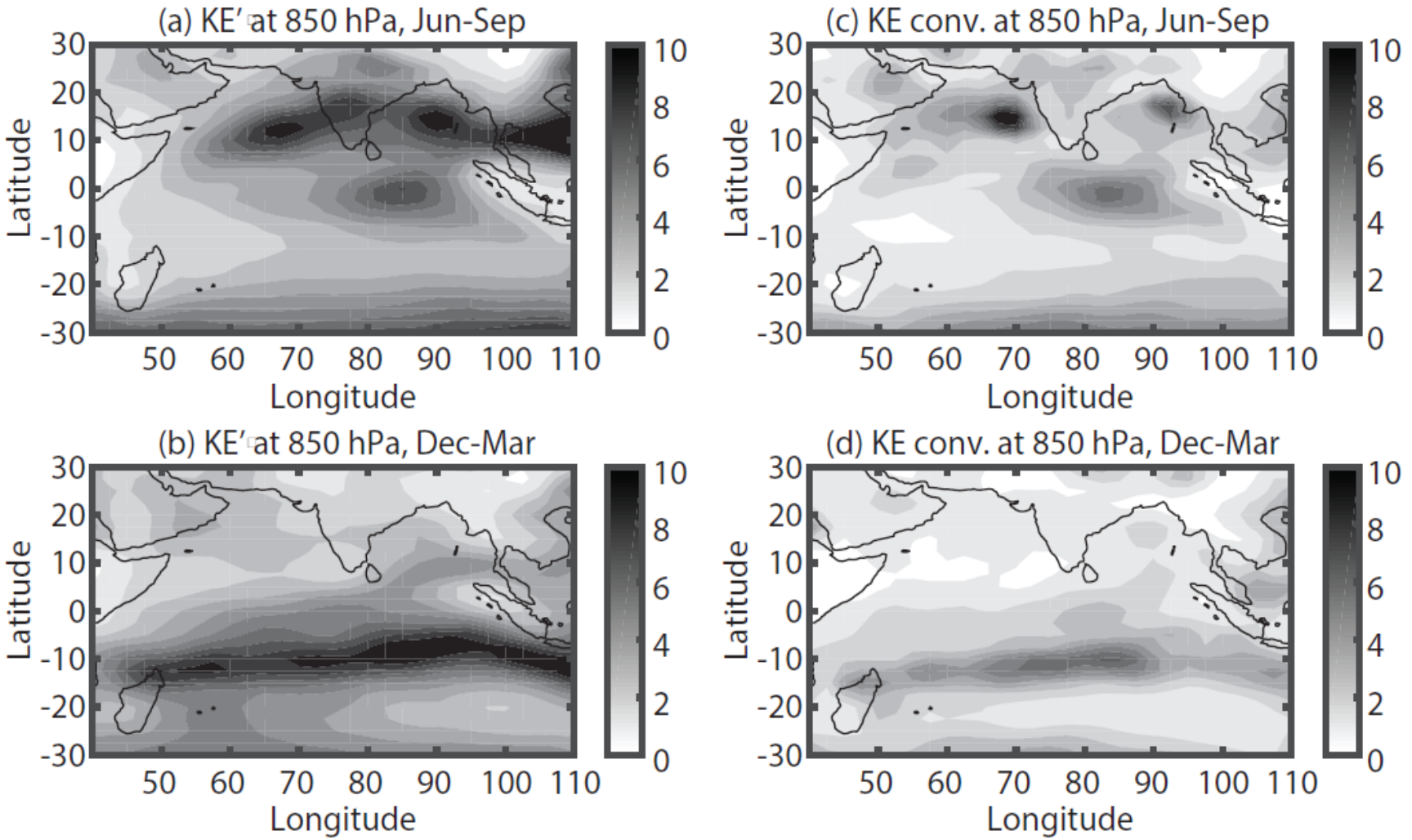

(a) Kinetic energy of ISVs (KE') at 850 hPa averaged over boreal summer from June to September. (b) Same as (a), but averaged over boreal winter from December to March. (c) and (d) Same as (a) and (b), but for $[KE' \times \overline{KE}]$. Units for KE' are J kg^{-1} and units for $[KE' \times \overline{KE}]$ are J day^{-1} kg^{-1}.

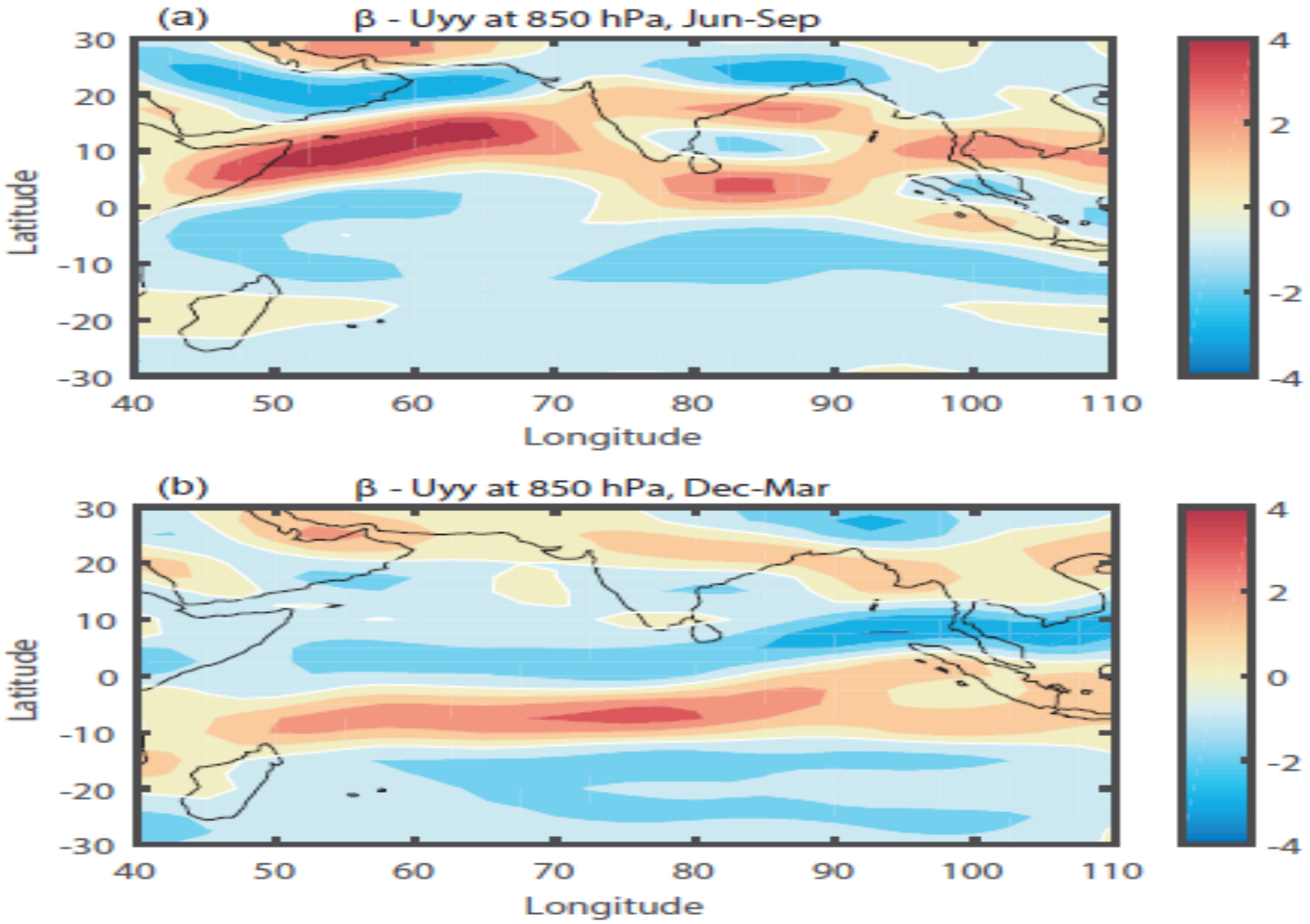

The meridional gradient of QGPV, i.e., $\frac{dq}{dy} = \beta - \frac{\partial^2 U}{\partial y^2}$, at 850 hPa for the ISM (from June to September; a) and boreal winter (from December to March; b). Units are 10^{-11} m^{-1} s^{-1}.

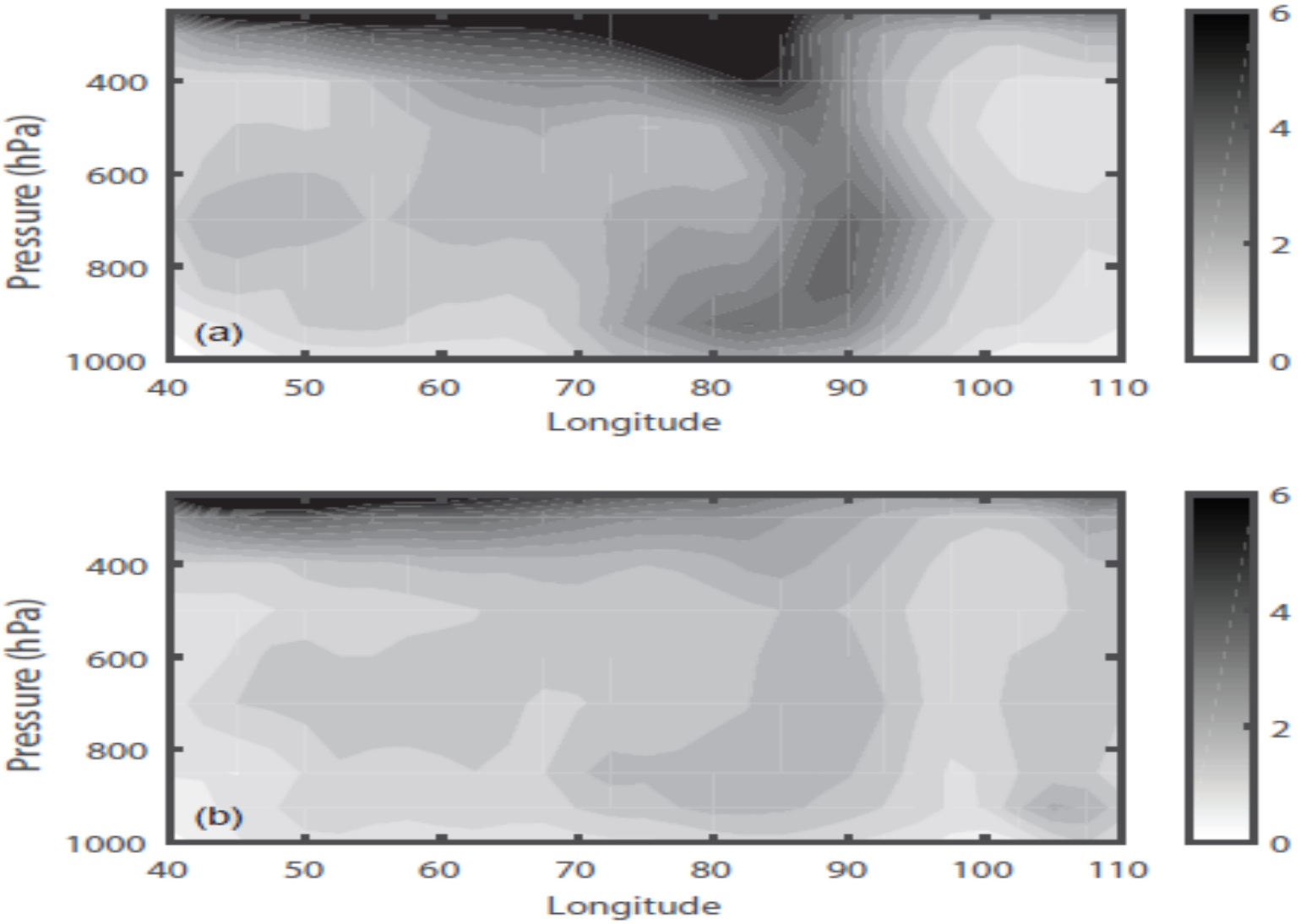

Vertical profile of the mean $[\mathrm{KE}' \times \overline{\mathrm{KE}}]$ averaged between 5°N and 5°S during ISM (a; from June to September), and during boreal winter (b; from December to March). Units are J Day^{-1} kg^{-1}.

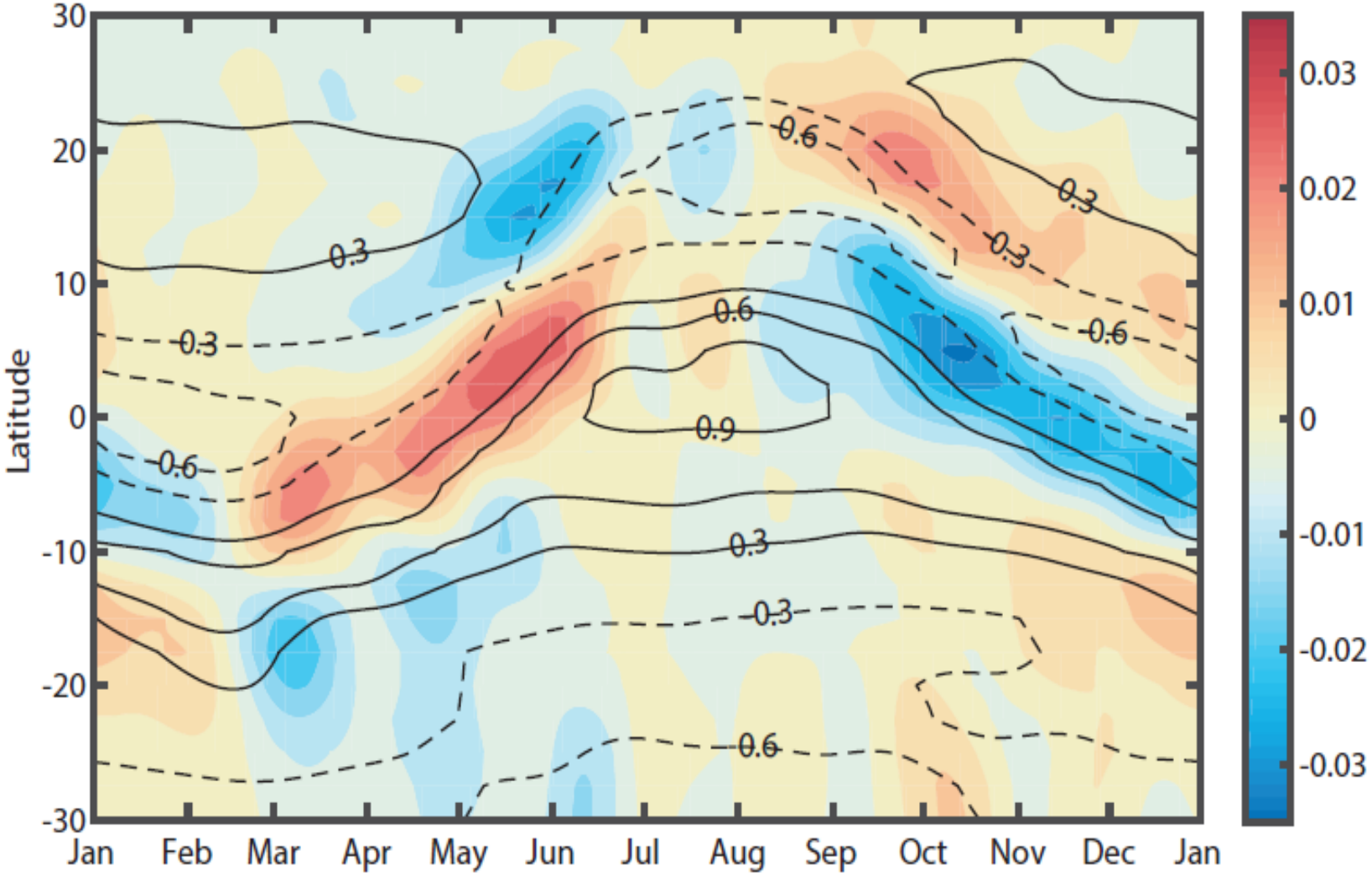

Daily mean $\frac{\partial \bar{u}}{\partial y}$ (contours, unit: day^{-1}) and $\frac{\partial}{\partial t}\left(\frac{\partial \bar{u}}{\partial y}\right)$ (colors, unit: day^{-2}) averaged from 1982 to 2014 over the Indian Ocean from 40°E to 120°E.

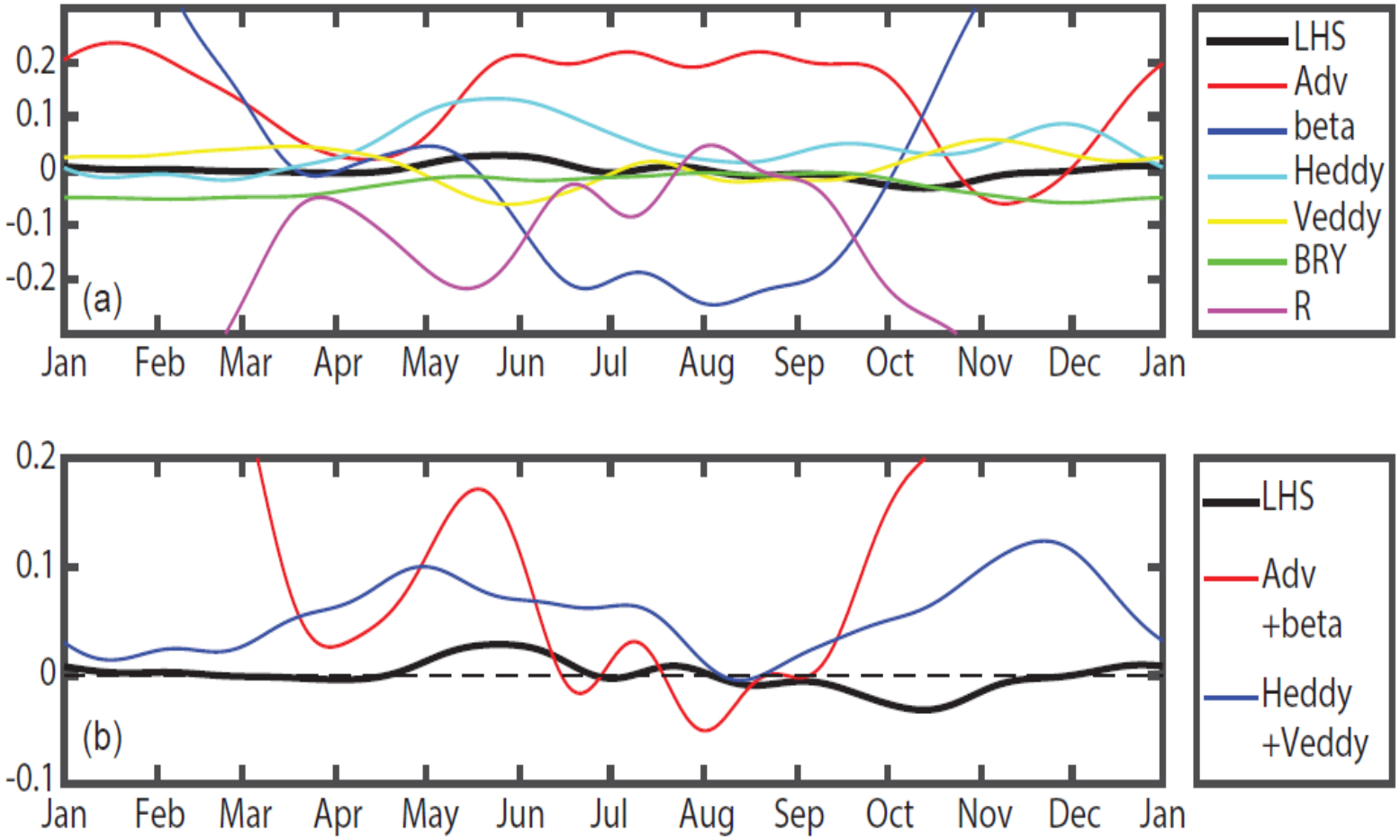

All terms in Eq. (4) along 5°N. (b) Three major components in Eq. (4). LHS denotes the $\frac{\partial}{\partial t}\left(\frac{\partial \bar{u}}{\partial y}\right)$ on the left-hand-side of Eq. (4), Adv is the advection term, beta is the β_{term}, and R is the residual term. The domain for the zonal mean is the Indian Ocean basin from 40°E to 120°E. Units are day^{-2}.

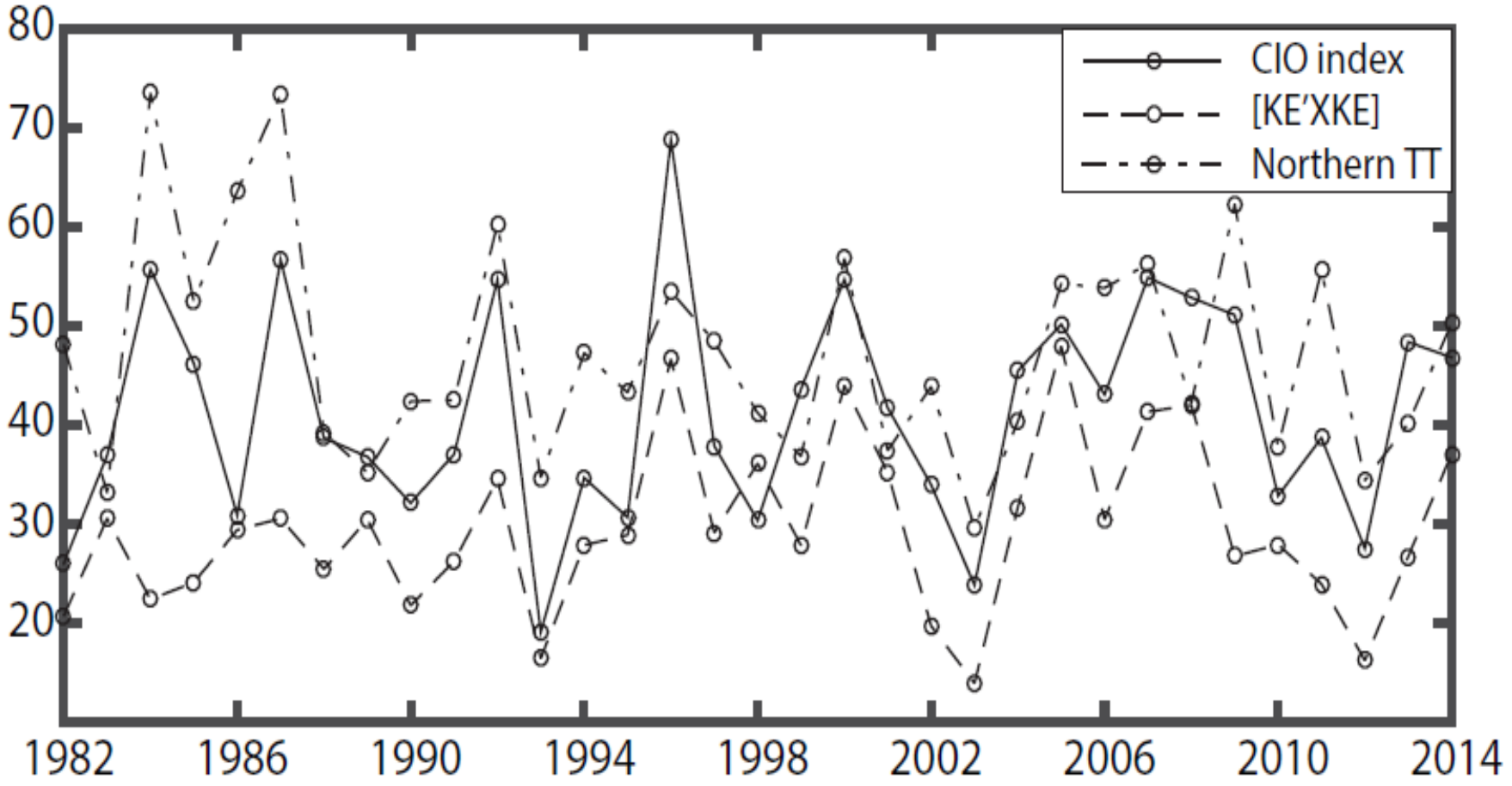

Solid line: EI averaged from June to September in each year. Dashed line: Mean $[\mathrm{KE}' \times \overline{\mathrm{KE}}]$ at 850 hPa, averaged over 75°E-85°, 5°N-15°N, and also averaged from June to September in each year. Dash-dot line: The envelop (obtained with the Hilbert transform) of intraseasonal TT index in the northern box (35°N–10°N, 30°E–110°E), averaged from June to September in each year. Units for the mean $[\mathrm{KE}' \times \overline{\mathrm{KE}}]$ are 0.1 J day^{-1} kg^{-1} and units for the TT index are 0.01 °C.

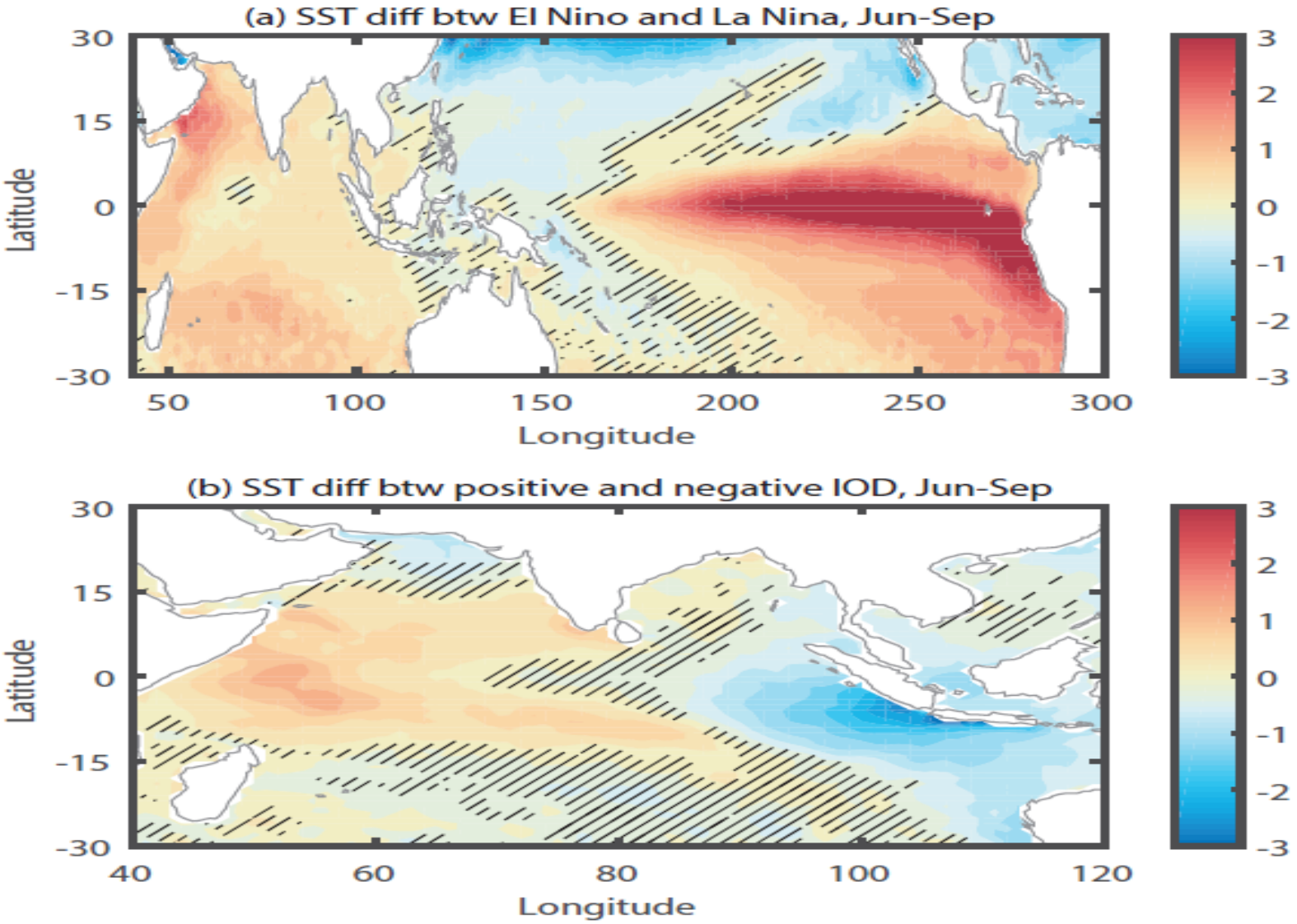

SST differences during ISM (from June to September) between El Niño and La Niña (a), and between positive and negative IODZM phases (b). Units are °C. The differences in the hatched regions are not significant at a 95% confidence level.

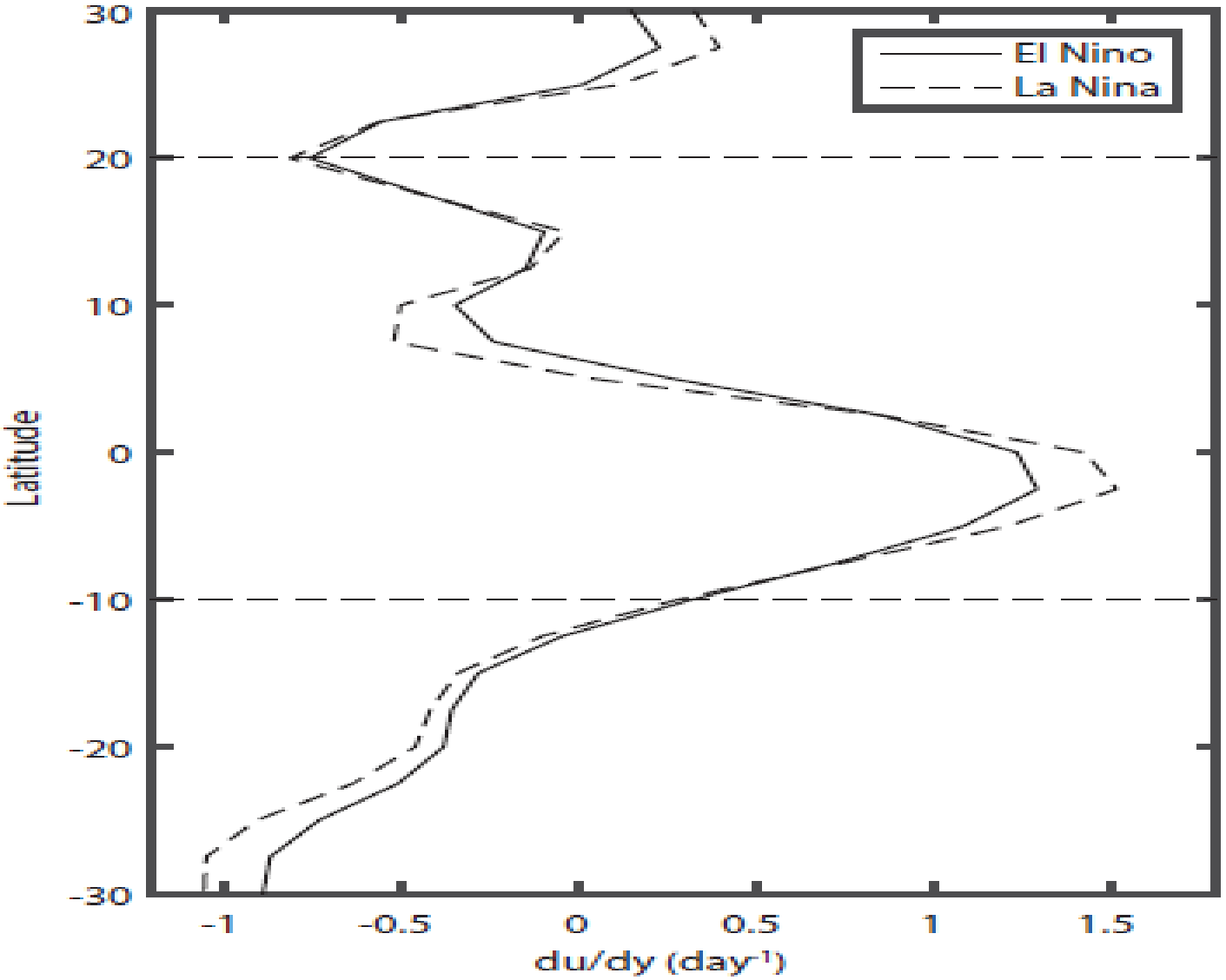

Meridional gradient of zonal wind (∂u/∂y) at 850 hPa, averaged between 80°E and 90°E, during El Niño and La Niña.

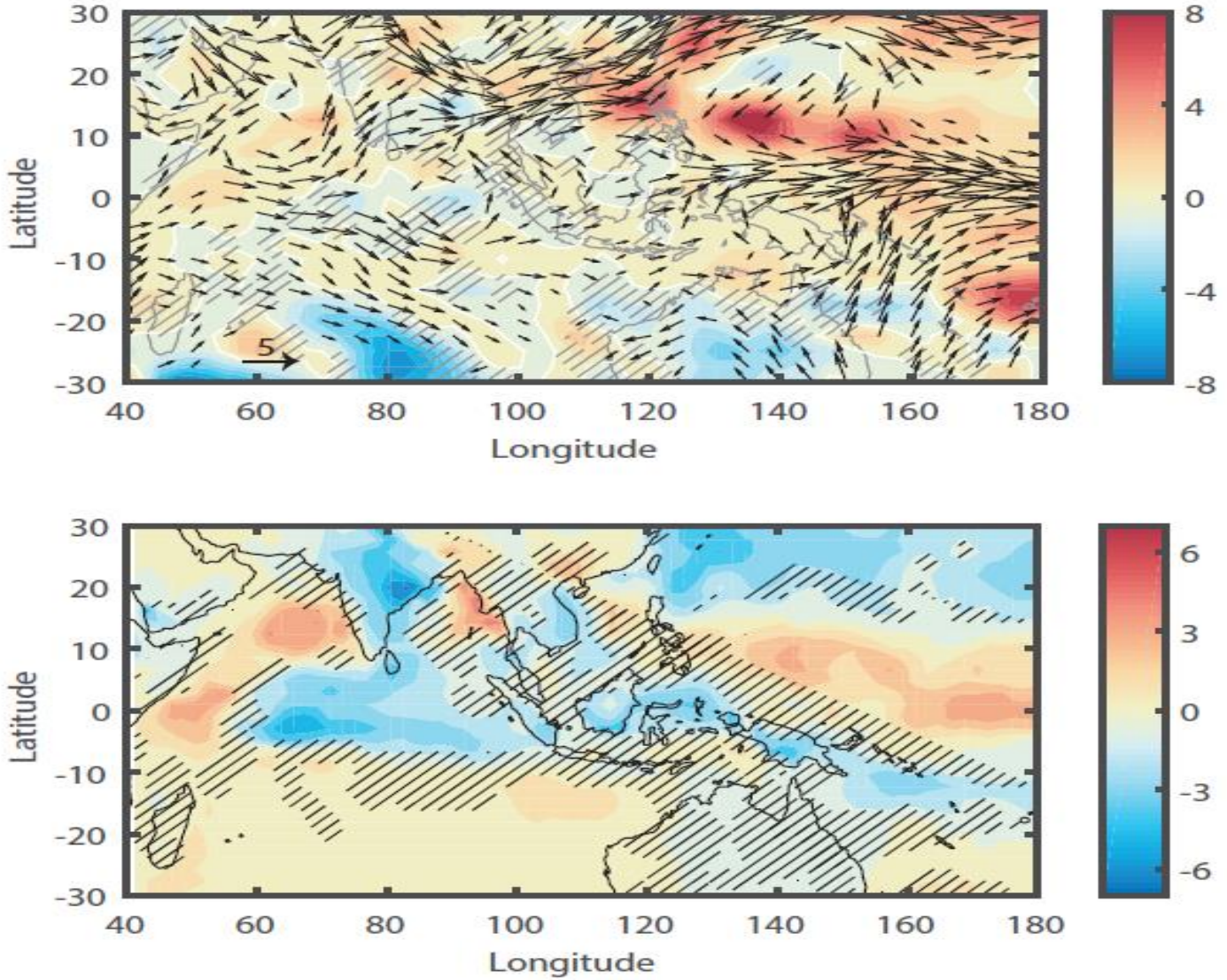

(a) Difference in $[\mathrm{KE}' \times \overline{\mathrm{KE}}]$ at 850 hPa (colors) and in winds at 850 hPa (vectors) between El Niño and La Niña during ISM (from June to September). Units are J Day^{-1} kg^{-1}. (b) Difference in precipitation between El Niño and La Niña. Units are kg m^{-2} day^{-1}. The differences in the hatched regions are not significant at a 95% confidence level.

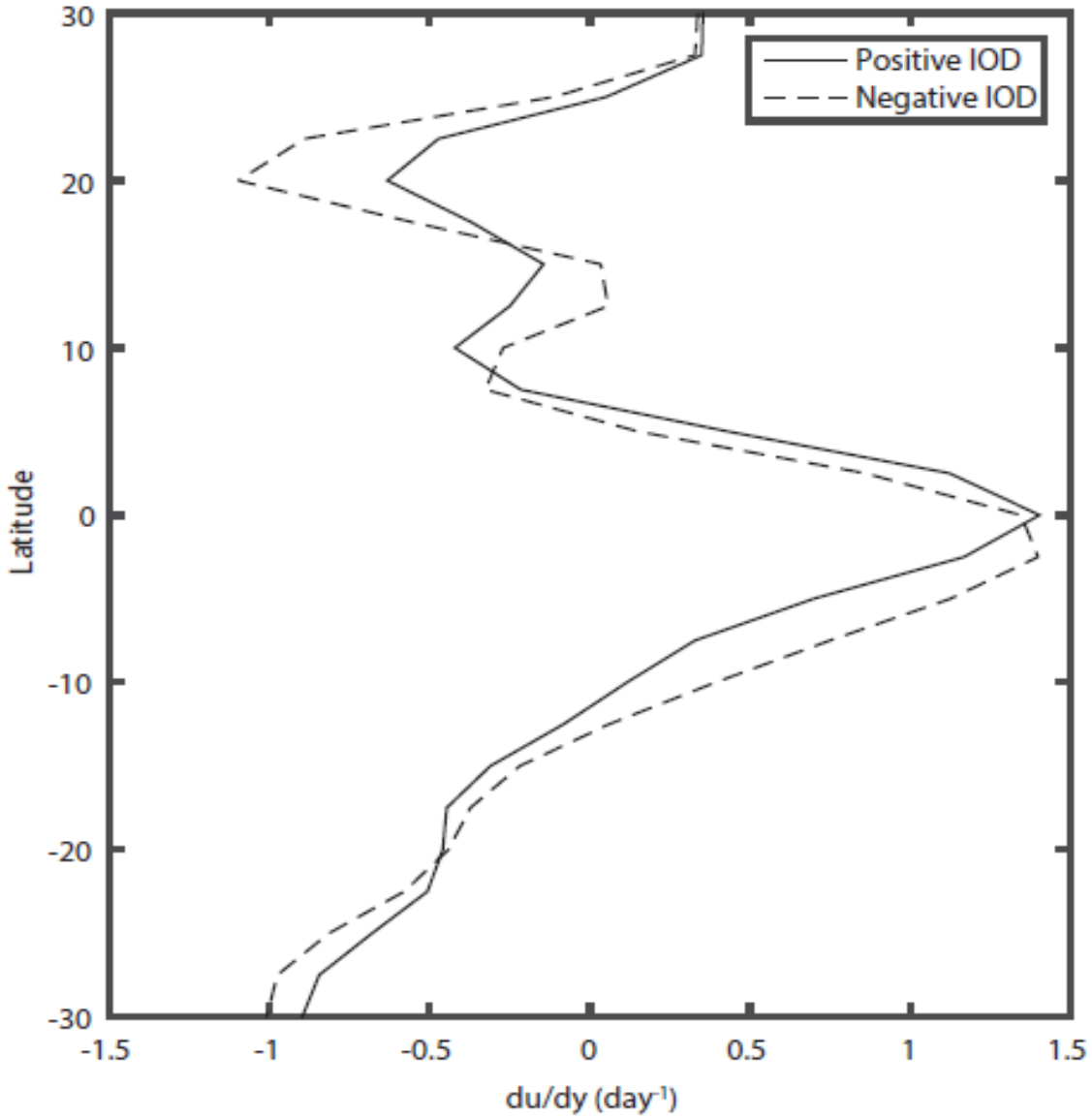

Meridional gradient of zonal wind (∂u/∂y) at 850 hPa, averaged between 80°E and 90°E, during positive and negative IODZM phases.

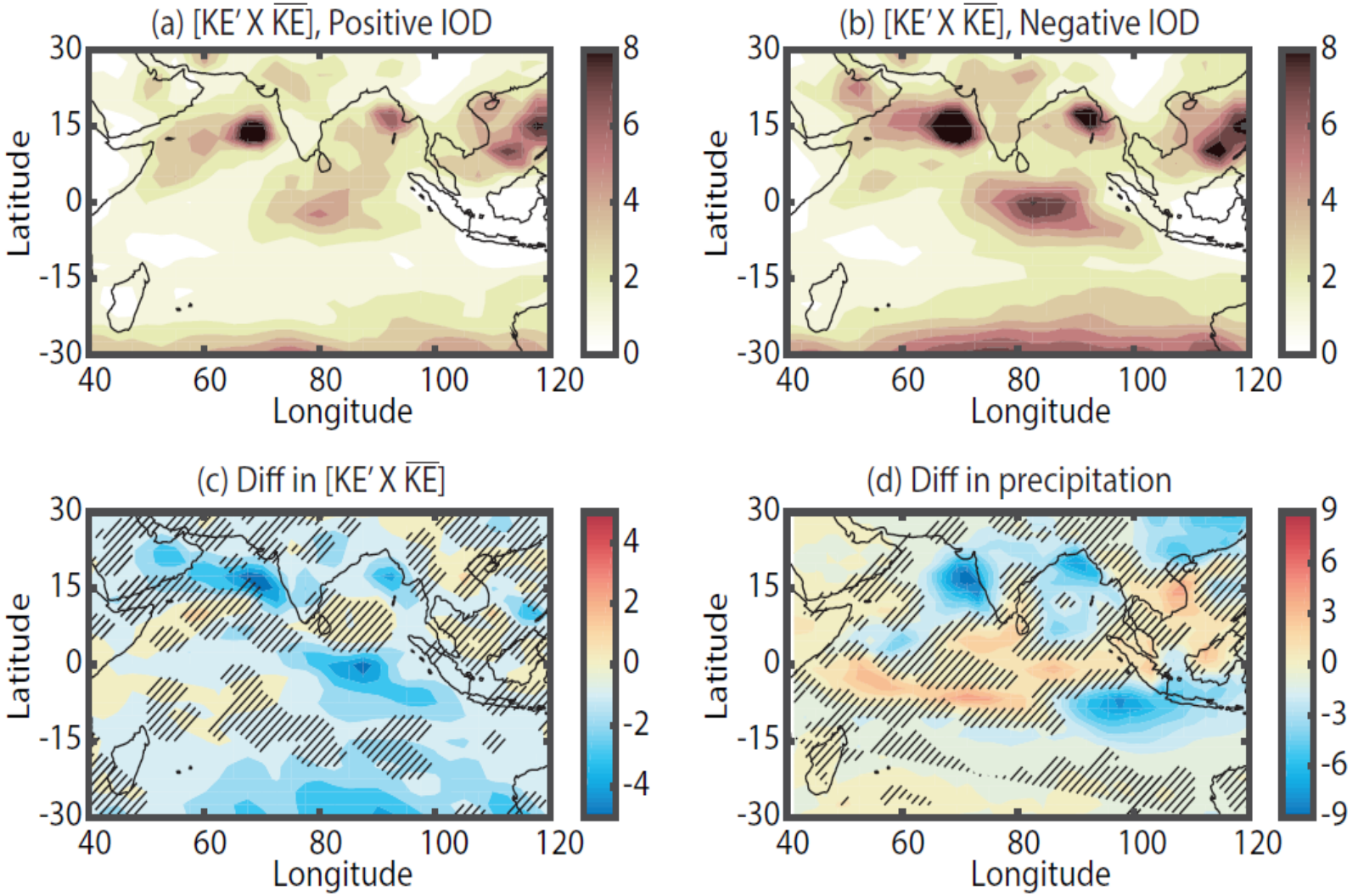

Mean $[\mathrm{KE}' \times \overline{\mathrm{KE}}]$ at 850 hPa during positive IODZM (a) and negative IODZM (b), and their differences (c). Units are J Day^{-1} kg^{-1}. (d) Differences in precipitation between positive and negative IODZM phases. Units are kg m^{-2} day^{-1}. The differences in the hatched regions are not significant at a 95% confidence level.

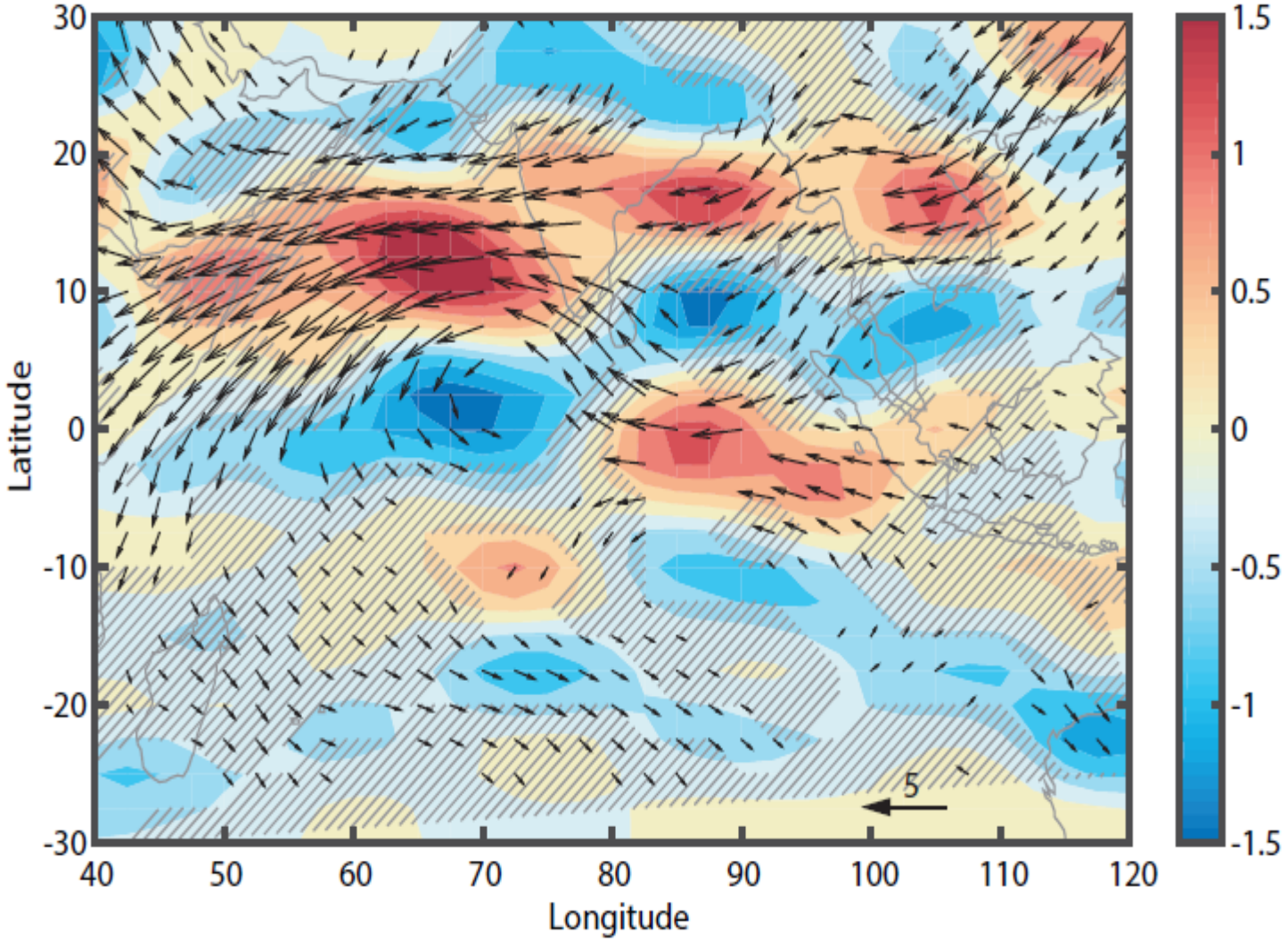

Difference in winds (δu) at 850 hPa (vectors) and in $\partial^2(\delta u)/dy^2$ (units: 10^{-11} m^{-1} s^{-1}) between the positive and the negative IODZM phases. The differences in the hatched regions are not significant at a 95% confidence level.

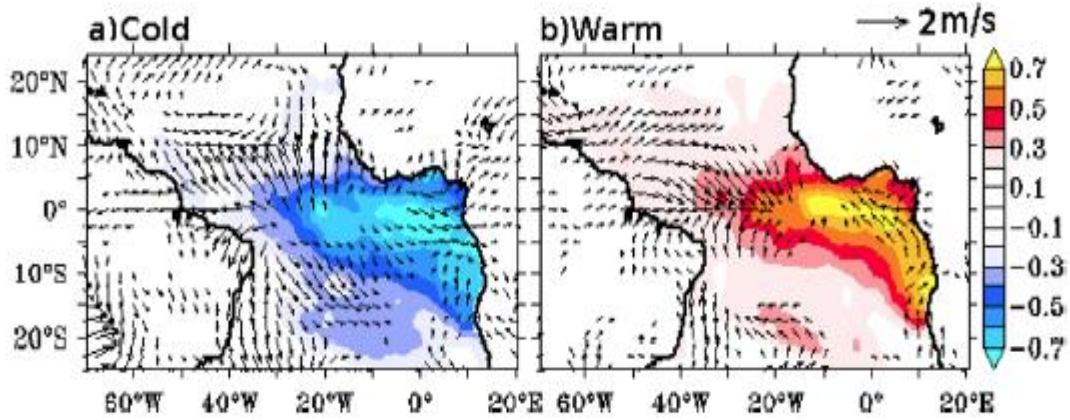

Figure 1. Seasonal composite (June–July–August) of SST anomalies overlaid by surface wind vector anomalies for the (a) cold and (b) warm AZM years.

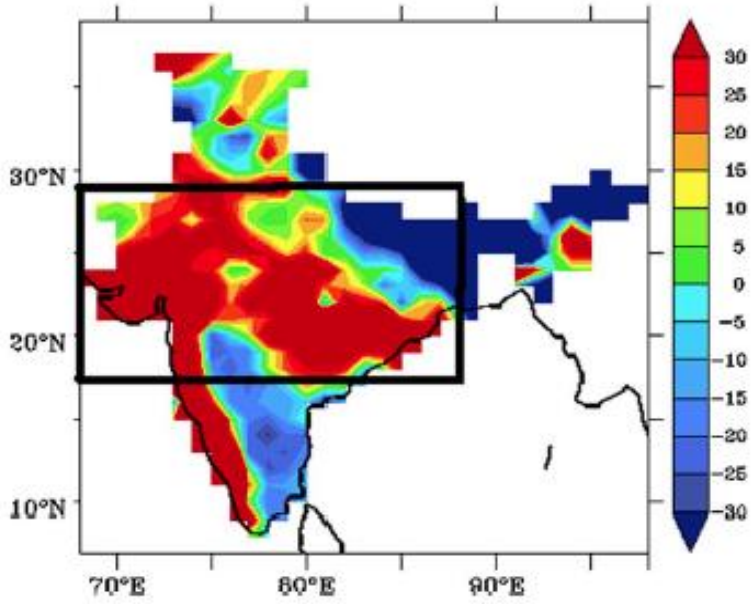

Figure 2. The difference (cold-warm) in seasonal (June–August) composite of monsoon rainfall (mm month^{-1}) during AZM years. The black box indicates the approximate area of core monsoon region (18°N–28°N and 65°E–88°E) defined by *Rajeevan et al.* [2010].

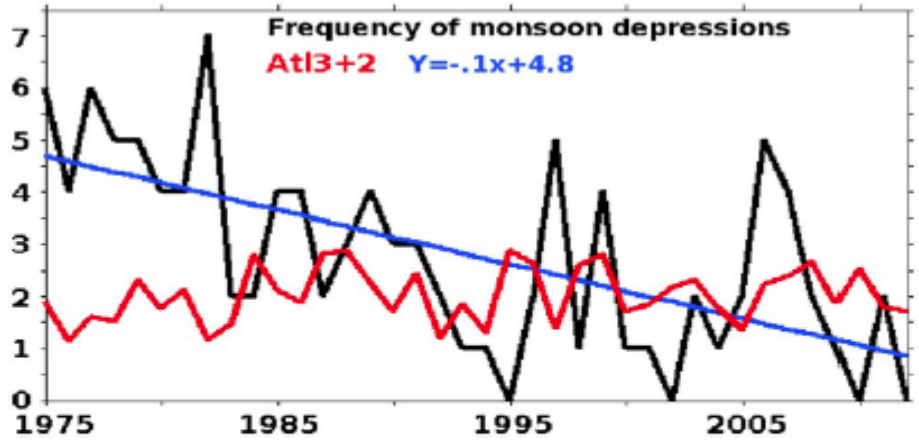

Figure 3. Time series of (black line) frequency of monsoon depressions in the Bay of Bengal during June–August and (red line) Atl3 index averaged during June–August ("2" is added to show it along with others) for the period 1975–2012. The green line indicates the least squares linear fit for the frequency of monsoon depressions with slope −0.1 and intercept 4.8.

All interannual variability studies face sampling limitations. Especially when it comes to ENSO

Table 1. Total Number of Monsoon Depressions Formed Under the Cold and Warm Years for All the AZM Years, AZM Years Without ENSO Years, All the ENSO Years and ENSO Years Without AZM Years During the Study Period of 1975–2012[a]

	AZM Cold (Pure AZM Cold)	AZM Warm (Pure AZM Warm)	La Niña (Pure La Niña)	El Niño (Pure El Niño)	Normal Years
Number of years	8 (6)	9 (4)	7 (3)	7 (4)	14
Total depressions	26 (15)	12 (2)	17 (10)	18 (5)	43
Depressions per season	**3.3 (2.5)**	**1.3 (0.5)**	2.5 (3.3)	2.6 (1.25)	3.1
Average life of a depression in days	4 (4.4)	3 (4)	2.9 (3.3)	3.1 (3.2)	2.9

[a]The corresponding means of cold and warm events whose difference crosses 95% confidence level are marked in bold (others are not significant even at 90%).

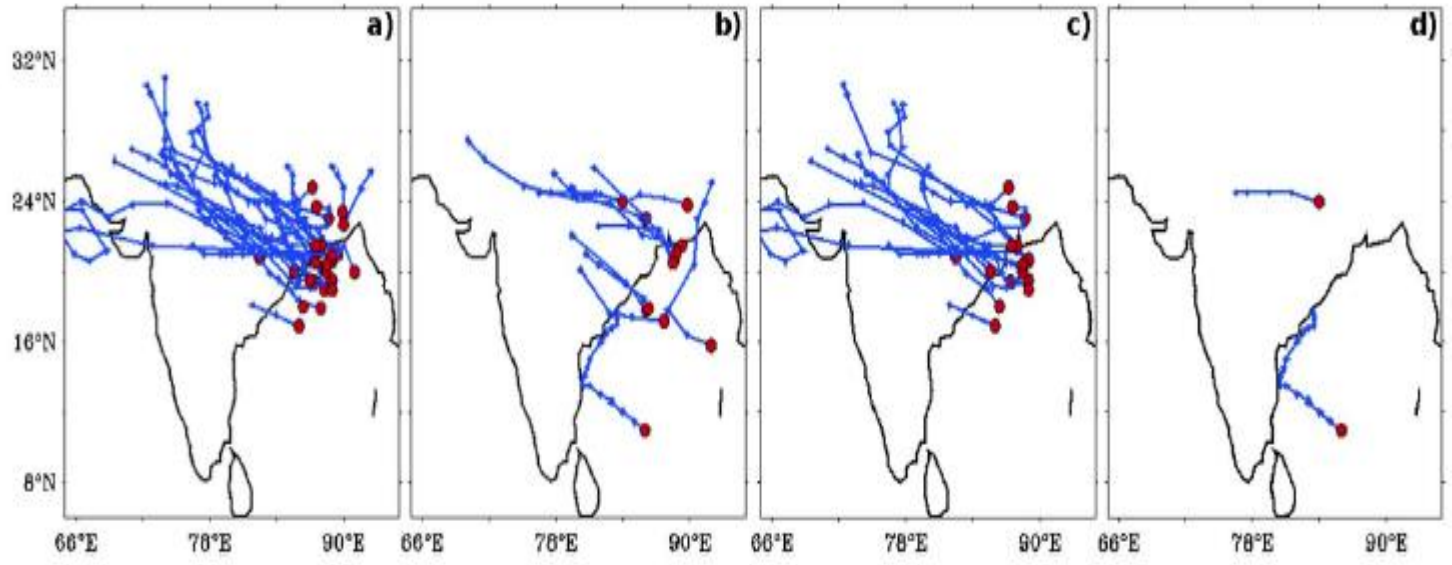

Figure 4. The genesis locations (red circle) and tracks of monsoon depressions (blue line) during (a and c) cold and (b and d) warm phases of AZM. Figures 4a and 4b represent all the corresponding AZM years and Figures 4c and 4d represent all the corresponding AZM years without ENSO years.

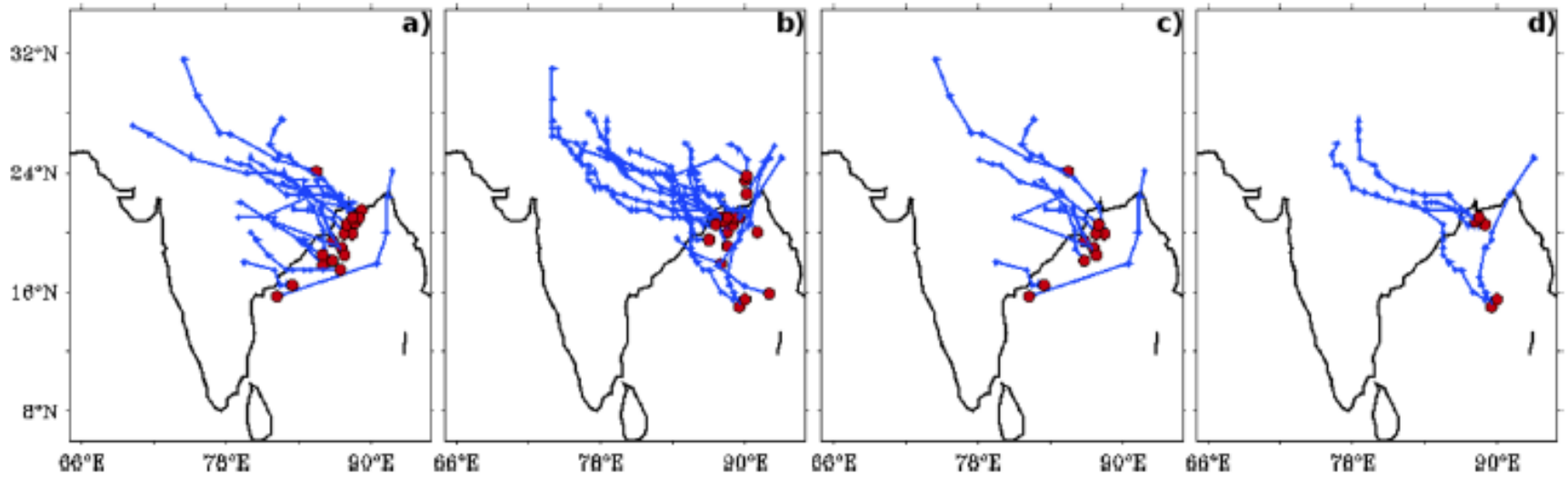

Figure 5. The genesis locations (red circle) and tracks of monsoon depressions (blue line) during (a and c) cold and (b and d) warm phases of ENSO. Figures 5a and 5b represent all the corresponding ENSO years, and Figures 5c and 5d represent all the corresponding ENSO years without AZM years.

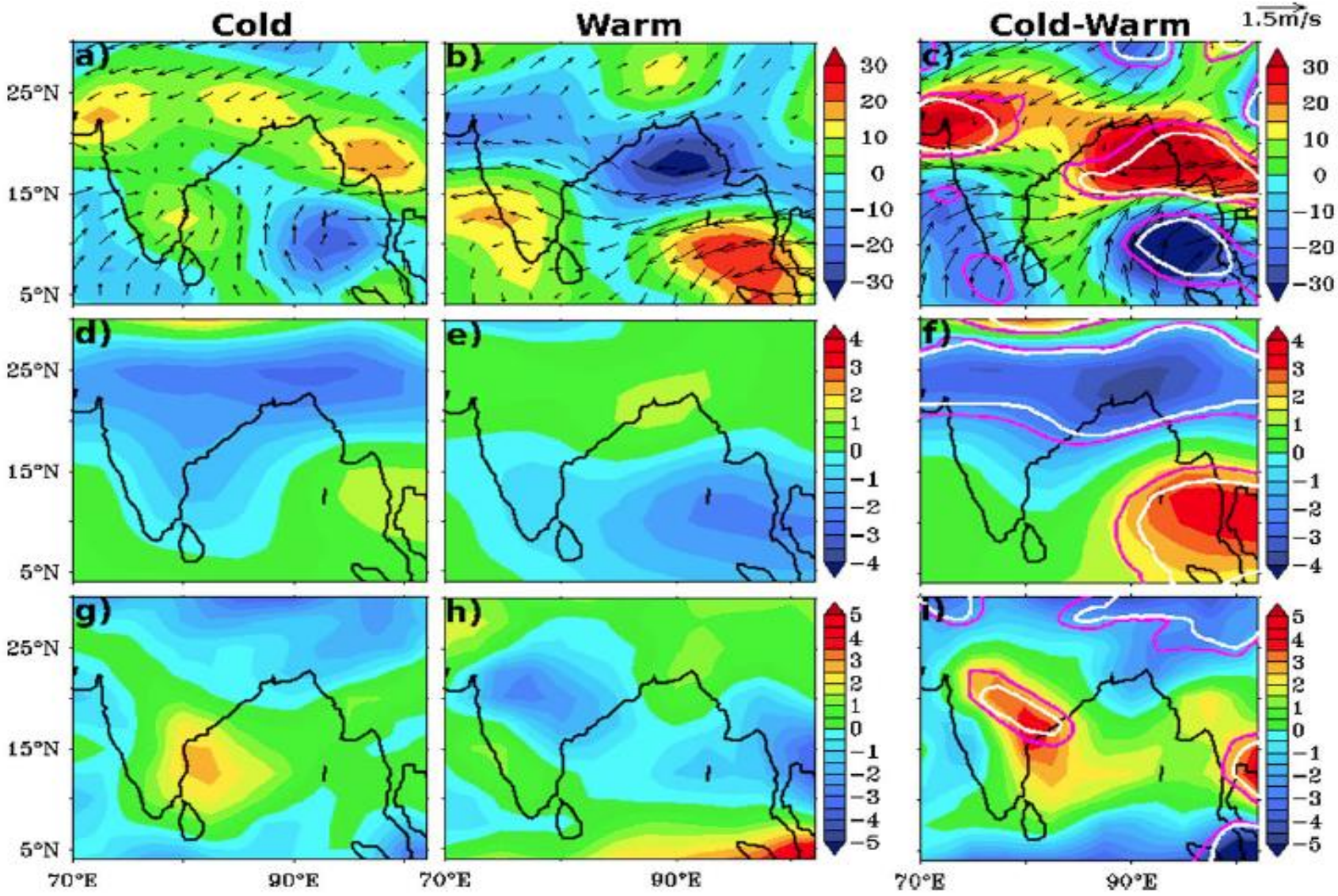

Figure 6. Composites of seasonal average (June–August) of (a and b) low-level (850 hPa) vorticity anomaly (10^{-7} s^{-1}) overlaid by the corresponding wind vector anomalies, (d and e) vertical wind shear anomaly ($m\,s^{-1}$), and (g and h) midtroposphere (600 hPa) humidity anomaly (%) during the cold and warm phase of AZM years. Cold minus warm composite of (c) low-level (850 hPa) vorticity anomaly (10^{-6} s^{-1}) overlaid by the corresponding composite of wind vector anomalies, (f) vertical wind shear anomaly (ms^{-1}), and (i) midtroposphere (600–hPa) humidity anomaly (%). In Figures 6c, 6f, and 6i, the pink and white contours indicate 80% and 90% confidence levels as per two-tailed Student's *t* test, respectively.

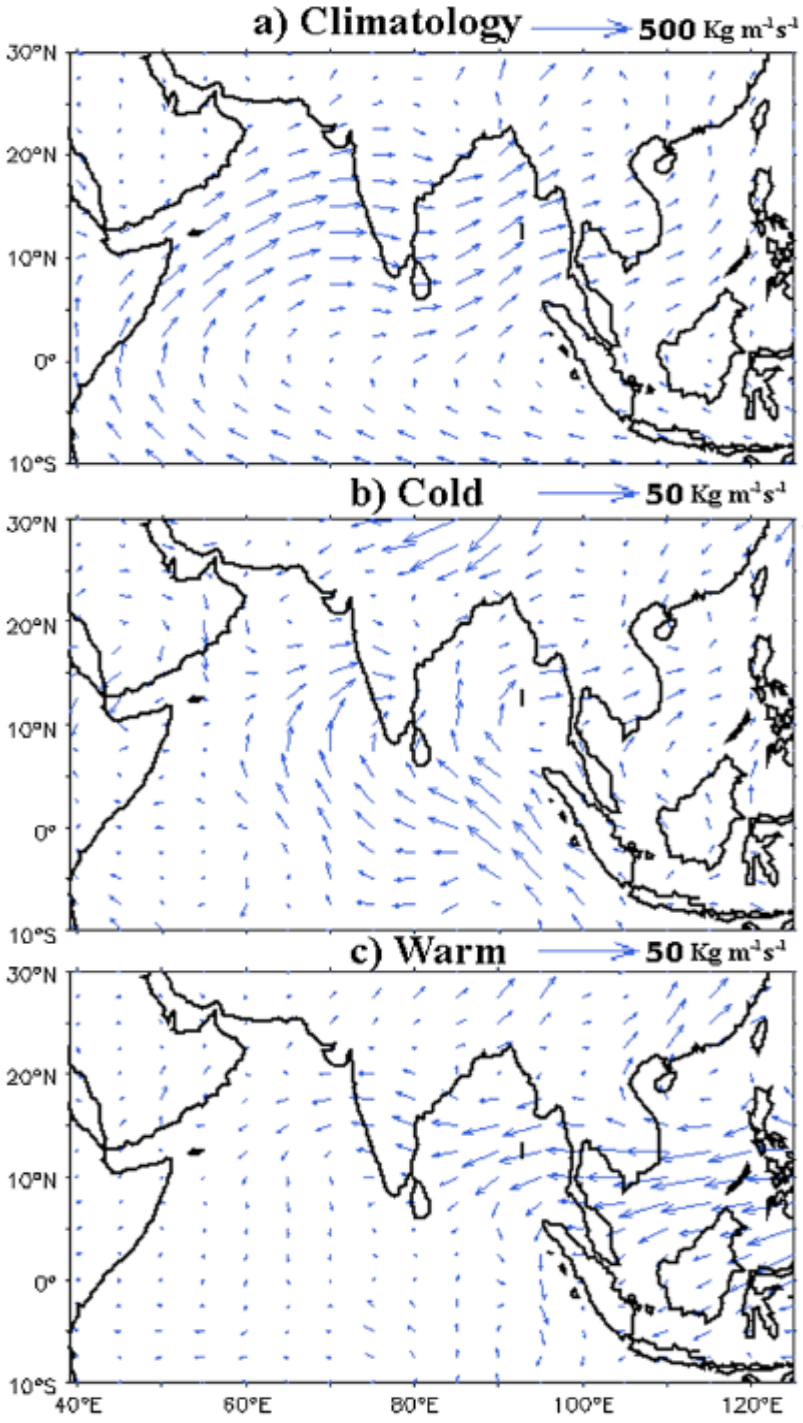

Figure 8. Seasonal average of integrated moisture transport's (Kg m^{-1} s^{-1}) (a) climatology and composite of its anomaly during (b) cold and (c) warm phase of AZM.

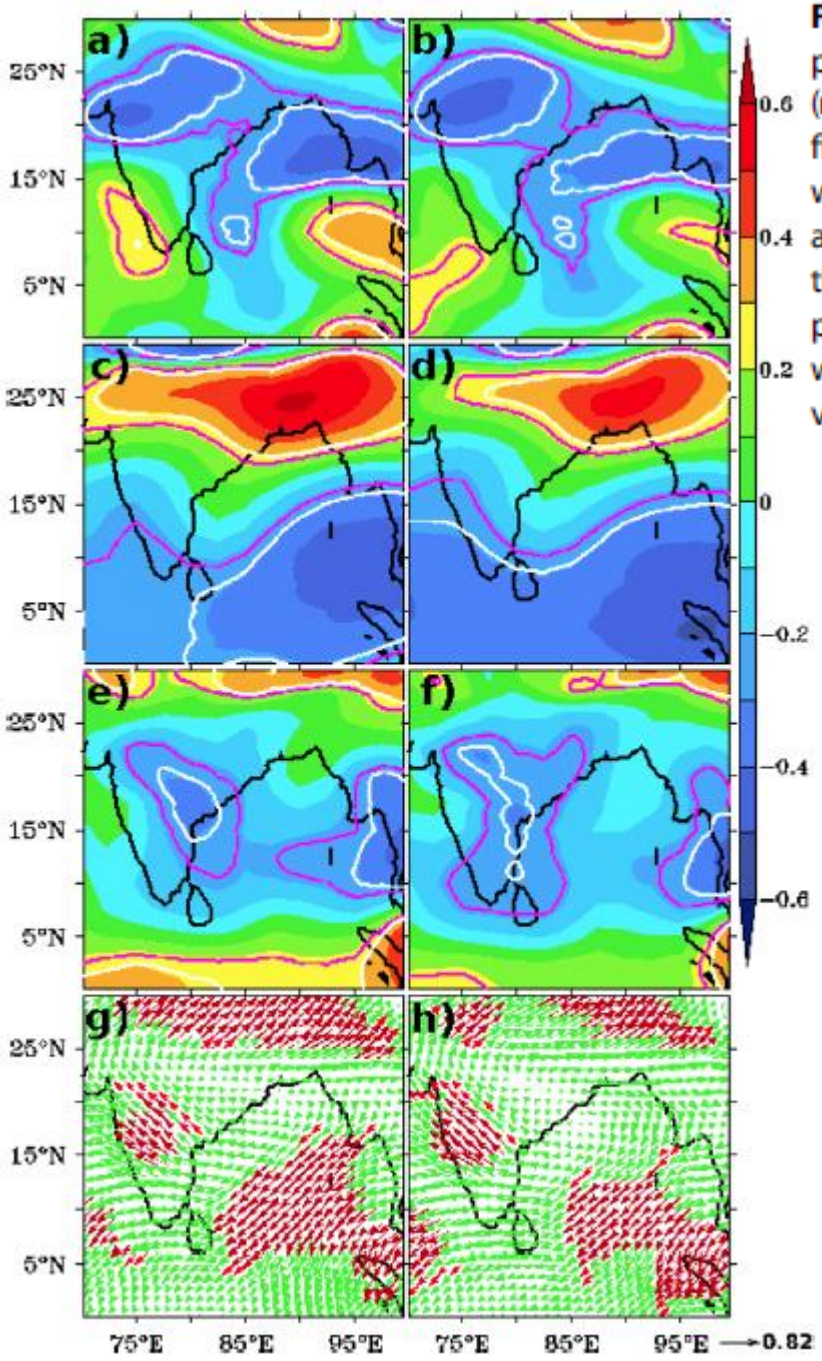

Figure 9. The correlation between the Atl3 index and different atmospheric parameters for the simultaneous months of June–August (left) before and (right) after removing ENSO signal from both the index and respective fields. (a and b) Low-level (850 hPa) vorticity anomaly, (c and d) vertical wind shear anomaly, (e and f) midtroposphere (600 hPa) humidity anomaly, and (g and h) integrated moisture transport. In Figures 9a–9f, the pink and white contours indicate 80% and 90% confidence levels as per two-tailed Student's t test, respectively. In Figures 9g and 9h, vectors with 80% and 90% confidence levels are marked in brown and red line vectors, respectively, with all else in light green.

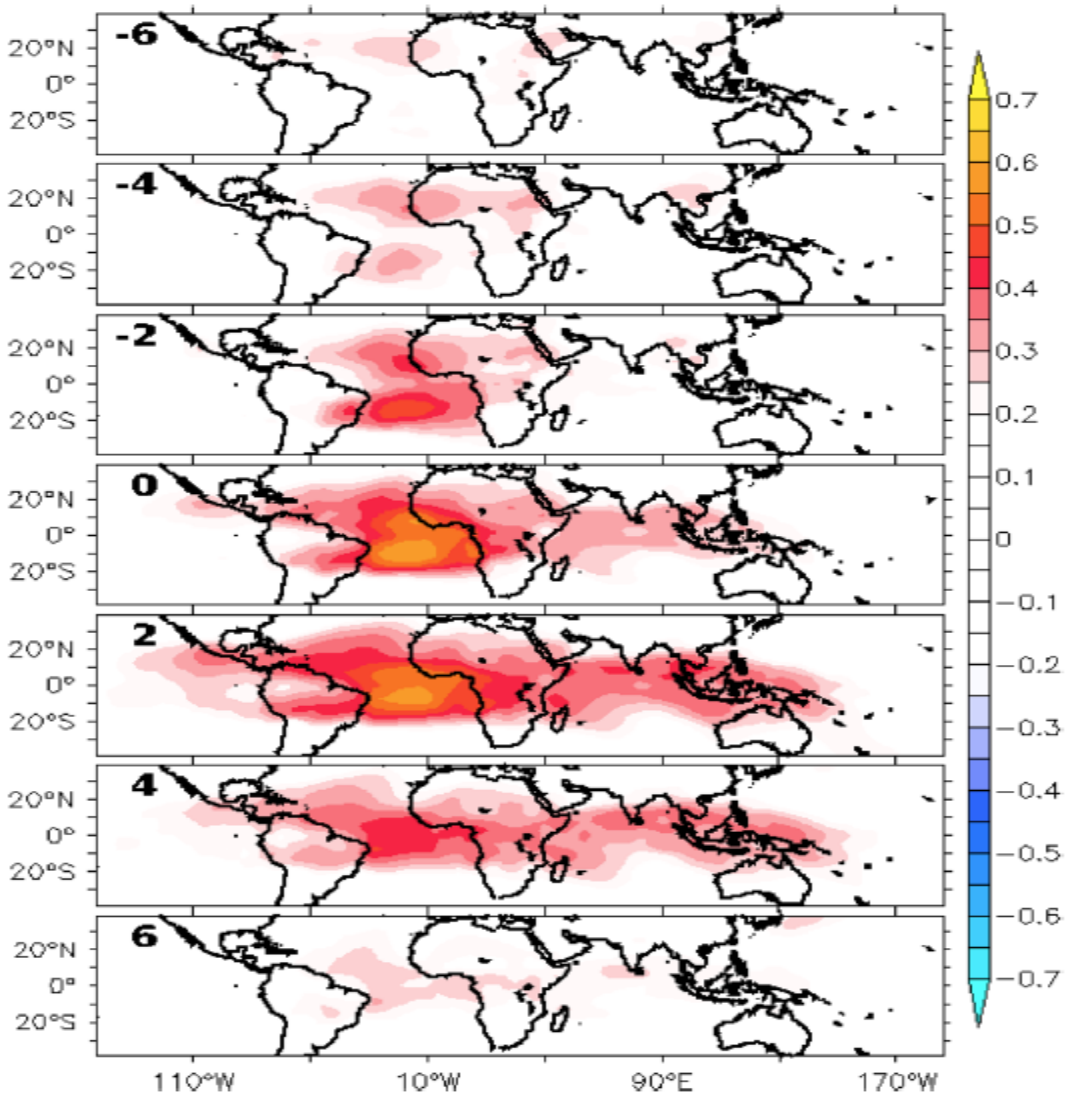

Figure 10. Bimonthly lead-lag correlations between the Atl3 index and the $\overline{TT}$ anomalies (troposphere temperature anomaly averaged between 1000 hPa and 200 hPa) after removing the ENSO influence from both the fields for the period 1979–2012. The number on each subfigure indicates the lag or lead time of $\overline{TTA}$ with respect to Atl3 index in months. In the figure positive correlation indicates the enhancement of $\overline{TTA}$ with respect to warm phase of AZM. All the shaded values are statistically significant by 95% confidence level by Student's *t* test.

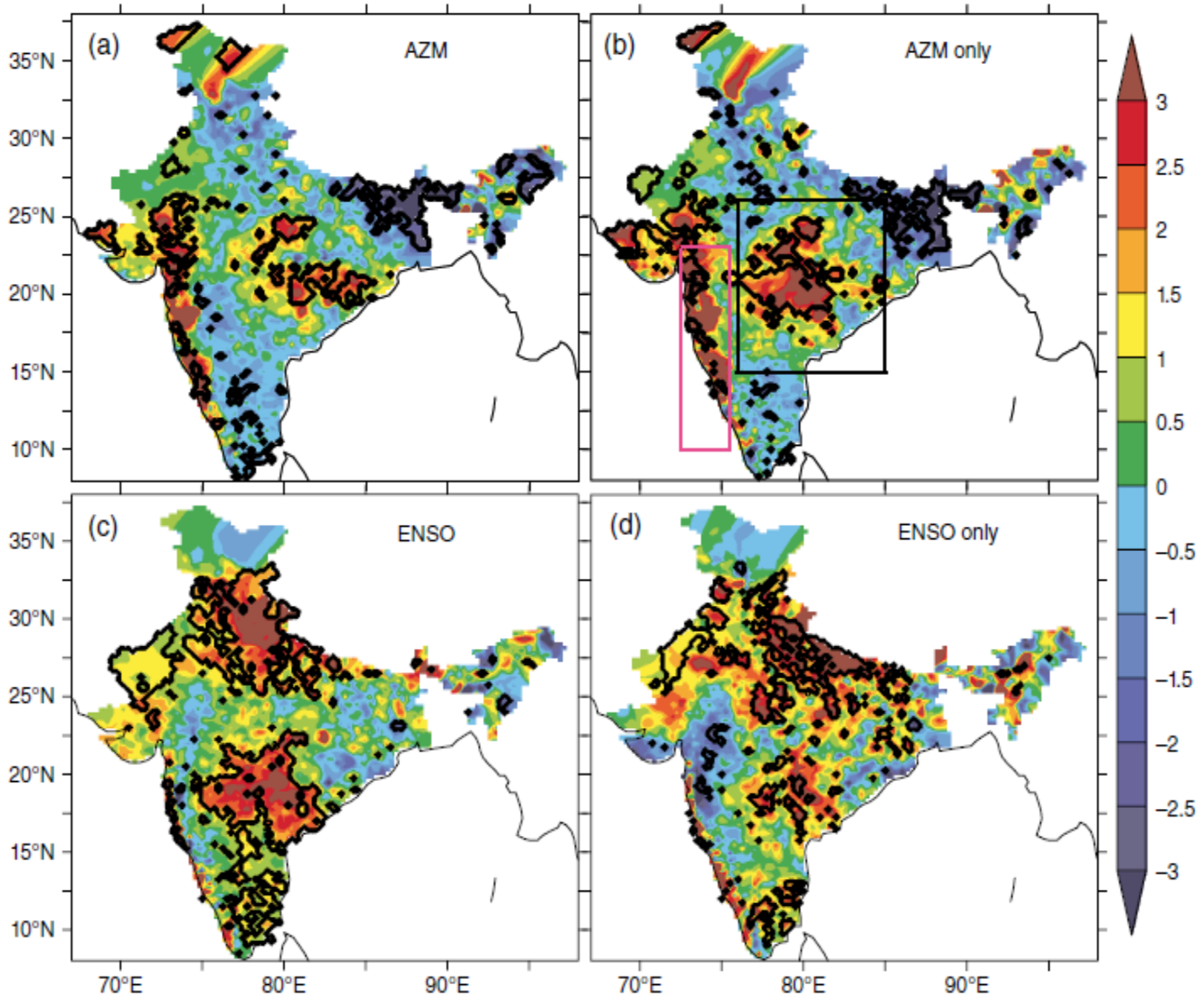

Figure 1. Differences of composites of rainfall between the cold and warm years of (a) AZM, (b) AZM only (excluding those co-occurring with ENSO), (c) ENSO, and (d) ENSO only (excluding ENSO co-occurring with AZM). The two regions selected for the analysis, i.e., central India (15°–26°N and 76°–85°E; big thick box (black in online)) and the Western Ghats (10°–23°N and 72.5°–75.5°E; small light box (pink in online)) are shown in (b). The contours in black colour indicate 90% significance level.

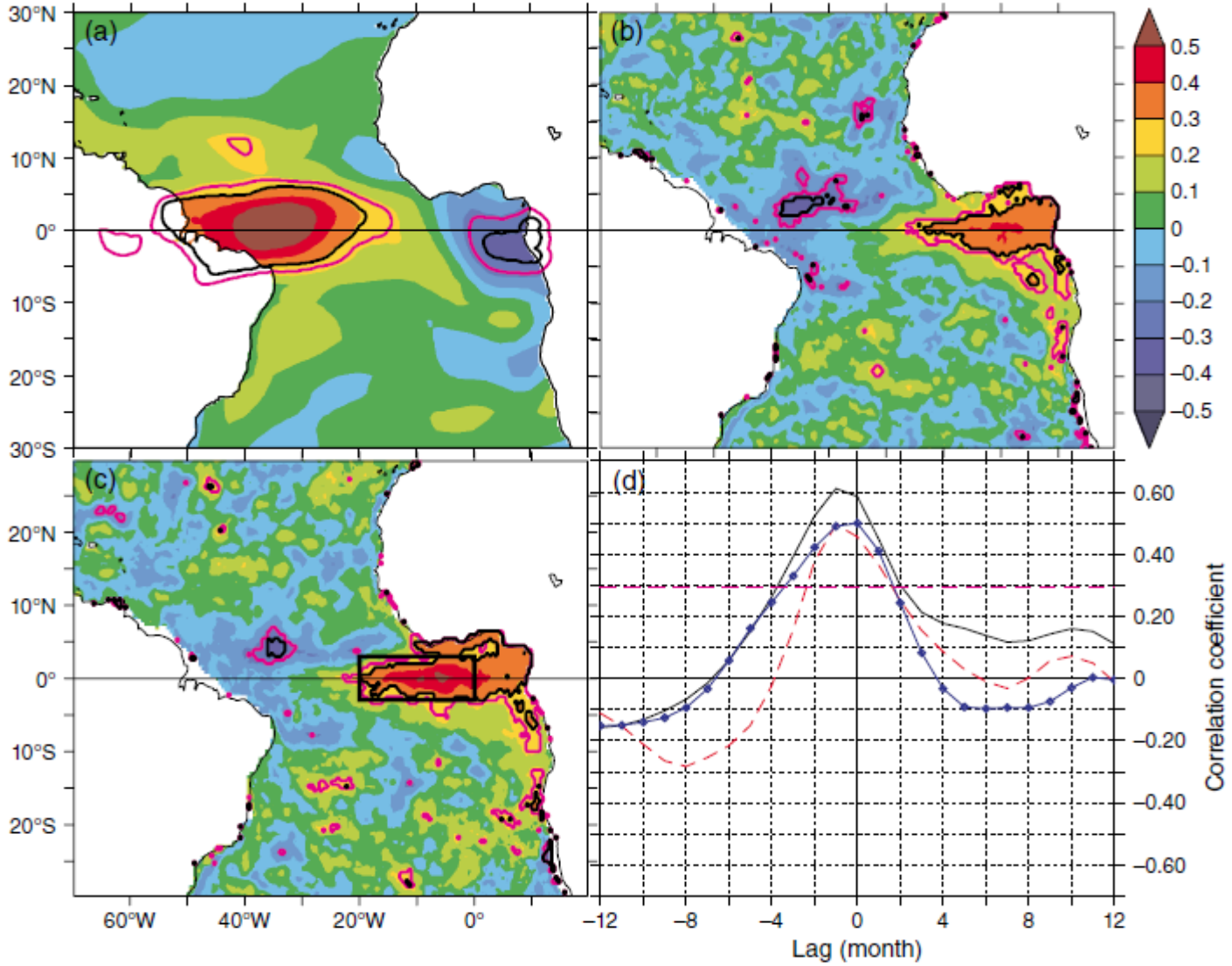

Figure 2. Spatial correlations between the anomalies of (a) SST in the Atl3 region and zonal winds, (b) western equatorial Atlantic (3°S–3°N and 40°–20°W; WEA) zonal winds and heat content, (c) east equatorial Atlantic (3°S–3°N and 5°W–10°E; EEA) heat content and SST, and (d) monthly lead–lag correlations between anomalies of SST in the Atl3 region and WEA zonal wind (black), WEA zonal wind and EEA heat content (dashes in red) and EEA heat content and Atl3 (diamonds in blue). The zonal winds are taken at 850 hPa level. In spatial correlation plots (a–c), contours of 80 and 90% significance are indicated in light and thick (pink and black colours) in online, respectively, and in (d), the level of 90% significance is indicated by a dashed horizontal (pink dashed in online) line. The correlations over land are masked in (a) to highlight the same over the ocean. The black box in (c) indicates the Atl3 region.

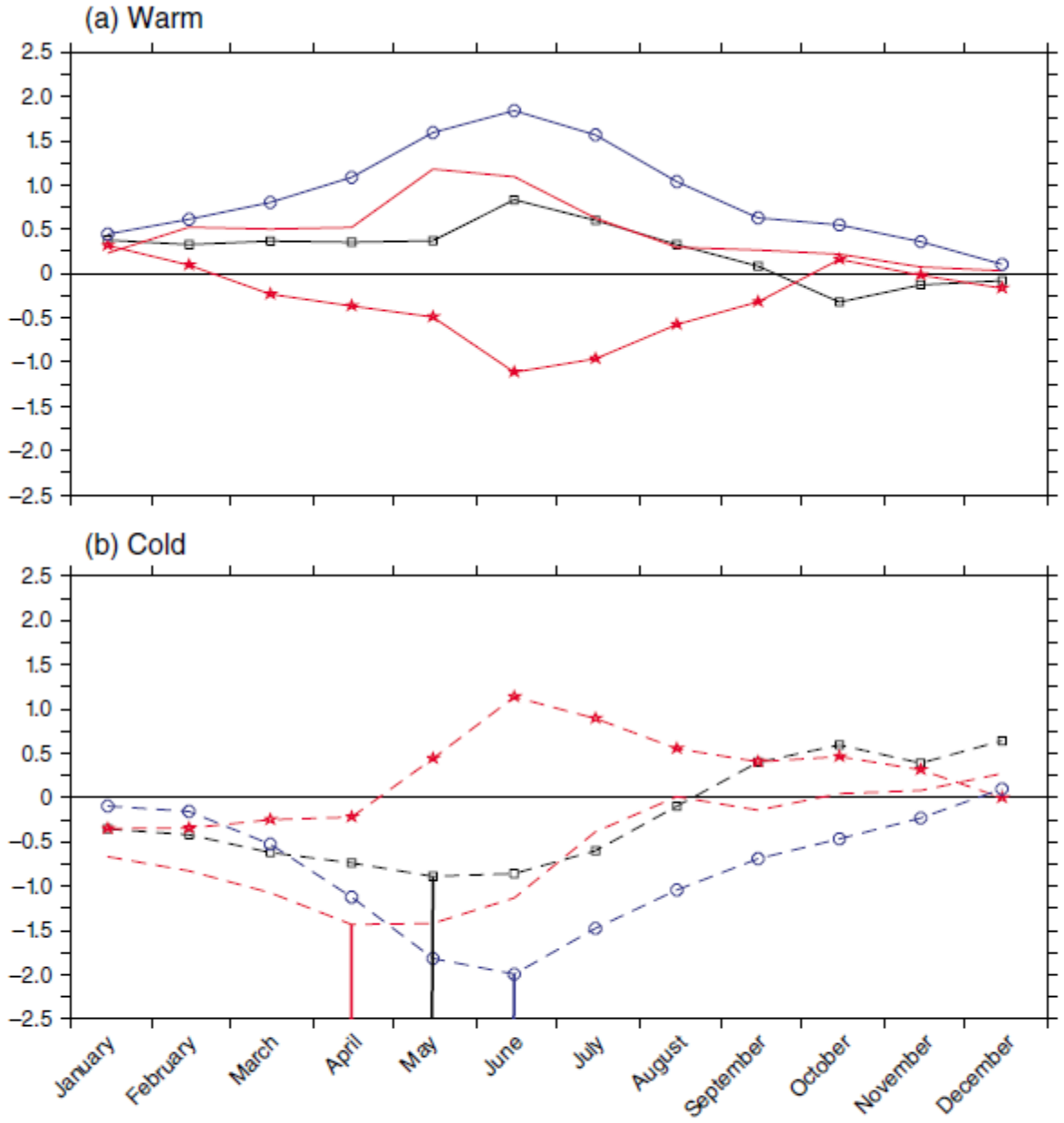

Figure 3. Evolution of composites of anomalies of western equatorial zonal wind (red; no symbol), eastern equatorial zonal wind (stars in red), eastern equatorial heat content (squares in black), and SST in the Atl3 region (circles in blue) during the warm (solid line) and cold (dashed line) years of AZM. All the fields are normalized before compositing. The zonal winds are taken at 850 hPa level. The peaks of different fields plotted are marked as vertical lines in their respective colours.

Correlation between the MAM ITCZ position and JJAS (Aug.-Sep.) rainfall over India

MAM ITCZ vs JJAS rainfall

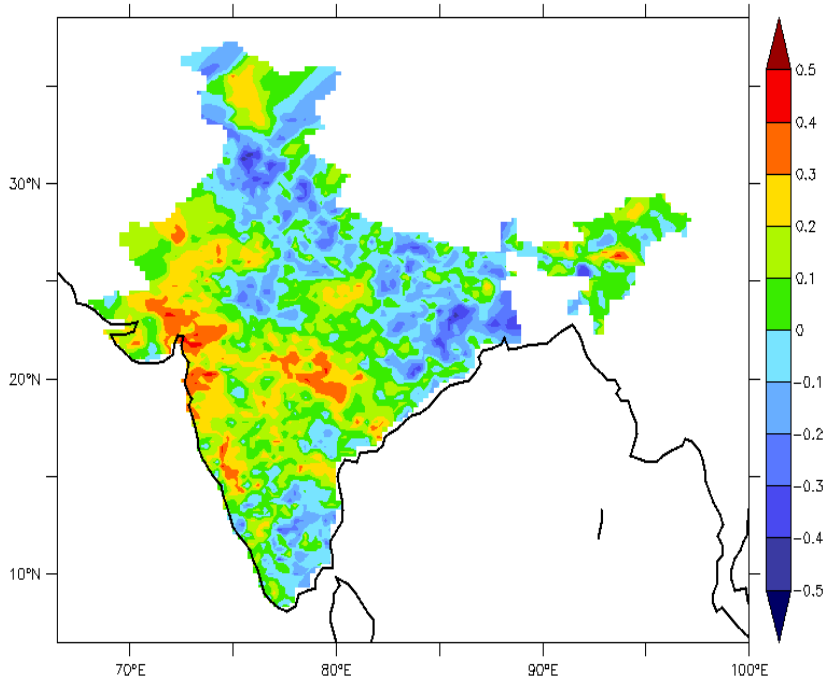

MAM ITCZ vs AS rainfall

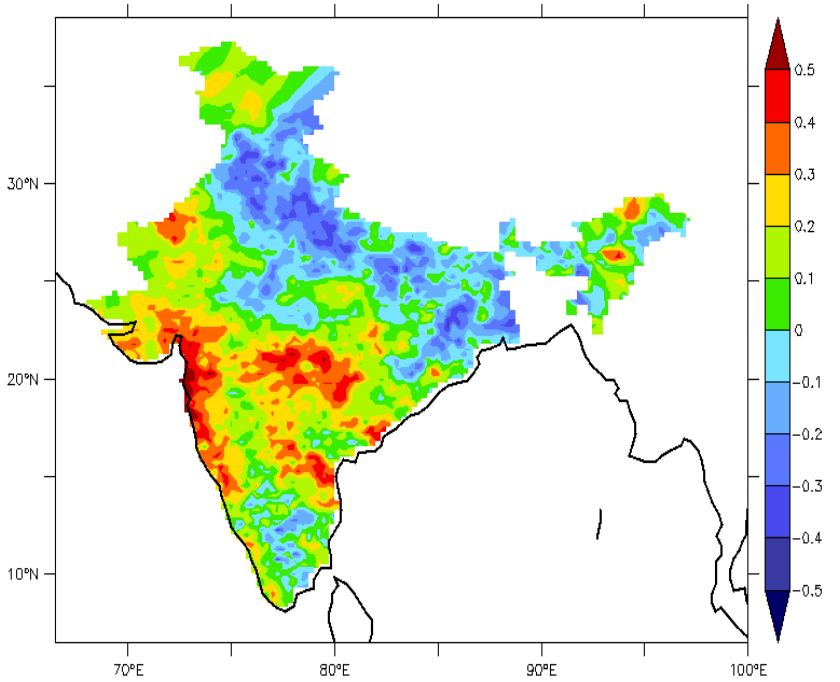

mm/day

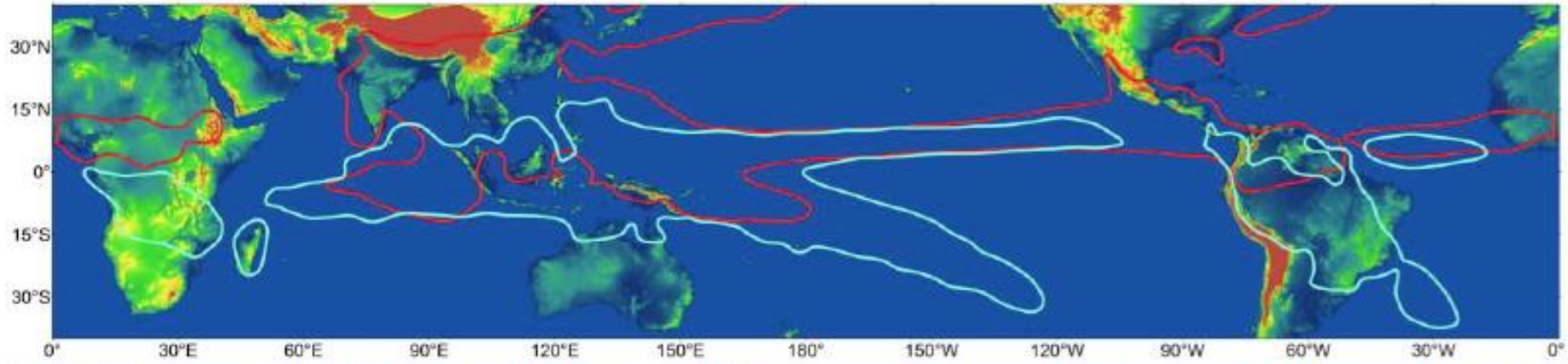

Figure 4. Boreal summer (red) and winter (cyan) positions of 3 mm/day precipitation contours are shown to highlight the multi-scale nature of the subseasonal to interannual processes within the IMME complex, the associated land and ocean processes, and their interdependences. Key processes include Bjerknes feedback in each of the tropical oceans and the sensitivity of precipitation to SST and terrestrial hydrology in the tropical band, coupling strengths over land and the oceans as manifest in interactions between lower tropospheric humidity, latent heat fluxes, SSTs, and soil moisture variability, and shortwave feedbacks via the sensitivity of cloud amounts to precipitation variability.

Performance of Southwest Monsoon 2016 in India from June 1 to September 13

Region	Actual rainfall in mm	Normal rainfall in mm	Excess/Deficit
East and Northeast India	1111.9	1280.5	-13%
Central India	902.1	895.6	1%
Northwest India	558.7	568.5	-2%
South Peninsula	545.9	617.9	-12%

Multi-Scale Interactions between MJOs and the ITF

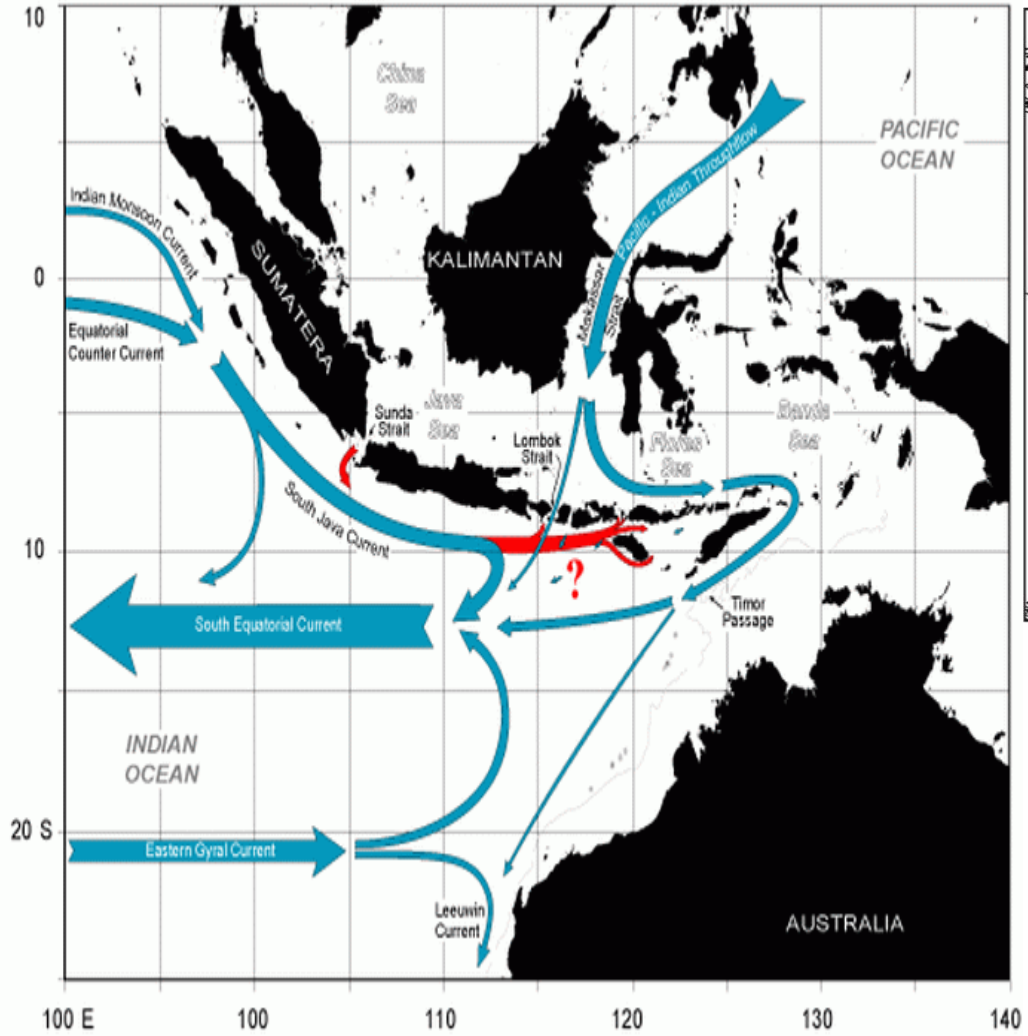

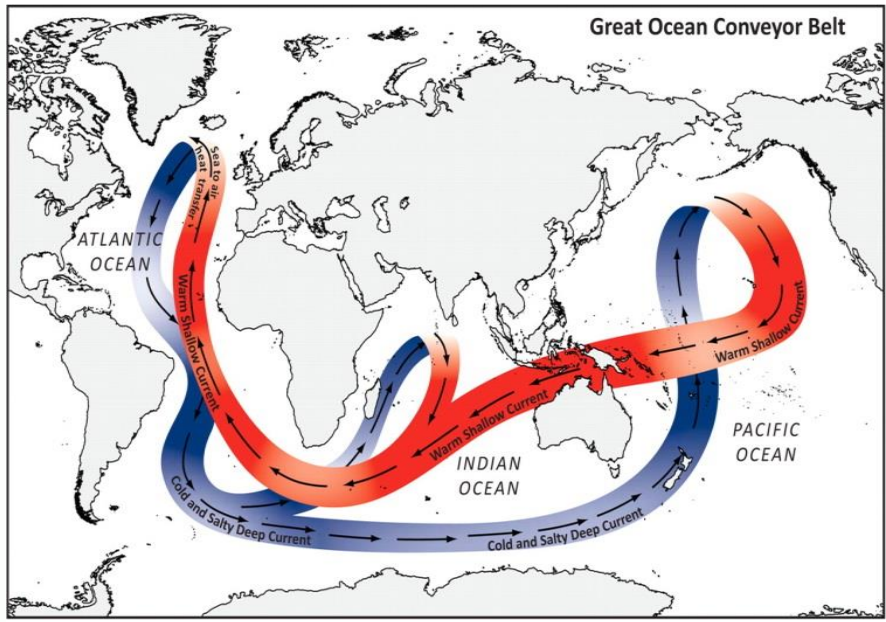

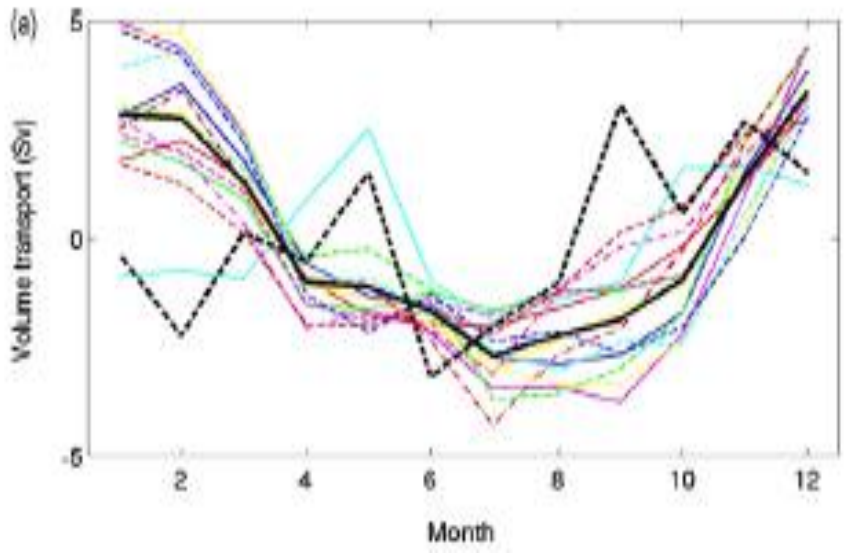

Can We think of it as a Capacitor linking the two Warm Pools?

SSTs off Java and Sumatra hover around convective thresholds. Can ITF push SSTs to trigger feedbacks?

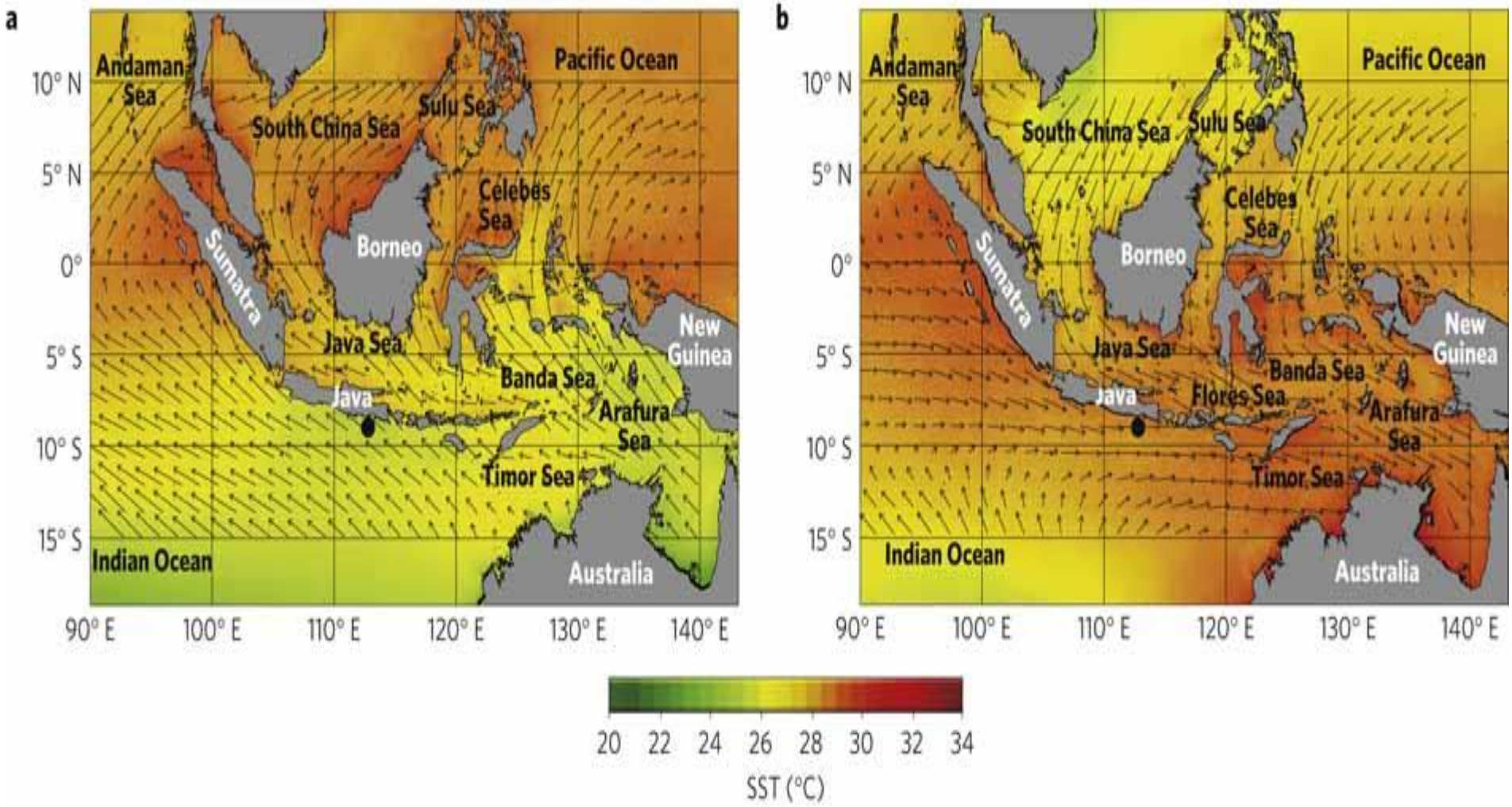

Can ISV in ITF produce coupled positive feedbacks?

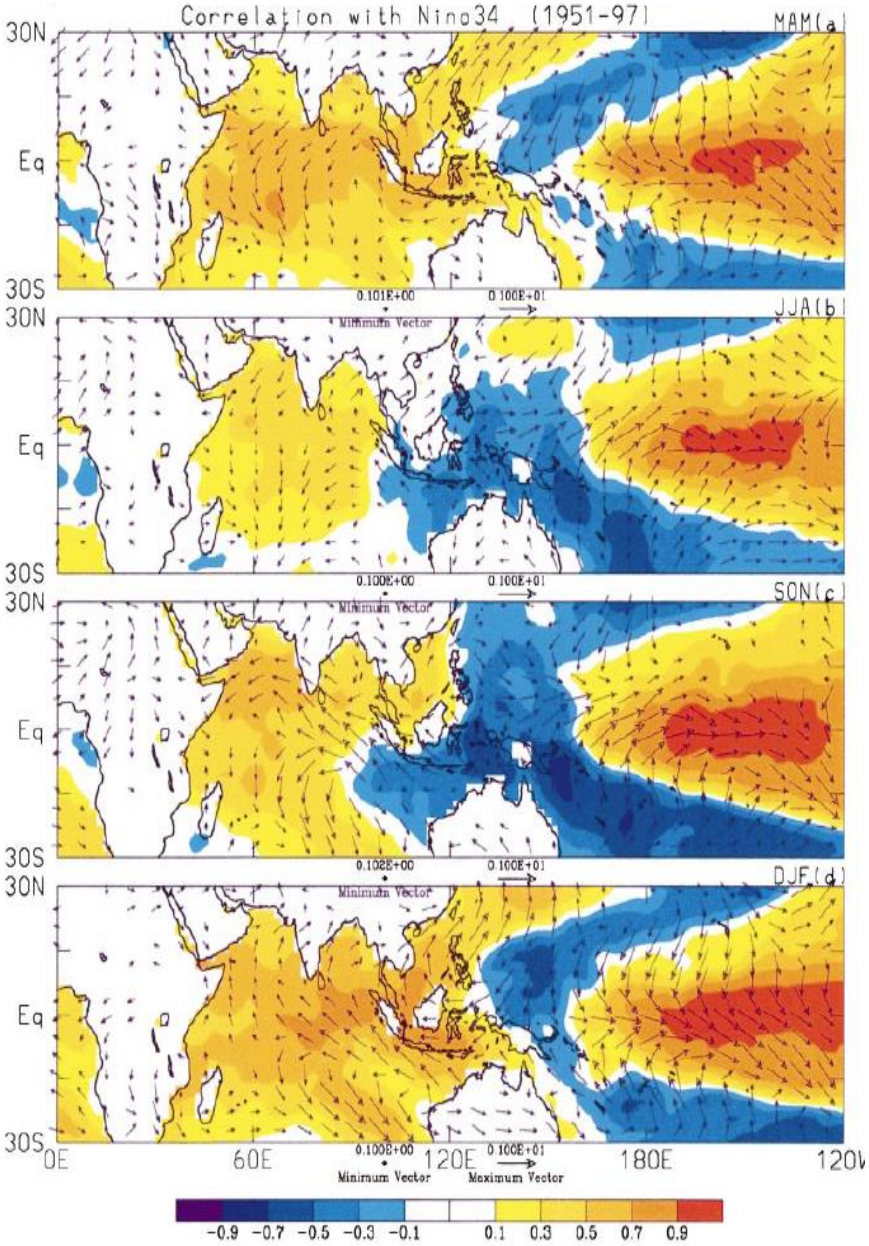

FIG. 5. Seasonal correlation of Niño-3.4 with SST and surface winds for (a) MAM, (b) JJA, (c) SON, and (d) DJF. Plotting convention is same as in Fig. 4.

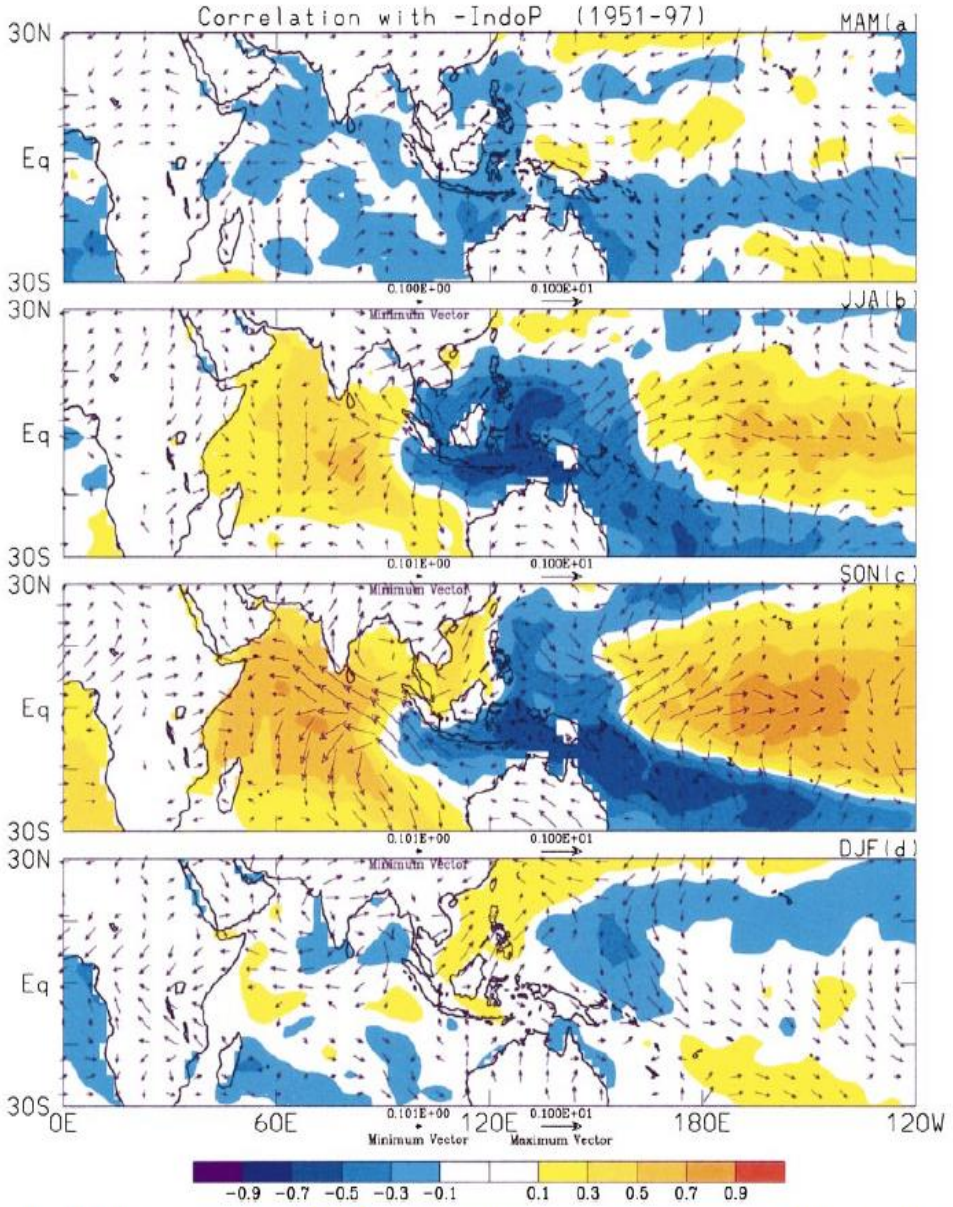

FIG. 4. Simultaneous correlation of −IndoP with SST (shading) and surface winds (max vector is length 1.) for the (a) MAM, (b) JJA, (c) SON, and (d) DJF seasons. A correlation of approximately 0.24 is significantly different than zero at the 95% confidence level, assuming 46 degrees of freedom (i.e., assuming each year is independent).

ISVs in ITF can be generated from Both Indian and Pacific Oceans

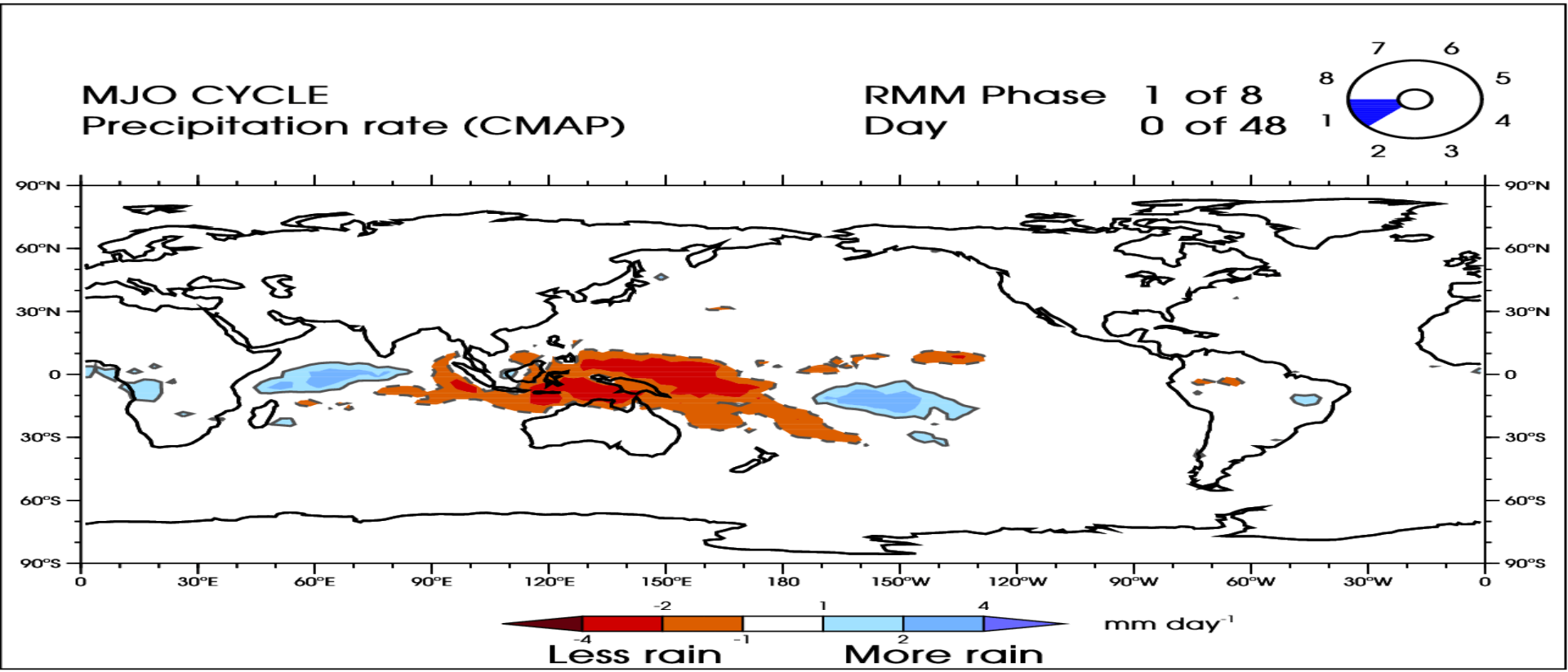

Figure 1. MJO cycle of precipitation anomalies (CMAP data set). The life cycle is calculated from MJO events in the November-April (northern hemisphere winter) season only. Composite maps were calculated for each of the 8 RMM phases, and linearly interpolated for the intermediate days to give a smooth cycle. In addition to the colour shading, a thick solid contour at 1 mm day^{-1} outlines the region of enhanced rainfall, and a thick dashed contour at -1 mm day^{-1} outlines the region of suppressed rainfall. These contours are reproduced in subsequent animations below to indicate the main regions of MJO precipitation. Animations stolen from Adrian Matthews, UEA, UK

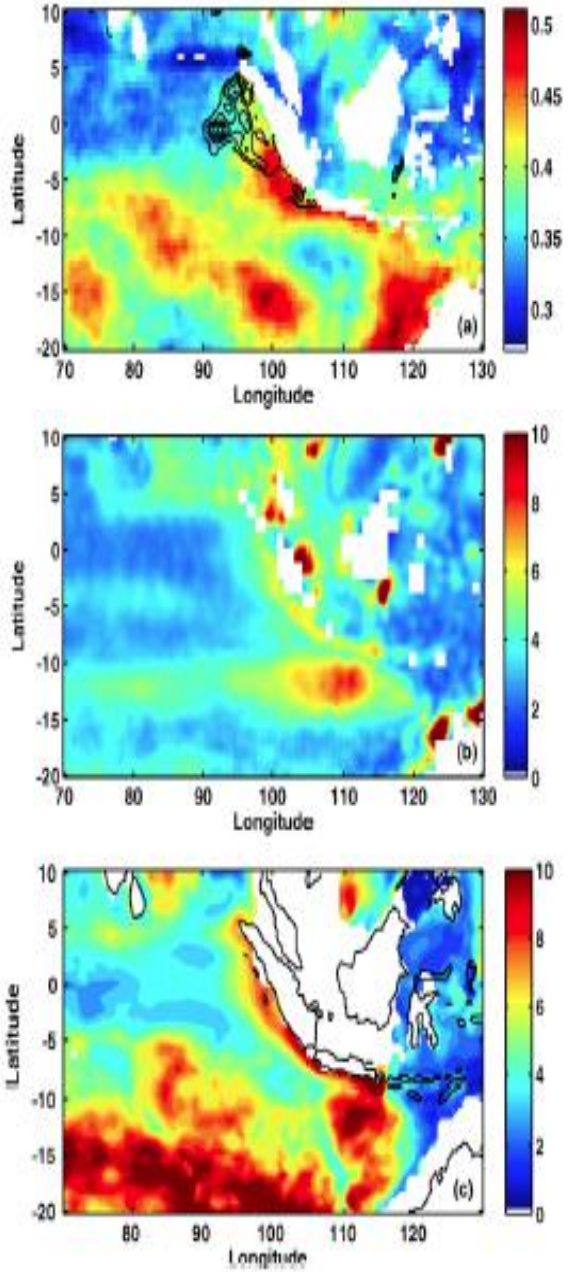

Fig. 5. $\overline{T}$ of intraseasonal SST anomalies (a), intraseasonal SSH anomalies (b), and intraseasonal D20 (c). The unit of SST anomalies is °C, the unit of SSH anomalies is cm, and the unit for D20 is m. The black contours in (a) are the barrier layer depths, starting from 16 m with an interval of 2 m.

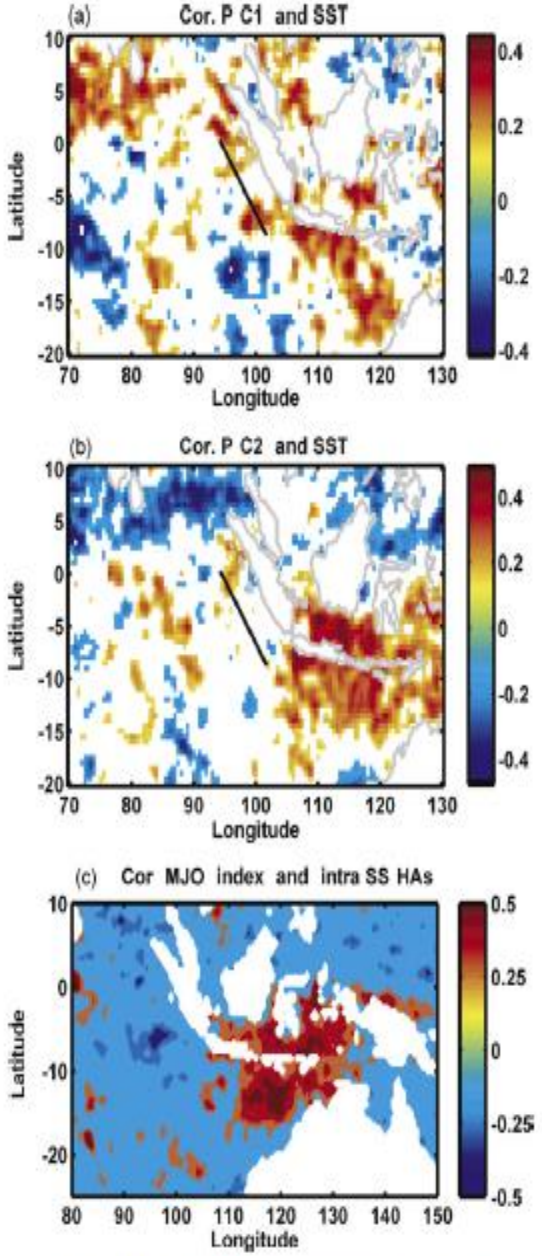

Fig. 6. (a) Correlation between significant daily PC1 (PC1 > 2) and the corresponding intraseasonal SST anomalies. (b) Correlation between distinct daily PC2 (PC2 < –2) and the corresponding intraseasonal SST anomalies. (c) Correlation between significant MJO events (MJO index > 2) and the intraseasonal SSH anomalies. The values in (b) are reversed, so that positive values represent sea surface warming and negative values represent sea surface cooling in both (a) and (b). Only statistically significant correlations at the 95% confidence level are shown.

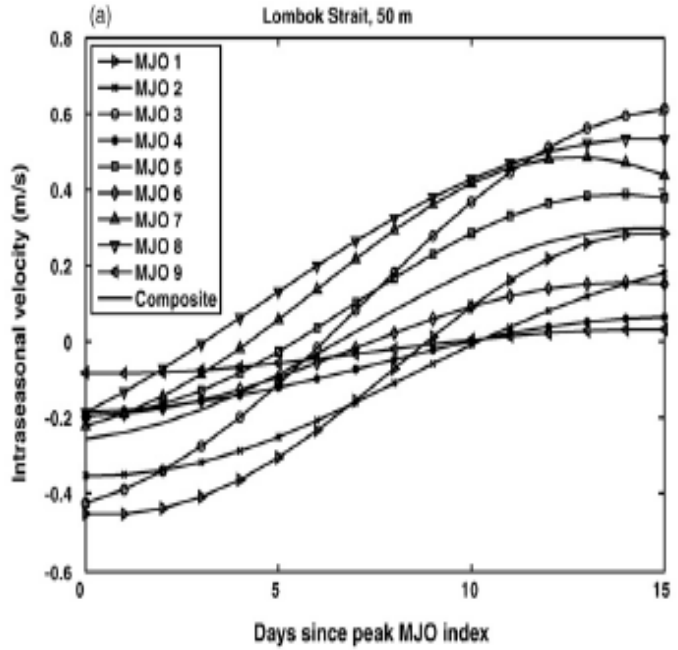

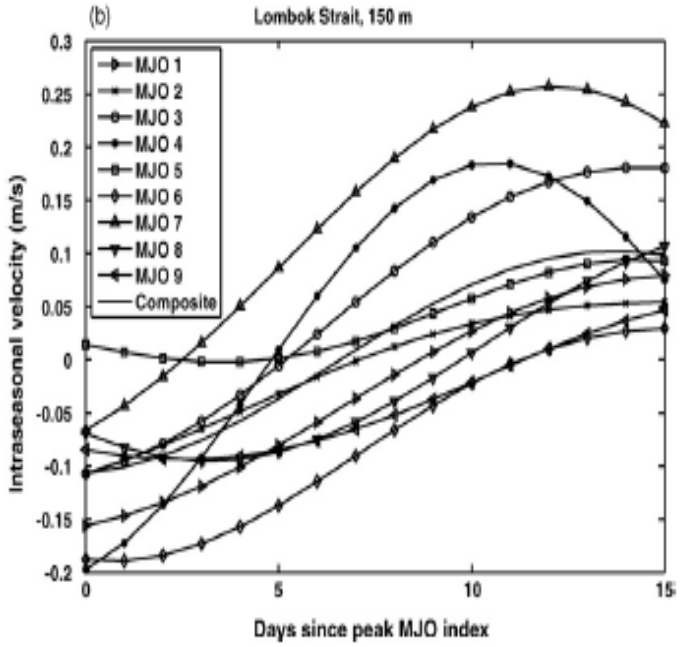

Fig. 10. Intraseasonal meridional currents at 50 m (a) and 150 m (b) in the Lombok Strait. The zeroth day is the day with a peak MJO index, which are marked with circles in Fig. 1.

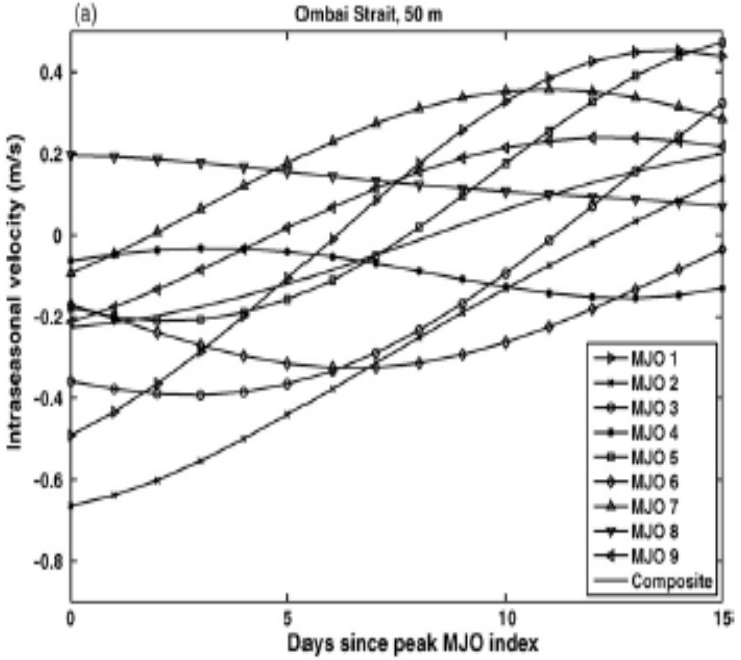

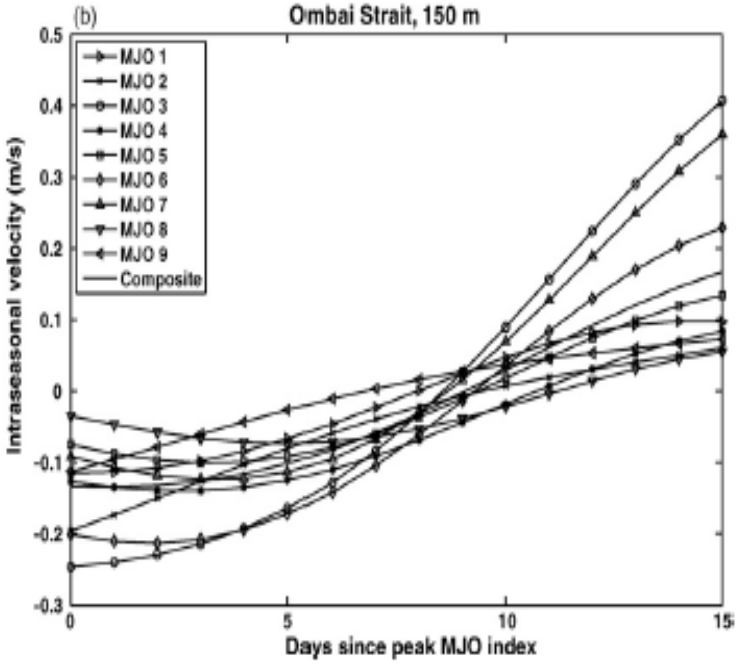

Fig. 11. Intraseasonal zonal currents at 50 m (a) and 150 m (b) in the Ombai Strait. The zeroth day is the day with a peak MJO index, which are marked with circles in Fig. 1.

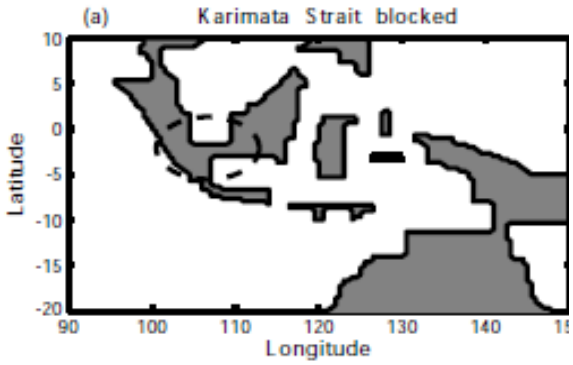

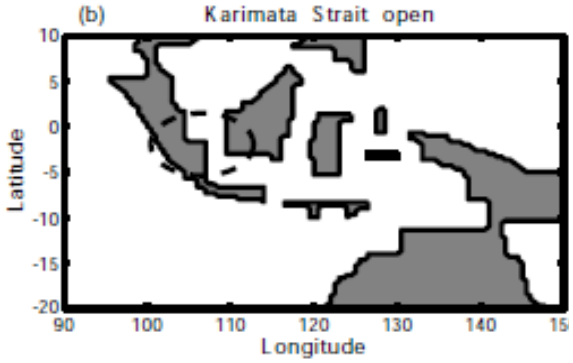

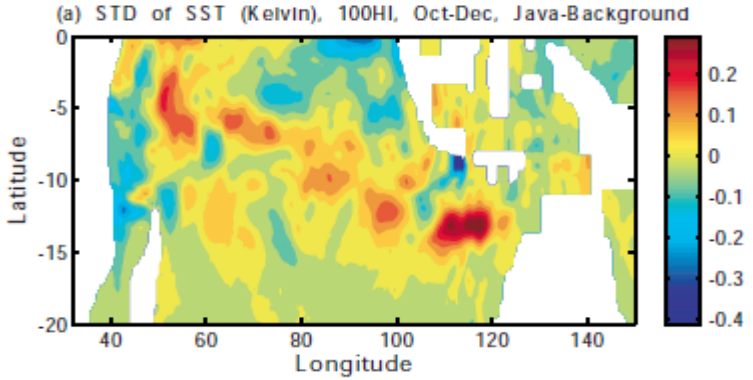

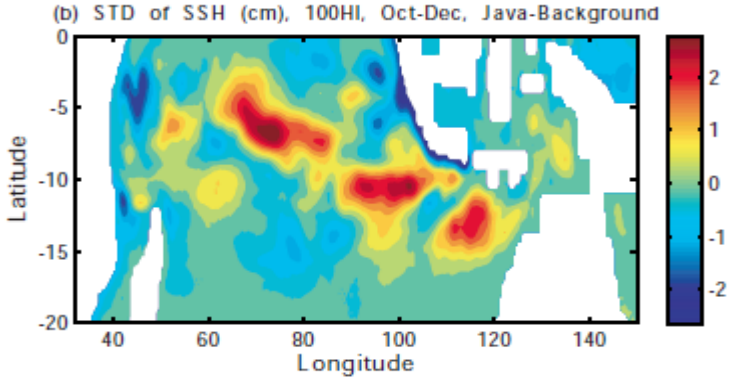

Each strait has a unique impact on the Indian Ocean. Coupled feedbacks may be opening and closing different valves..

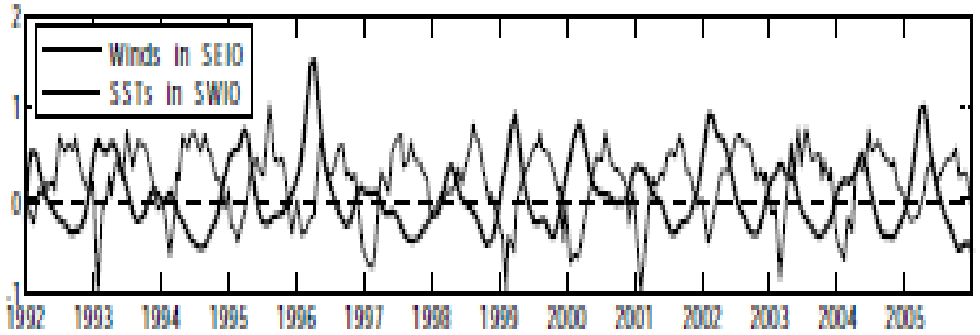

Small errors in transports or winds in the Indonesian Seas can have large impacts on the SWIO. We have no idea how they may be amplified by coupled feedbacks with IndoP

MJOs produce a seasonal-rectification and a thermocline-intensified response

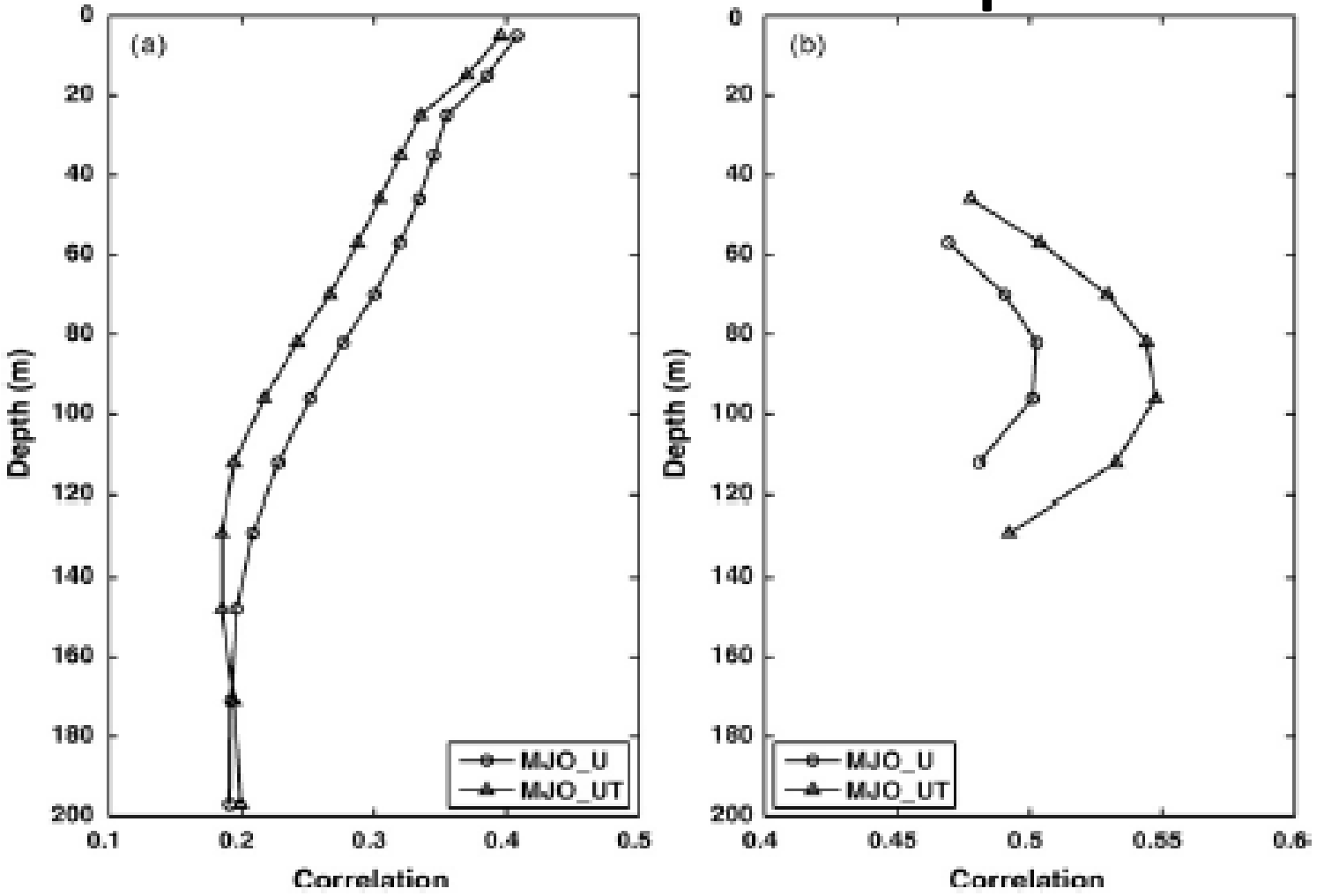

Fig. 14. (a) Correlations between the 5-day MJO index and the zonal velocity, as well as correlations between the 5-day MJO index and zonal temperature advection. (b) Correlations between the annual MJO index and the annual mean zonal velocity, as well as correlations between the annual MJO index and annual mean temperature advection. The zonal velocity and temperature advection are averaged between 10°S and 15°S at 114°E. The correlations are statistically significant at a confidence level of 95%.

ITF waters induce baroclinic instability in the Southern IO

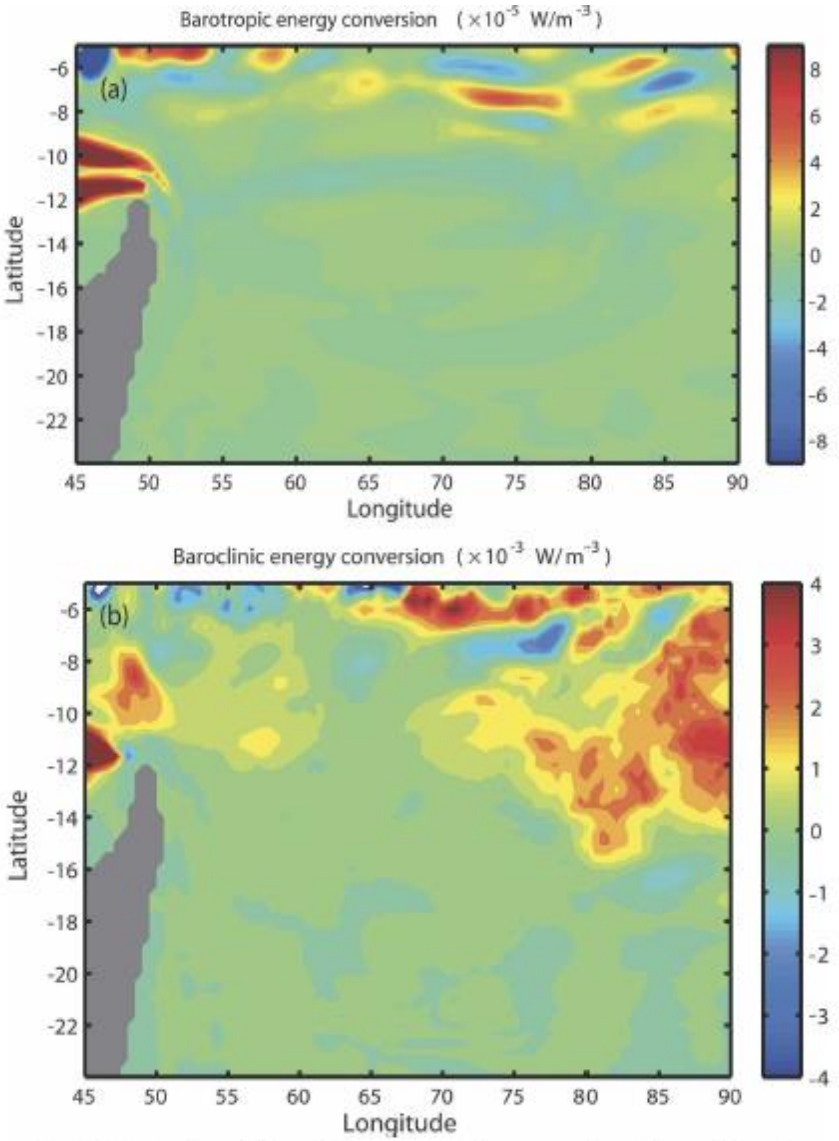

FIG. 5. (a) Barotropic and (b) baroclinic energy conversions averaged over 20 yr and above the thermocline in the SWIO.

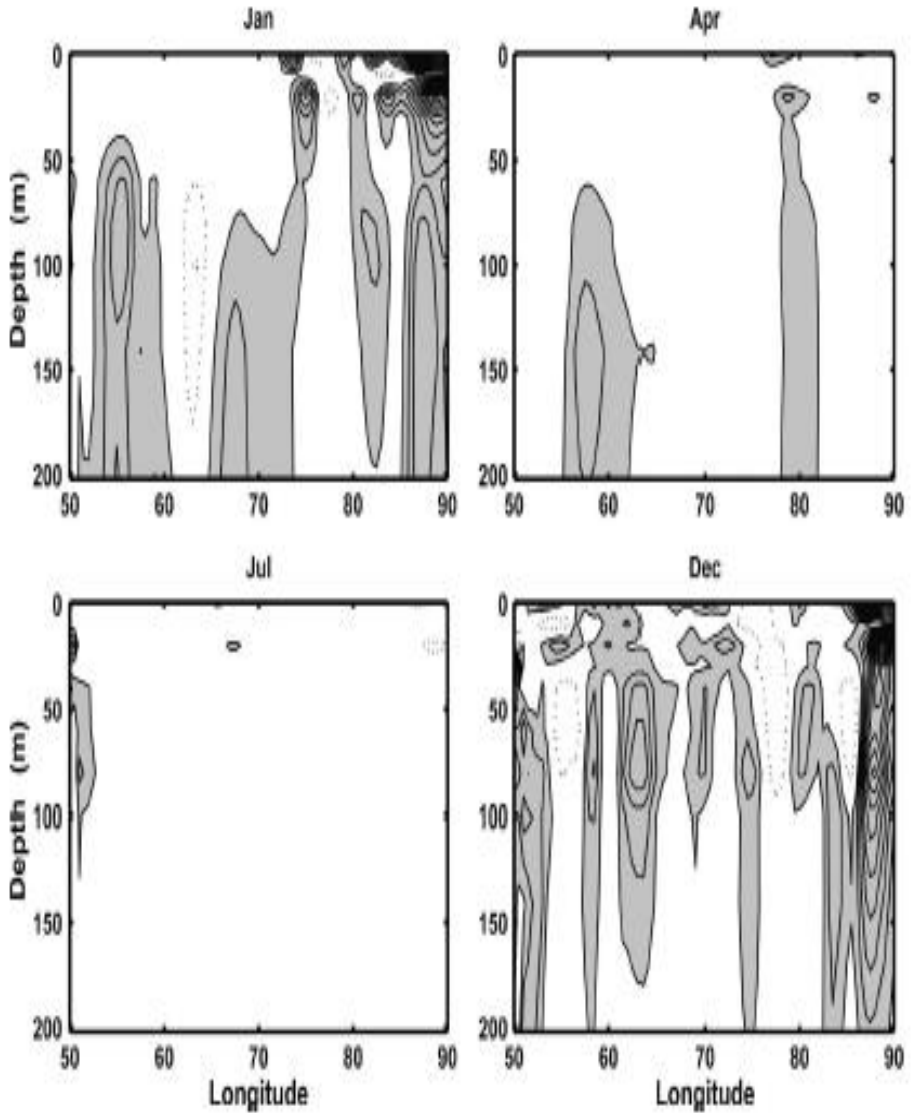

FIG. 7. Longitude–depth plots of baroclinic energy conversions for January, April, July, and December. The contour interval is 1×10^{-3} W m^{-3}. Regions with positive values are shaded.

We can use the PV conservation equation to calculate spatio-temporal scales of the Eady waves

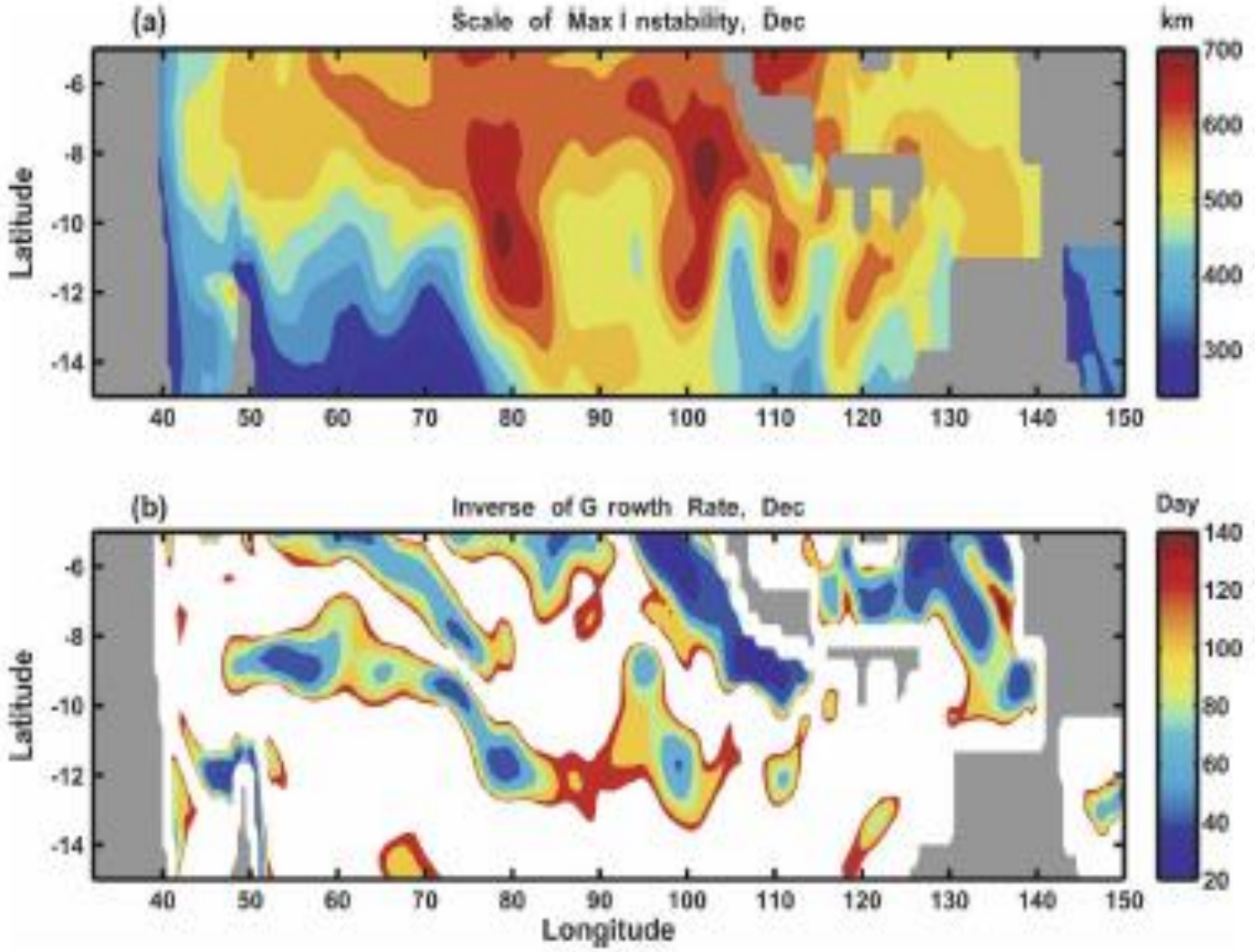

FIG. 7. (a) Wavelength of the maximum instability ($L_{max} = 3.9L_d$) and (b) the inverse of the corresponding maximum growth rate ($\sigma_{max} = 0.3U/L_d$), both in December.

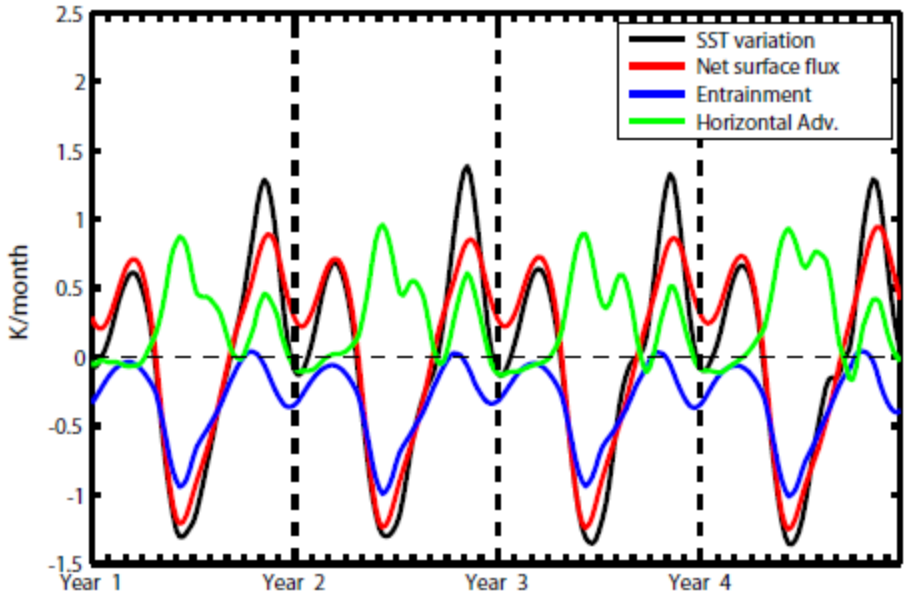

Figure 8 SST variation, net surface heat flux, entrainment, and horizontal temperature advection averaged within a rectangular region 6°S-7°S, 63°E-73°E, which are smoothed with the one-month running mean. Positive values mean that the upper mixed layer gain heat, while negative values mean that the upper mixed layer lose heat.

Warm Entrainment in late fall – early winter months because of ITF

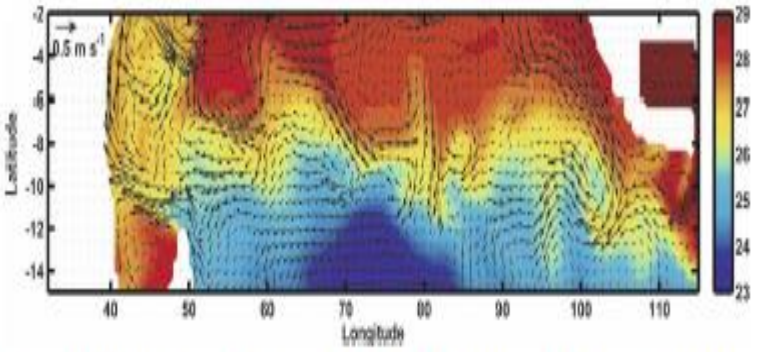

FIG. 11. Weekly mean SSTs (see color codes, °C) and surface velocities (vectors) during 16–21 Nov of year 7, when the warm entrainment reaches its maximum.

Impact on MJO genesis?

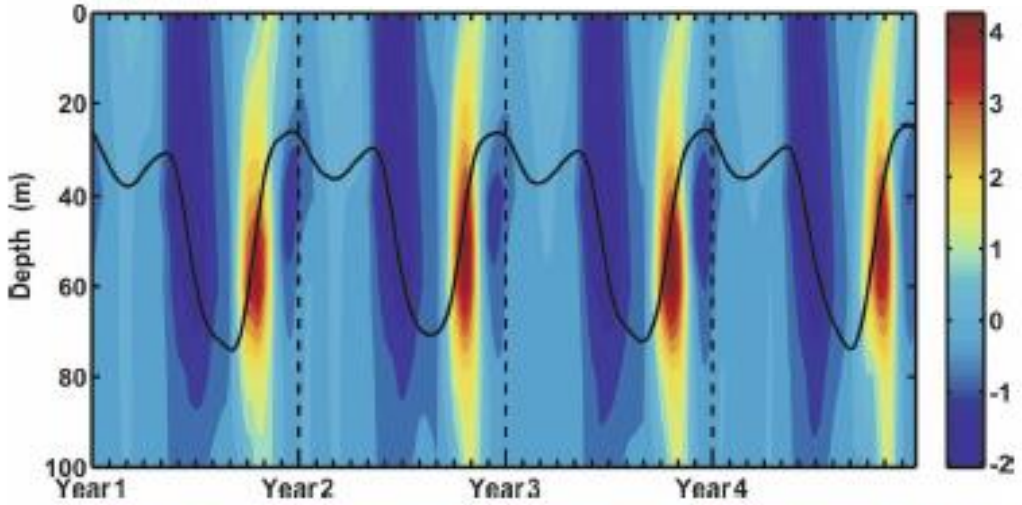

FIG. 9. Temperature variations (see color codes, K month^{-1}) and mixed layer depth (solid line), averaged in the region of 6°–7°S, 63°–73°E.

Both SWIO and SEIO have strong thermocline-SST interactions with potential for coupled feedbacks – via MJO genesis and maritime rainfall.

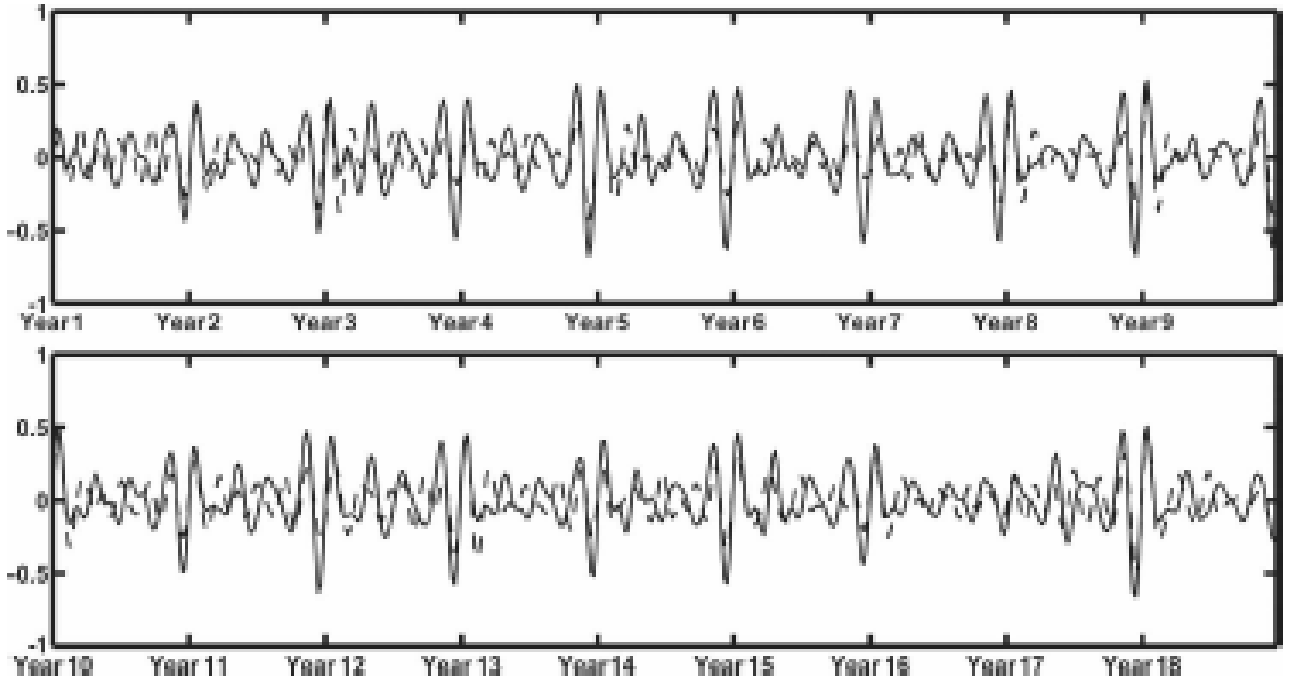

FIG. 12. Intraseasonal entrainment (solid line, K month^{-1}) and intraseasonal SSHAs (dashed line 10 cm) at 8°S, 63°E for 18 yr.

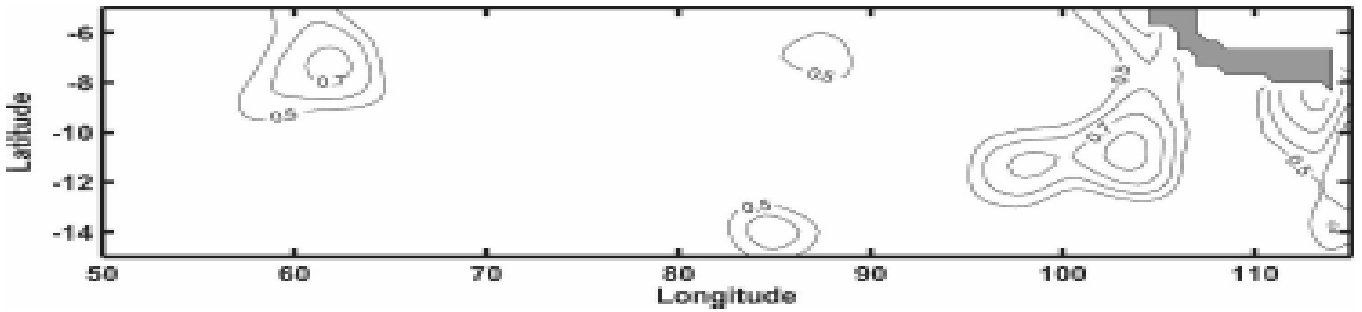

FIG. 13. Correlations between the intraseasonal entrainment and the intraseasonal SSHAs, which are statistically significant at the 95% confidence level.

The pathways in the Indonesian Seas are like valves that determine the properties of waters being injected into the Indian Ocean which in turn determine the ISVs in the southeastern and southwestern Indian Ocean.

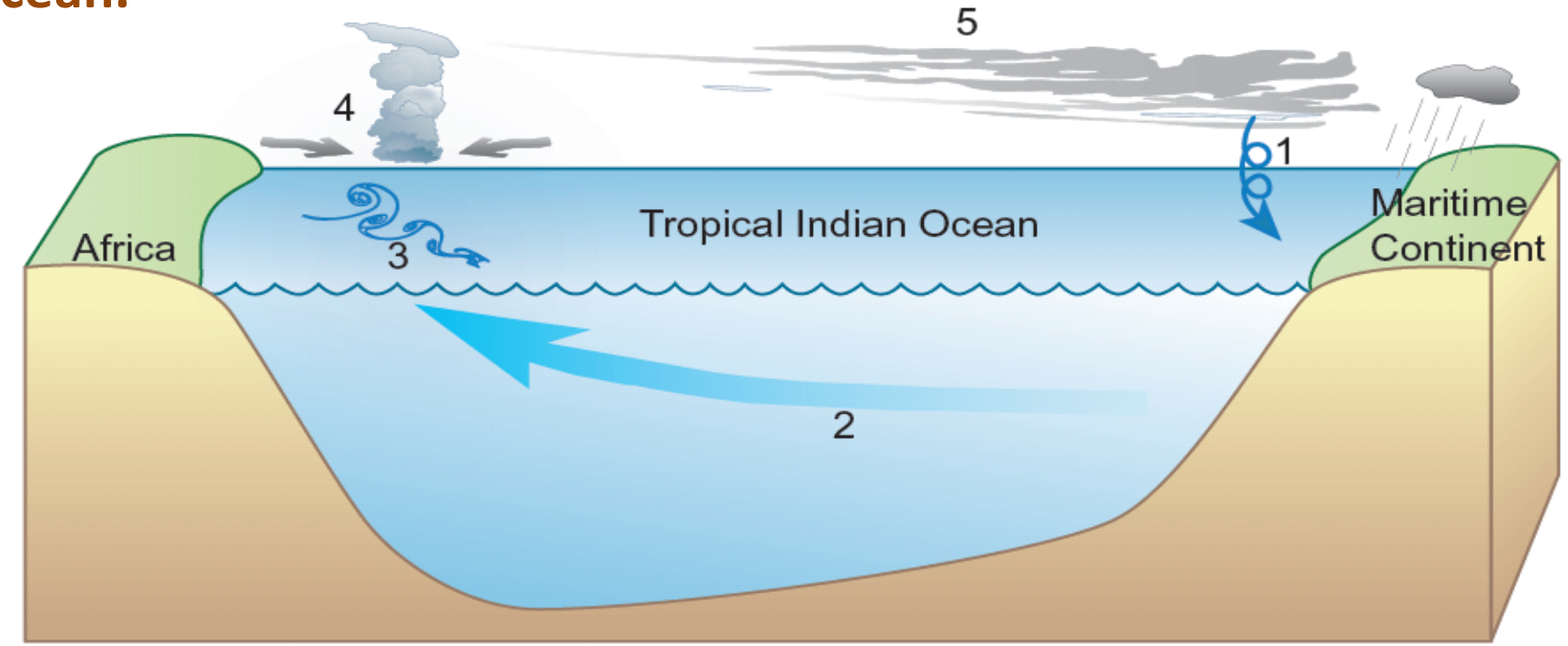

1. Atmosphere forcing on the ocean;
2. Westward propagation in the ocean;
3. Ocean eddy in the upper mixed layer;
4. Ocean feedback to the atmosphere;
5. Eastward propagating MJOs in the atmos.

Model Biases may be amplified if these links are missing

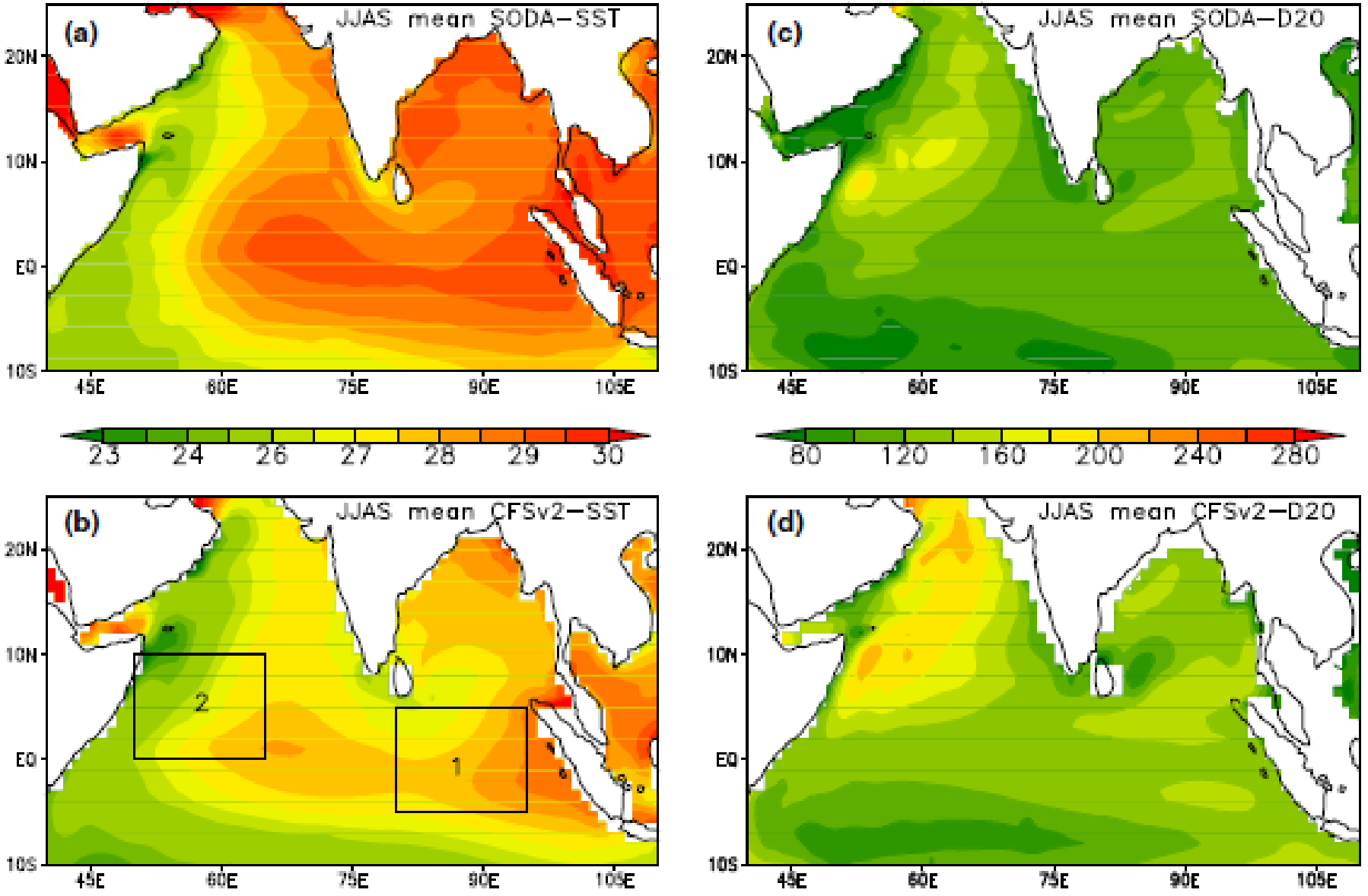

Fig. 8 Seasonal (JJAS) mean SST (°C) from **a** SODA and **b** CFSv2 and D20 (m) from **c** SODA and **d** CFSv2

More Paleo studies are needed to link the global monsoon components

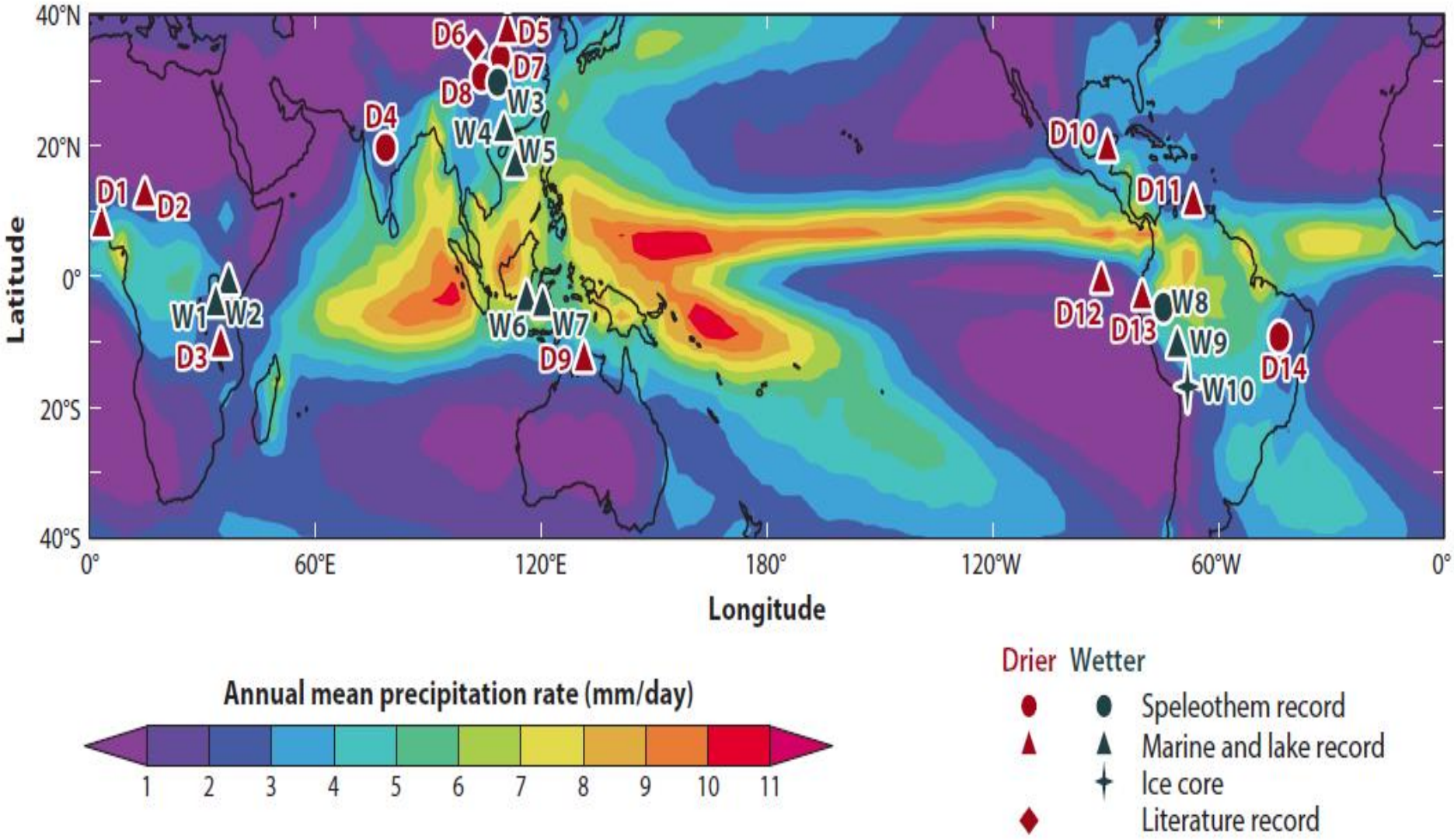

Feedbacks From the Global Monsoon To ENSO Remain To be Fully under-stood

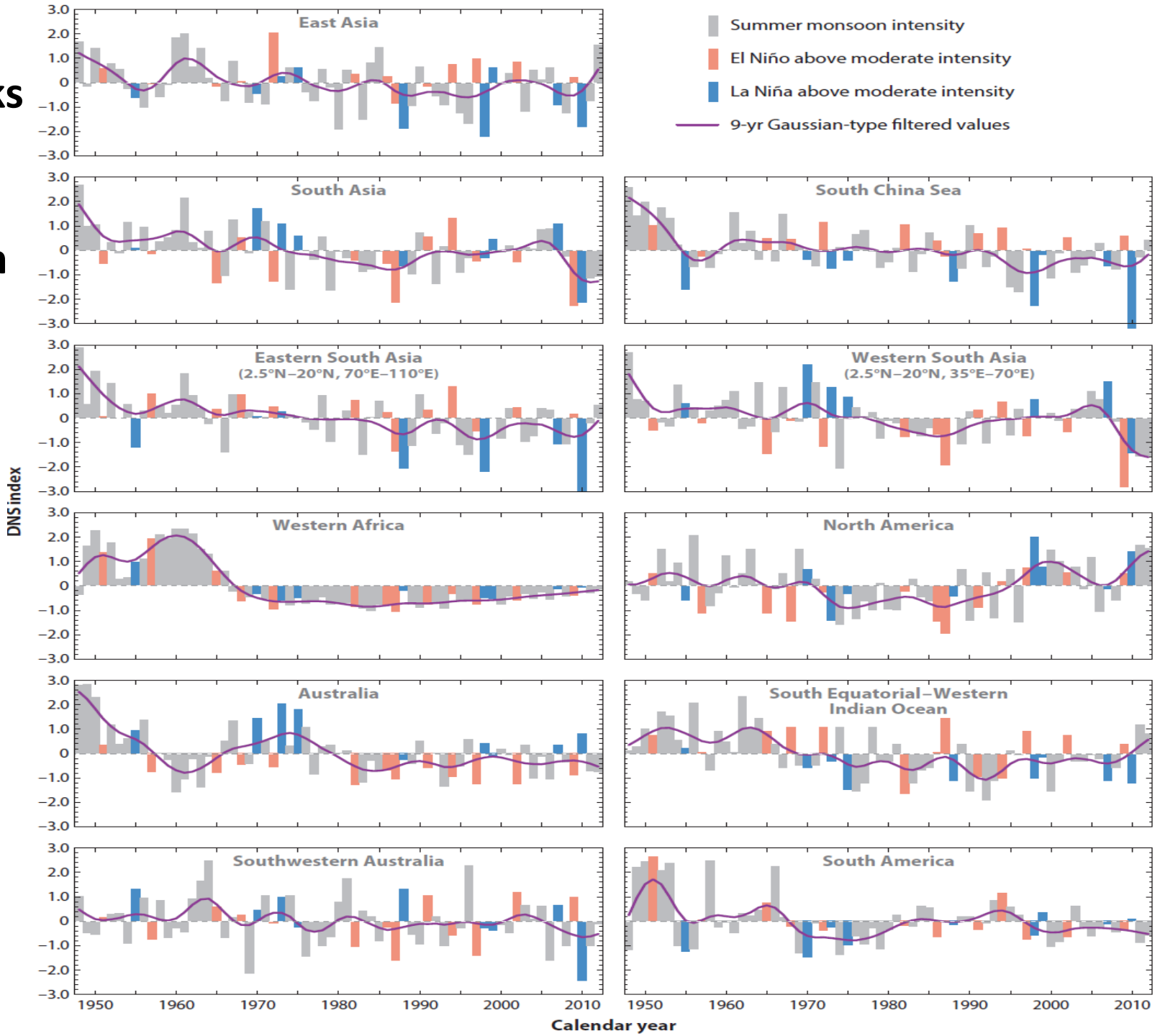

Especially considering peak phase of ENSO vs monsoons

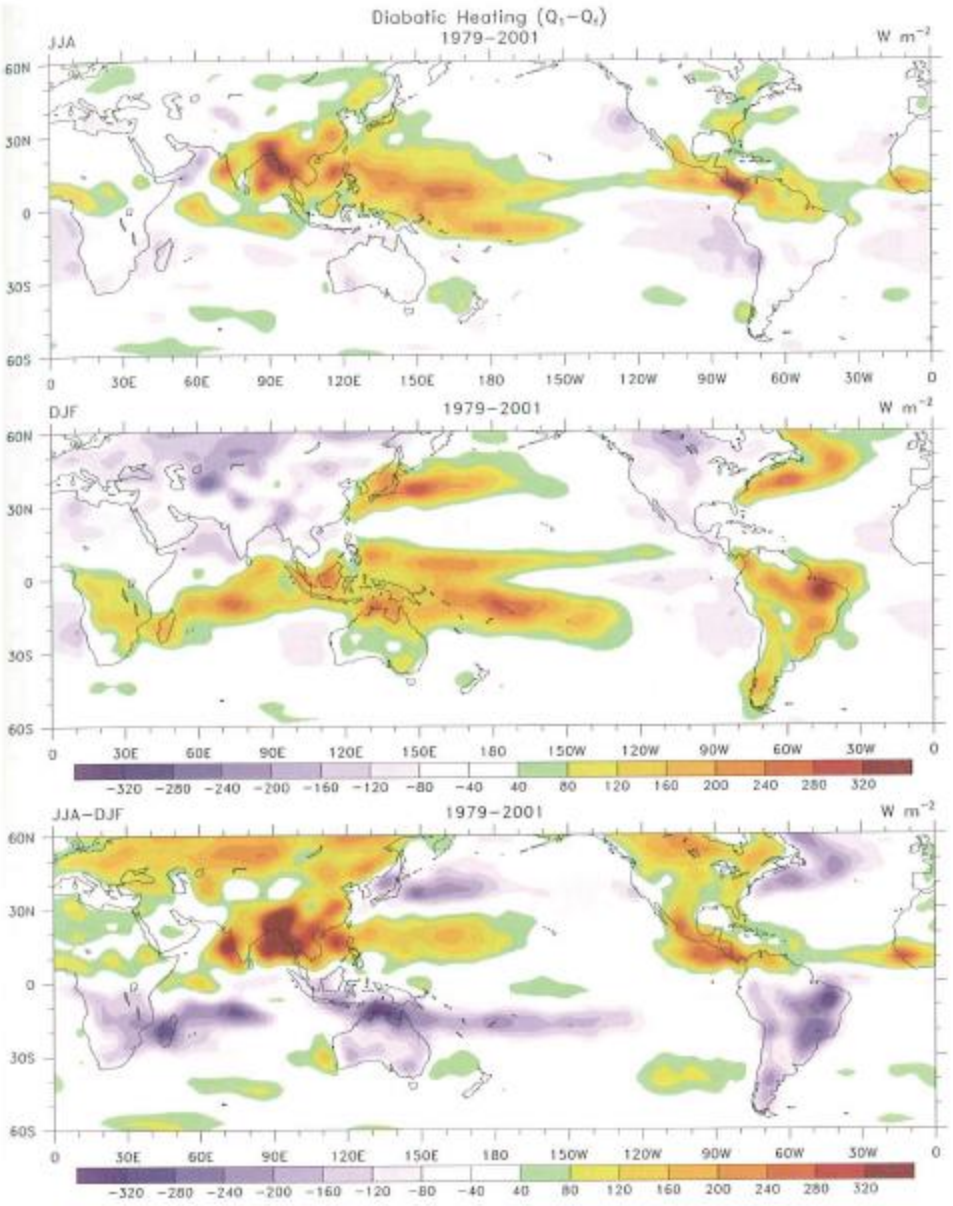

The vertically integrated diabatic heating in Wm^{-2}. The monsoonal regions of the globe are clearly identifiable, including their seasonal migration. From Trenberth (2006).

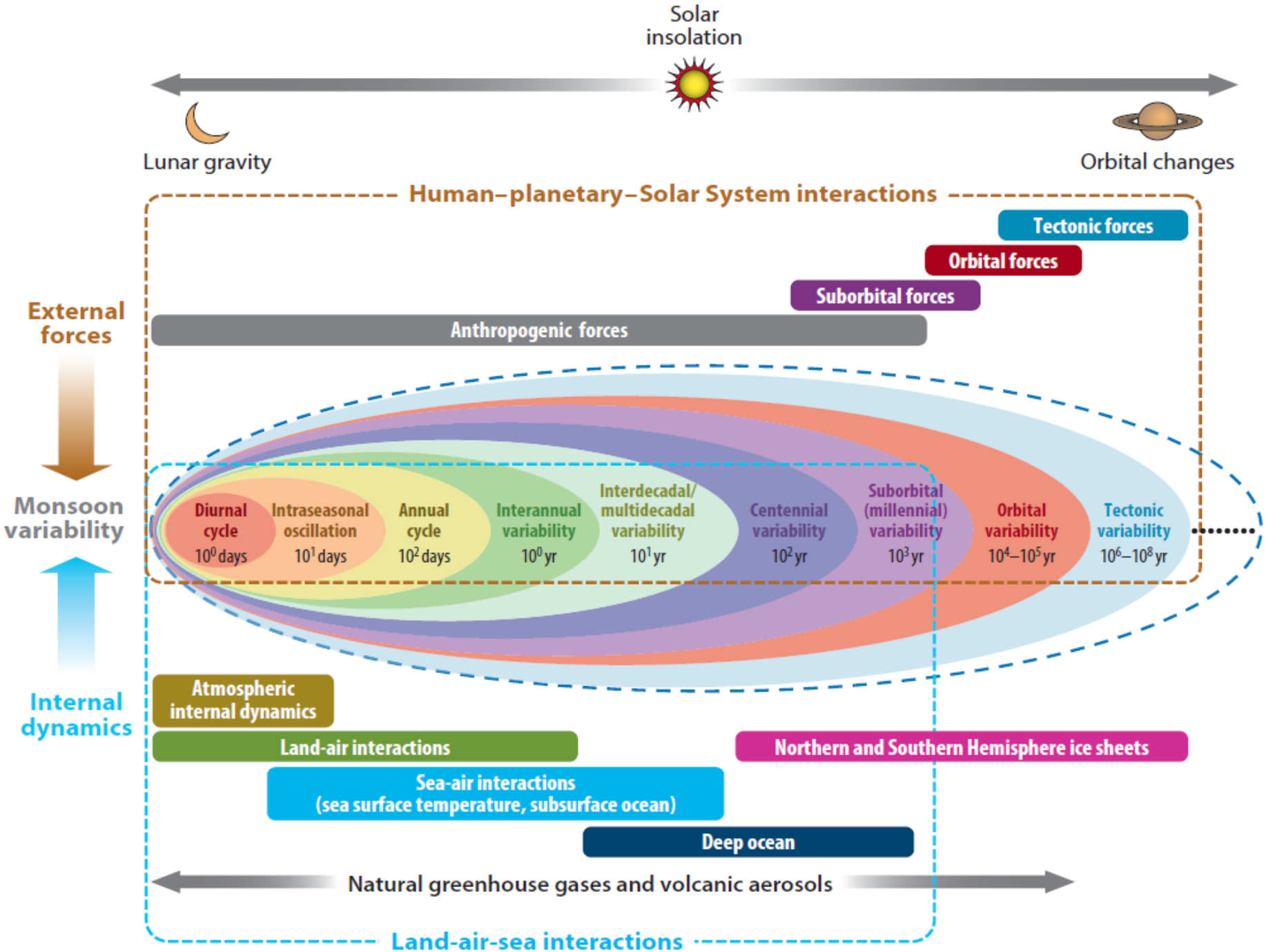
Solar insolation
Lunar gravity
Orbital changes
Human–planetary–Solar System interactions
Tectonic forces
Orbital forces
Suborbital forces
Anthropogenic forces
External forces
Monsoon variability
Internal dynamics
Diurnal cycle 10^0 days
Intraseasonal oscillation 10^1 days
Annual cycle 10^2 days
Interannual variability 10^0 yr
Interdecadal/ multidecadal variability 10^1 yr
Centennial variability 10^2 yr
Suborbital (millennial) variability 10^3 yr
Orbital variability 10^4–10^5 yr
Tectonic variability 10^6–10^8 yr
Atmospheric internal dynamics
Land-air interactions
Northern and Southern Hemisphere ice sheets
Sea-air interactions (sea surface temperature, subsurface ocean)
Deep ocean
Natural greenhouse gases and volcanic aerosols
Land-air-sea interactions